5
Understanding and Preventing Structural Changes During Drying of Gels

Thomas Metzger, Angélique Léonard, Wahbi Jomaa, and Hajime Tamon

5.1
Introduction

Gels are fragile materials with high liquid content so that it is quite a challenge to dry them without significant loss of product quality. The first question to be answered is why dry gels are so desirable that they are worth this effort. Therefore, the chapter starts with a summary of the advantages of the sol–gel process and the resulting extraordinary physical properties and possible technical applications of dry gels. Most of their quality features are a direct result of the gel structure, with the main features being high porosity and small pore and particle dimensions. In the next section, experimental methods are presented, which can be used to characterize this structure – before, after and even during drying – in order to assess the changes, and often damage, caused by this production step. As will be seen, standard characterization techniques for porous media also face problems due to the fragility of the gels. Then, different drying methods are presented in the light of how high is their risk to the gel structure. Theoretical considerations help one to understand why convective drying is bound to damage the gel by capillary forces, causing shrinkage and/or cracks, but also why even freeze-drying and supercritical drying present a considerable risk to the gel structure. In the following section, recent efforts are presented that aim at substituting the most successful process of supercritical drying by the cheaper and safer alternatives of, among others, convective and freeze-drying. Different strategies are chosen to prevent structural damage, and often a direct comparison is given between dry gels obtained by different methods; a new possibility to create product quality by freeze-drying is also shown. The last section is dedicated to recent theoretical approaches to convective drying with the goal to define the drying conditions and gel structures that are favorable for preservation during drying. The overall goal of the chapter is to provide a sound background and a comprehensive overview over the past two decades of research in the field of gel drying, with a focus on structural damage. Recent developments in sol–gel chemistry in terms of materials and synthesis conditions are, however, beyond the scope of the chapter.

Modern Drying Technology Volume 3: Product Quality and Formulation, First Edition.
Edited by Evangelos Tsotsas and Arun S. Mujumdar.

5.2
Gels and Their Applications – Quality Aspects

By gelation, technical porous media can be produced in the wet state. Several liquid precursors are mixed and – by reactions at the molecular level – particle nucleation, particle growth, and particle aggregation occur, finally leading to a sample-spanning solid network. This wet route has many advantages over other production methods such as the sintering of (ultra-)fine powders: different components can easily be mixed, ensuring a homogeneous product; due to the high mobility of the disperse solid in the liquid, self-assembly techniques can be used to create special structures; structure formation can be controlled by process parameters, either favoring growth or aggregation of the primary particles; porosity is mainly determined by the concentration of precursors in the mother liquor and can, therefore, be tuned over a wide range, including very high values; furthermore, no high temperatures are required to form the solid network; and finally, gels can be produced in a wide range of geometrical shapes by molding techniques, fiber drawing, dip and spin coating, or even by impregnation of the inner surface of a material that contains large pores.

The remaining challenge – before use in technical applications – is to remove the liquid without altering the solid structure by interfacial forces. Before addressing this drying step in great detail, important aspects of producing wet gels, as well as the extraordinary physical properties of successfully dried gels and their high-tech applications are presented in this section.

5.2.1
Preparation of Wet Gels

From the plethora of inorganic and organic gels, two widely spread representatives, namely silica gels and resorcinol-formaldehyde (RF) gels, will be briefly introduced to discuss the major mechanisms of gel formation and to illustrate possibilities for engineering gel structure. Whereas highly porous dry silica gels were successfully prepared back in the 1930s (Kistler, 1931), dry organic RF gels are a relatively recent material (Pekala, 1989).

5.2.1.1 Silica Gels

Silica is an attractive material for inorganic gel applications because it is non-toxic, non-flammable and easy to dispose of. Dry silica gels have a translucent, bluish appearance. For gel synthesis at lab-scale, a tetraalkoxysilane $Si(OR)_4$, commonly tetramethoxysilane (TMOS) or tetraethoxysilane (TEOS), dissolved in the respective alcohol ROH, acts as the silica source. When water is added, two chemical reactions occur: the first, hydrolysis,

$$\equiv \text{Si-OR} + \text{H}_2\text{O} \leftrightarrow \equiv \text{Si-OH} + \text{ROH} \tag{5.1}$$

prepares the individual molecules for the second, condensation,

$$\equiv \text{Si-OH} + \text{HO-Si} \equiv \leftrightarrow \equiv \text{Si-O-Si} \equiv + \text{H}_2\text{O} \tag{5.2a}$$

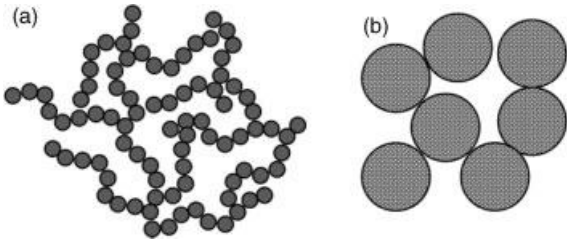

Fig. 5.1 Two major types of gel networks: (a) polymer-like and (b) colloidal.

$$\equiv \text{Si-OR} + \text{HO-Si} \equiv \leftrightarrow \equiv \text{Si-O-Si} \equiv + \text{ROH} \tag{5.2b}$$

which interlinks individual molecules, resulting in particle growth and aggregation (Hüsing and Schubert, 2006). The relative rates of these two reactions determine the structure of the forming solid network and can be adjusted by the pH of the solution. To put it simply, under acidic conditions, condensation is the limiting step and occurs favorably at terminal silicon atoms resulting in a polymer-like network of small particles (typically < 5 nm) that are connected by wide necks, as in Fig. 5.1a. In contrast, under basic conditions, hydrolyzed molecules immediately condense with no spatial preference so that rather dense particles are formed; these particles can grow (typically > 10 nm), before aggregation occurs with relatively narrow necks, as in Fig. 5.1b (Boonamnuayvitaya *et al.*, 2006). In practice, a two-step process with a change of pH is often used, offering more possibilities to engineer the gel structure. Not only the size distribution of particles and pores, but also the porosity can be adjusted, simply by changing the silica concentration in the starter solution.

Controlled aging of the wet gel is used to strengthen the network: hydrolysis and condensation reactions are to some extent reversible, and solid can be dissolved from thermodynamically unfavorable regions to condense at more favorable places. During this Ostwald ripening, small pores are filled and solid bridges grow, thereby reducing curvature – and area – of the solid/liquid interface (Hüsing and Schubert, 2006).

When the gel is aging, new bonds can also be formed between neighboring branches of the network, which are brought into contact by thermal fluctuations. As a consequence, the gel not only stiffens, but also shrinks linearly by a few percent and expels some of the pore liquid; this is called syneresis (Scherer, 1999). The described synthesis and post-processing of silica gels is performed at (or slightly above) room temperature.

For commercial silica gels, water glass Na_2SiO_3 is used as a cheap silica source; then, before the gelation step, sodium is ion-exchanged from the aqueous sodium silicate solution to get a silicic acid (Schwertfeger *et al.*, 1998).

5.2.1.2 **Resorcinol-Formaldehyde (RF) Gels**

RF gels are probably the most intensively studied organic gels with high porosity applications. Dry RF gels are dark red and transparent (Hüsing and Schubert, 2006); by pyrolysis in an inert atmosphere, they can be converted into electrically conducting

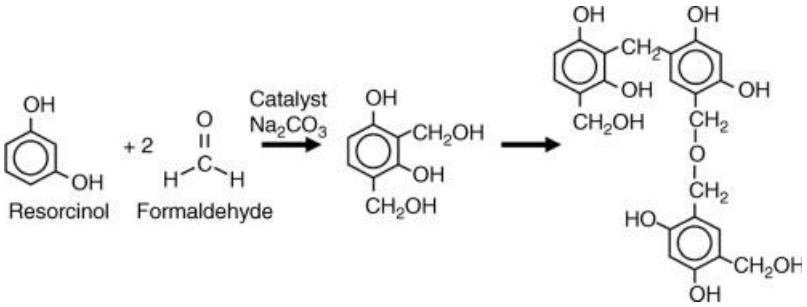

Fig. 5.2 Synthesis of RF gel: addition and condensation reaction (simplified from Lin and Ritter (1997)).

carbon gels (black and opaque) making them suitable for applications complementary to those of silica gels.

The two steps of gel synthesis are sketched in Fig. 5.2: in an aqueous (or organic) solution of resorcinol and formaldehyde (molar ratio 1: 2), an addition reaction is catalyzed by sodium carbonate to form hydroxymethyl derivatives; subsequently, these are interlinked by methylene ($–CH_2–$) or methylene ether ($–CH_2OCH_2–$) bridges in endothermic condensation reactions (Al-Muhtaseb and Ritter, 2003). Historically, sodium carbonate is referred to as a catalyst, although its only role is to tune the pH value (Job *et al.*, 2004).

Gel structure can be tuned by the molar ratio between resorcinol and catalyst (R/C), which controls the relative rate of the necessary addition reaction; the reasoning is analogous to the silica gel case: low R/C favors the addition reaction so that polymer-like gels are formed (Fig. 5.1a); for high R/C, emerging hydroxymethyl derivatives are immediately consumed in the condensation reaction, leading to colloidal gel networks (Fig. 5.1b). Again, the amount of solvent determines the porosity of the solid network.

Common post-processing of the wet gel includes curing at elevated temperature ($\sim$80 °C) and aging in a dilute acid, both for several days. This increases the degree of crosslinking and hence strengthens the gel network, fortunately, without the negative effect of shrinkage.

Besides the silica and RF model systems, there is a large variety of further technical gels. Other material classes are metal oxide gels, such as alumina gels, which can be pure or serve as a carrier for metal compounds (catalytic sites); and inorganic/organic hybrid gels, which can combine the positive properties of both species. Doping or modification of gels is mostly done in the wet state, but also by impregnation of the dry gel (Hüsing and Schubert, 2006).

5.2.2
Properties of Dry Gels

First, a list of outstanding physical properties of highly porous dry gels will be given, all of which are determined by solid structure. In numerous research projects all over

the world, a large amount of knowledge has been accumulated on how the structure can be engineered by setting the process parameters for gelation and subsequent aging. The challenge is, therefore, to preserve the structure during liquid removal. Historically, the only successful technique was supercritical drying (see Section 5.4.3) and the resulting dry gels were named aerogels. Note that the term *aerogel* is often used for highly porous gels, no matter the chosen drying route; in this text, however, we will use it for gels dried under *supercritical conditions*. Alternative routes are reflected in the names for the dry gels: *cryogels* are the result of freeze-drying, *xerogels* are prepared by convective drying or, in a wider sense, evaporative drying.

The following properties (Hrubesh, 1998; Hüsing and Schubert, 2006) only apply to gels with low solid fraction, that is, to porous media that cannot easily be created by other production routes:

- **Extremely high porosity/extremely low density**: Dry gels can have the highest porosity and the lowest density of all solid materials but the actual values can vary over a wide range, depending on the choice of the gel system and its synthesis conditions. For silica aerogels, the most extreme values have been reached with bulk densities as low as $0.004\,g\,cm^{-3}$ and porosities higher than 99% (Tillotson and Hrubesh, 1992).
- **High specific surface area**: Gels are built from primary particles that can be approximated by mono-sized spheres. The specific surface area of such structures scales with the inverse of particle size, which is in the nanometer range (typically 5 nm), so that values around $600\,m^2\,g^{-1}$ are typical for most aerogels, organic and inorganic.
- **Extremely low thermal conductivity**: In porous media, heat transfer has contributions from solid and gas conduction and from radiation. Gels with low solid volume fraction show little solid heat conduction. Additionally, according to Knudsen, heat transfer by gas molecules in voids is significantly reduced as compared to the unconfined gas if the pore size is less than (or about) the mean free path ($\approx$70 nm for ambient air); this insulation effect is enhanced in vacuum. Radiation also depends on the pore size if the pore walls are opaque; then, for small pore size, many absorption–emission steps are needed for macro-scale heat transfer, just as in a super-insulator. At room temperatures, the thermal conductivity of silica aerogels is typically below $0.02\,W\,m^{-1}\,K^{-1}$ (air: $0.026\,W\,m^{-1}\,K^{-1}$); for RF aerogels, $0.012\,W\,m^{-1}\,K^{-1}$ have been reported (Lu *et al.*, 1992), and for evacuated silica aerogels, values as low as $0.01\,W\,m^{-1}\,K^{-1}$ are possible (Scheuerpflug *et al.*, 1985). At high temperatures, that is, in the infrared range, silica does not absorb well, but special opacifiers, such as carbon black or titanium dioxide, can be incorporated in the solid network during gelation (Lu *et al.*, 1992).
- **Optical transparency**: If the solid phase itself is transparent, as for silica gels, light can be transmitted through the dry gel with little interaction since the structural units of gels are much smaller than the optical wavelengths. Only structural inhomogeneities at the nanometer scale lead to Rayleigh scattering and the typical blue appearance (against a dark background), and surface inhomogeneities at the micrometer scale blur the view through aerogel plates (Wang *et al.*, 1992), making

the gel a translucent, rather than transparent material. Typically, 84% of light is transmitted, which is only a small reduction from the 89% transmission for bulk silica glass (Sakka, 2005).

- **Low refractive index**: Compared to bulk solid materials such as silica glass, which has a refractive index of around 1.5, typical silica aerogels exhibit values very close to unity (Bellunato *et al.*, 2007), meaning that the speed of light is only slightly reduced. The refractive index can be tuned in the range from 1.007 to 1.25 by adjusting the density of the aerogel (Wang *et al.*, 1992; Kharzheev, 2008).
- **Low dielectric constant**: In aerogels, the dielectric constant is well below 2, and the value depends on the gel density so that it can be tuned by synthesis conditions (Geis *et al.*, 2000). Other solid materials have a dielectric constant (usually much) greater than 2, for example, quartz glass has a value of 4.
- **Low sound speed**: The velocity of sound in silica aerogels is very low for a solid material; typical values are around 100 m s^{-1}, as compared to 5000 m s^{-1} in quartz glass (Daughton *et al.*, 2003).
- **Mechanical properties**: Even for very porous materials (99%), the stress–strain curve shows perfect elastic behavior, and the conchoidal fracture morphology indicates that the material is brittle, like a conventional glass; however, elastic and rupture moduli can be 10 000 times lower than those of silica glass (Woignier *et al.*, 2005). Under compression, at increasing strain, the network exhibits yield, densification and plastic hardening (Woignier *et al.*, 2005). Typical silica aerogels have a compressive strength of 0.15–0.3 N mm^{-2} with an elastic compression of 2–4%; their tensile strength is about 0.02 N mm^{-2} (Hüsing and Schubert, 2006). Of course, these values depend on the connectivity in the solid network which is determined by the preparation conditions.
- **Hydrophobicity**: Silica aerogels are hydrophilic because of the silanol groups ($\equiv$Si-OH); in a humid atmosphere, adsorption and capillary condensation occur and capillary forces can destroy the fragile structure. To achieve long-term stability, hydrophobation is necessary, for example, by trimethyl silylation of the wet gel (Shewale *et al.*, 2008).

5.2.3 Applications of Dry Gels

It is clear that highly porous gels have a great number of interesting potential applications (Hrubesh, 1998; Sakka, 2005; Hüsing and Schubert, 2006) because of their previously described extraordinary properties. Some specific applications are already reality; many others are still awaiting improvements in the economy and safety of production for their commercial breakthrough. In the following, the most important applications of dry gels are listed:

- **Thermal insulation**: Large commercial potential lies in applications coupling thermal insulation with transparency, especially in the building sector, where monolithic silica aerogels might be used as transparent windows (Jensen *et al.*, 2004); layers of granular aerogels where diffuse lighting is acceptable or

desired (Schmidt and Schwertfeger, 1998); and aerogel coatings for insulation of solar heat collectors, where both transparency to sunlight and the confinement of generated heat are essential. Of course, there are also numerous thermal insulation applications where transparency plays no role, for example, in high or low temperature storage. In space technology, opacified aerogels serve as lightweight thermal insulation, for example, in the exploration of Mars where electronics have to be protected from the 100 K temperature difference between night and day (Jones, 2006).

- **Sound insulation**: Sound absorption in buildings or, more specialized, in anechoic chambers, opens another promising field of applications. Unlike for other materials, good absorption is also observed for the low frequency range. While suitable bulk aerogels are not yet available, respective composite materials containing aerogel particles can already be produced (Schmidt and Schwertfeger, 1998).
- **Electrodes for example, for supercapacitors or water treatment**: Monolithic carbon aerogels are very suitable electrode materials because of their low electric resistance and high specific surface area. One possible application is in supercapacitors where the voids of the gel are filled with an electrolyte. If voltage is applied, energy is stored by charge separation in the electrochemical double layer. High energy density and high power density make the device suitable for bridging short power failures. In other electrode applications, harmful contaminants are removed from industrial wastewater, or seawater is desalinated by (easily reversible) capacitive deionization during the passage by and through a stack of alternately polarized electrodes (Farmer *et al.*, 1996, 1997).
- **Cherenkov detectors in high energy physics**: The velocity and, hence, energy of a charged atomic particle is measured by Cherenkov detectors. They contain a medium with a speed of light lower than the selected range of particle velocities. When traveling through such a medium, the particle produces an electromagnetic shockwave; from the cone angle, the particle velocity is obtained. Here, aerogels with tuned density are able to cover a velocity range for which the previously used compressed gases or liquids were not suitable; additionally, they are much safer to handle. These detectors are large ($>1\,m^3$), and significant amounts of aerogel have already been produced for this application (Fricke, 1986).
- **Optical coatings**: The losses of optical devices can be reduced by coating them with an aerogel of (matched) low refractive index (Hrubesh and Poco, 1995; Hrubesh, 1998); in this way, more sunlight can reach the active surface of a solar cell and, in fiber optics, light collection at the fiber entrance and signal propagation efficiency can be improved.
- **Catalysis and chromatography**: These are obvious applications for aerogels with their tunable microstructure exhibiting high internal surface area and large pore volume. Concerning catalysis (Hüsing and Schubert, 2006), the sol–gel process allows good dispersion of the active component and aerogels can be prepared from most relevant oxides. However, some problems arise from the low permeability and the poor thermal conductivity; here, the deposition of aerogels on macroscopic structures offers a solution. In high-performance liquid chromatography, silica monoliths with bimodal pore size distributions

are used to combine good permeation and high binding capacity (Lubda *et al.*, 2005; Nunez *et al.*, 2008).

- **Space science**: During the Stardust mission (1999–2006), an aerogel array was used to capture cometary and interstellar particles. The particles stayed largely intact when they were smoothly slowed down by the small filaments of the gel network and could be returned to earth for analysis (Jones, 2006).

For all these applications, the pore structure and high porosity of the aerogel are very important, even if the geometrical shape may vary from large monoliths to particulate material, and to films. After gel synthesis, it is therefore crucial to preserve the solid network during the drying step.

5.3
Structural Characterization of Gels – Quality Assessment

Before addressing the drying step itself, a brief overview will be given of the techniques by which the structure of gels can be characterized, and some non-standard techniques will be discussed in greater detail. This will allow assessment of the quality of gels that have been dried by different routes. And, in some cases, it will allow direct quantification of the quality loss during drying.

5.3.1
Characterization of Wet Gels

The structural features of a gel are typically in the range of a few nanometers; and direct 3D visualization of wet gel structure is not possible: X-ray microtomography (μ-CT) has a spatial resolution of about (or just below) one micrometer; electron microscopy (in transmission mode, TEM, or in scanning mode, SEM, for the surface) has a substantially higher resolution, but works only on dry gels. Therefore, indirect methods, such as scattering of X-rays, are used to characterize gel structure and also to investigate the sol–gel transition.

5.3.1.1 Small Angle X-Ray Scattering (SAXS)

In the following, small angle X-ray scattering (SAXS) will be briefly introduced (Roe, 2000; Brinker and Scherer, 1990). As depicted in Fig. 5.3a, the X-ray beam hits the sample and the scattered signal is detected at a range of small angles. Structural units that are very large compared to the X-ray wave length (0.154 nm for $K\alpha_1$ emission from Cu) do not significantly scatter the X-rays and, therefore, cannot be detected; with decreasing size of the structural features, the corresponding scattering angles increase and structural information can be extracted from the spectrum, which is commonly plotted as signal intensity over wave vector. The interpretation of such spectra is a research field of its own (e.g., Sinko *et al.*, 2008). The most common characteristics extracted from SAXS spectra are particle size and fractal dimension, but other properties such as specific surface

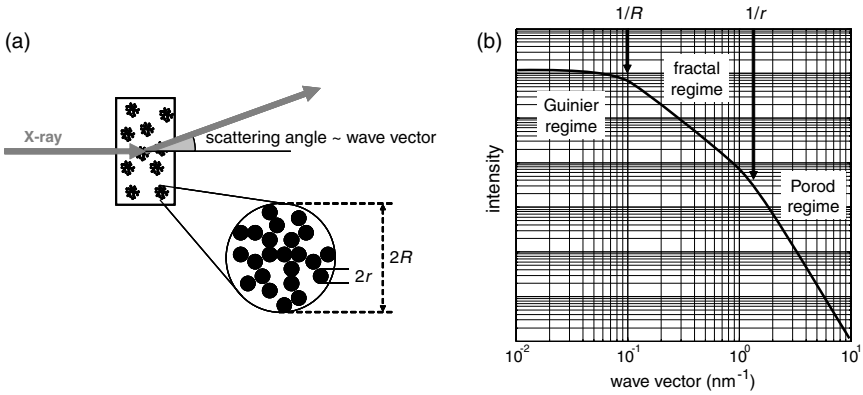

Fig. 5.3 Small-angle X-ray scattering (SAXS): (a) measurement principle and (b) typical spectrum for a dilute suspension of fractal aggregates built from dense primary particles.

area may also be accessed (Berthon *et al.*, 2001). Here, only some elements of interpretation will be discussed for an illustrative example, the spectrum of a suspension of aggregates shown in Fig. 5.3b. For very small angles, in the Guinier regime, the signal intensity is highest and, from its decay with increasing wave vector, the aggregate size can be computed. For wave vectors corresponding to smaller sizes, the spectrum contains information about the inner structure of the aggregates. The absolute value of the negative slope in the log–log representation equals the fractal dimension, if it is less than 3; slopes between -3 and -4 indicate surface fractal structures. The Porod regime, with a slope of -4, indicates compact particles with a smooth surface. If these particles are monodisperse, regular oscillations in intensity are observed which are characteristic for particle size (Berthon *et al.*, 2001). The transition between different regimes marks critical length scales of the system. In this example, the radius of primary particles r indicates the transition from dense to fractal geometry; whereas the radius of the fractal aggregates R is determined by the transition to the Guinier regime. It should be stressed that SAXS spectra of real systems may deviate significantly from this example. For instance, in fractal gels, there is no marked upper size limit except of the system size so that the Guinier regime can neither be clearly identified, nor can it be used for a straightforward analysis as above. If larger structural features are investigated, light scattering provides a suitable technique due to the greater wavelengths; by a combination of light scattering with SAXS, it could be proven that gels are fractal over several length scales (Schaefer *et al.*, 1984).

In a traditional way, SAXS is used to investigate the correlation between synthesis parameters and the resulting gel structure, for example, the dependence of the fractal dimension of silica gels on TEOS concentration in the starter solution (Vollet *et al.*, 2008). Time-dependent SAXS has been applied to study sol–gel transition, in terms of particle growth and change in fractal properties in the forming structure (Tamon and Ishizaka, 1998). But the method also works on dry gels and, for

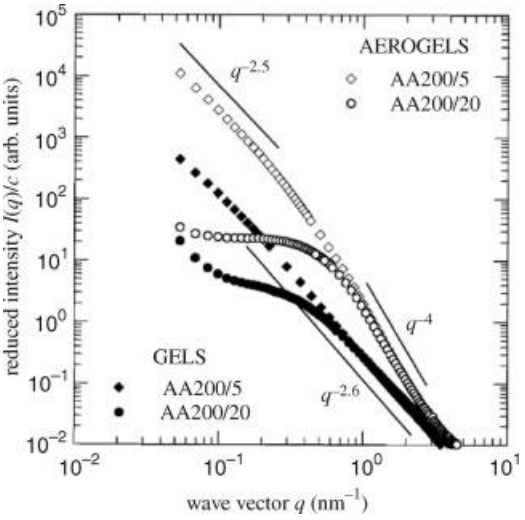

Fig. 5.4 SAXS spectra for RF wet gels and aerogels: both types have been prepared in acetone solution with acid catalyst (R/C = 200); the mass fraction of RF in the starter solution was 5% for "AA200/5" and 20% for "AA200/20" (taken from Berthon *et al.* (2001)).

example, has helped to characterize long-term restructuring of silica–alumina aerogels (Sinko *et al.*, 2008).

Berthon *et al.* (2001) performed SAXS measurements on gels in the wet state and after supercritical drying. They proved that for polymer-like RF gels formed in acetone and with *acid* catalysis, the structure is not fully preserved by drying with supercritical CO_2. The SAXS spectra for wet and dry gels, replicated in Fig. 5.4, show a significant change in slope from −2.6 (indicating fractal geometry) to −4 (indicating compact smooth particles) for large wave vectors. This suggests that fractal structures at small length scales have collapsed into dense particles (≈ 3 nm in size) during drying. For the high porosity (88%) sample "AA200/5", the dry gel consists of fractal aggregates of particles; for the "AA200/20" aerogel, no fractal features are visible. The authors attribute the evolution of gel structure rather to solvent exchange (CO_2 for acetone) than to drying itself. For *base*-catalyzed (R/C = 200) gelation in water or acetone, for which colloidal gels are expected, SAXS spectra suggest non-fractal structures that are preserved during drying.

5.3.1.2 **Thermoporometry**

Another suitable method to characterize the pore structure of wet gels is thermoporometry (Brun *et al.*, 1977). It uses the fact that the melting temperature of ice is reduced with decreasing crystal size due to the increasing curvature of the ice/water interface (Gibbs–Thomson effect). In the characterization experiment, the sample is either gradually frozen or slowly heated from the frozen state in a differential scanning calorimeter (DSC). The enthalpy flow released or required for the phase change at a given temperature is recorded. It is proportional to the pore volume that

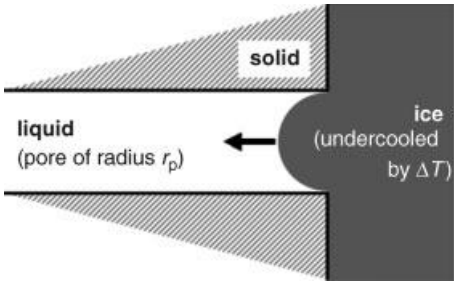

Fig. 5.5 Ice penetrating into a pore during freezing (ice considered as non-wetting).

freezes/melts at the corresponding undercooling ΔT. This undercooling can be converted into the pore radius for water as pore liquid by (Brun *et al.*, 1977)

$$r_p[\text{nm}] = 0.57 + \frac{64.7}{\Delta T[\text{K}]}, \text{ for } 0 < \Delta T < 40\ \text{K} \tag{5.3}$$

Hence, the pore volume distribution of the gel can be computed from the DSC thermogram. This method is only suitable for pore radii of 1–30 nm because liquid in smaller pores does not freeze and, for larger pores, the undercooling is too small for reliable measurement. Scherer (1993) interprets the freezing of a gel as the penetration of ice into progressively smaller pores as the undercooling ΔT increases (see Fig. 5.5) and, therefore, sees thermoporometry as an analogue of mercury porosimetry for saturated porous media. If the material is not rigid, but compliant, liquid may flow out of the pores instead of ice penetrating them, resulting in gel shrinkage (see Section 5.4.2) and a shift of the pore size distribution to smaller values.

Figure 5.6 shows the results of recent literature work, in which thermoporometry was applied to silica gels synthesized with ultrasound-assisted hydrolysis (Vollet *et al.*, 2008). For higher dilution of the TEOS starter solution, the gel

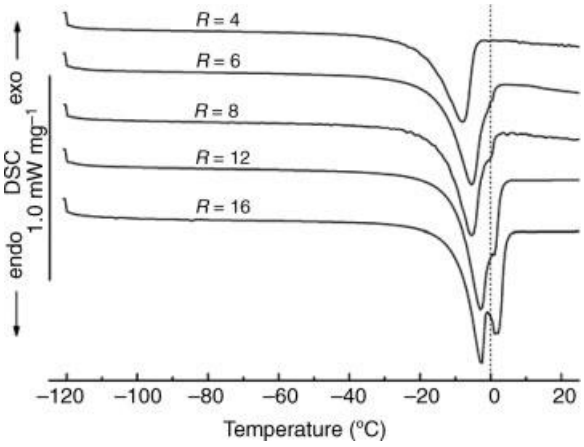

Fig. 5.6 DSC thermograms for silica gels with porosities from 78% (R = 4) to 88% (R = 16); *R* indicates the molar ratio of hydrolysis water to TEOS (taken from Vollet *et al.* (2008)).

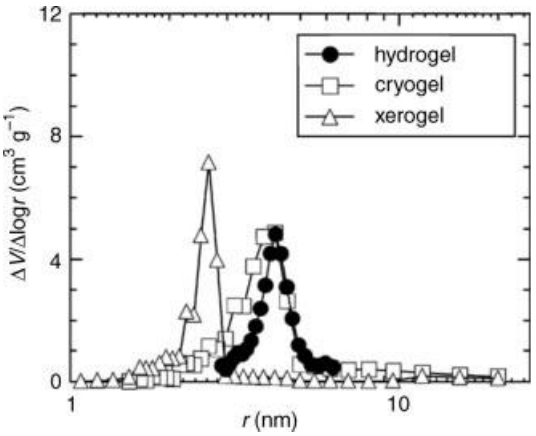

Fig. 5.7 Pore size distribution of wet RF gel (R/C = 200, R/W = 0.5 g cm^{-3}) by thermoporometry, and of corresponding dry gels by nitrogen adsorption (taken from Yamamoto *et al.* (2005)).

porosity was increased and the mean pore radius shifted, approximately from 10 to 25 nm. Besides the peak resulting from nanoscale pores (<0 °C), the thermograms for gels of high porosity show a second peak (>0 °C), which the authors attribute to macropores. Following Scherer's argumentation, this signal might also result from water that has flown to the gel surface during freezing.

Thermoporometry has also been used to assess structural changes during the drying step: Yamamoto *et al.* (2005) have prepared RF gels, exchanged the pore liquid for *tert*-butanol and subsequently dried the gels by convective or freeze-drying. The pore volume distribution of the wet gels was measured by thermoporometry, that of the dry gels by nitrogen adsorption. The results, depicted in Fig. 5.7, clearly indicate that nanoscale pores shrink during convective drying whereas the gel structure can be preserved by freeze-drying.

5.3.2
Characterization of Dry Gels

5.3.2.1 Nitrogen Adsorption

On dry gels, standard characterization techniques for porous media are used, several of which have been described in Volume 2 of this series: helium pycnometry for pore volume determination (Section 6.3.1.2) as well as nitrogen adsorption at 77 K for surface area (Section 6.3.2.2, BET method), for microporosity (Section 6.3.3.2, Dubinin–Radushkevich method), for pore size distribution (Section 6.3.3.3, BJH method), and for total pore volume (Section 6.3.3.4). When characterizing gels by nitrogen adsorption, other methods are also used for data interpretation, for example, the t-plot method for microporosity (Lippens and de Boer, 1965) and the Dollimore–Heal method (Dollimore and Heal, 1964) or Broekhoff–de Boer theory for mesoporosity (Lecloux, 1981).

An additional technique to measure pore size distributions, which will be briefly introduced later, is mercury porosimetry. It uses the successive intrusion of mercury (non-wetting) and – due to the high surface tension of mercury and small pore size –involves high compressive pressures. Therefore, special attention has to be given to deformation effects that occur when dry gels with low mechanical stiffness and strengths are characterized. However, shrinkage and/or cracks may not only happen during mercury porosimetry, but also during nitrogen adsorption (Scherer *et al.*, 1995a).

In *nitrogen adsorption*, as the relative pressure rises, pores of increasing size are gradually filled by condensing nitrogen; consequently, the interface tension between nitrogen and vapor (0.00885 N m^{-1}) exerts capillary forces on the aerogel and may lead to significant volumetric shrinkage. As the relative pressure approaches unity, the liquid/vapor interface becomes flat and the gel may expand to its full original volume, if no plastic deformation has occurred. Subsequent desorption is analogous to slow atmospheric drying; it is accompanied by shrinkage and a sudden expansion at low relative pressure since a small liquid volume in the capillary bridges can hold the sample under compression (Scherer *et al.*, 1995a). In Fig. 5.8, part of the adsorption–desorption cycle for a compliant gel is given: instead of showing a horizontal asymptote at saturation, the sorption curves reflect expansion and shrinkage of the (saturated) sample. For gels with different mechanical behavior, Reichenauer and Scherer (2000) have measured the sample dimensions during the sorption experiment. The compliant gel characterized in Fig. 5.8 underwent irreversible shrinkage; another, sintered gel was stiff enough to recover to its original size, both at full saturation and after complete desorption. For both gel types, pore volume information is obscured by shrinkage, resulting in underestimation of pore

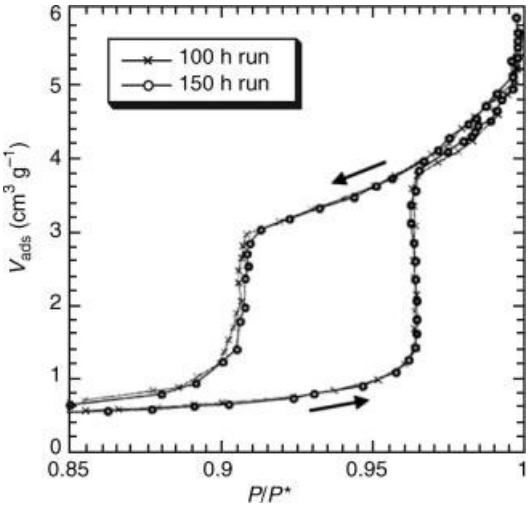

Fig. 5.8 Nitrogen adsorption-desorption cycle for a silica aerogel with 93% porosity (taken from Reichenauer and Scherer (2001a)).

size; an advanced characterization method has been proposed by the same authors, which uses dilatation and sorption data to obtain the bulk modulus and pore size distribution of the gel (Reichenauer and Scherer, 2001b).

Besides contraction of the sample, insufficient equilibration times may lead to wrong interpretation of nitrogen adsorption data (Reichenauer and Scherer, 2001a): because of incomplete filling of pores, the total pore volume is underestimated. In Fig. 5.8, two identically prepared aerogel samples have been characterized with different total duration of the cycle to prove sufficient equilibration.

5.3.2.2 **Mercury Porosimetry**

Whereas from nitrogen sorption data a size distribution can only be extracted for mesopores (with pore diameter $2\,\text{nm} < d_p < 50\,\text{nm}$), standard mercury porosimetry is used to obtain complete pore size distributions in the pore diameter range from 7.5 nm to 150 μm. During the characterization experiment, the sample is first surrounded and then progressively intruded by mercury, as the pressure is increased. Experimental results are commonly plotted as invaded pore volume versus applied pressure (see Fig. 5.9a). The *Washburn equation* describes at which (capillary) pressure a cylindrical pore of diameter d_p is invaded

$$P = \frac{4\sigma \cos\theta}{d_p} \tag{5.4}$$

where $\sigma = 0.48\,\text{N m}^{-1}$ is the surface tension and $\theta = 140°$ the contact angle of mercury, that is, 196 MPa corresponds to $d_p = 7.5$ nm. If the porous structure withstands these high pressures, as for some RF cryogels (Kocklenberg *et al.*, 1998), Eq. 5.4 allows conversion of pressures into pore sizes and easy computation of the pore size distribution (see Fig. 5.9b). More typically for gels, however, the structure collapses during characterization due to its weak compressive strength; or, depending on the conditions of the gel synthesis, drying and optional thermal treatment, some intrusion

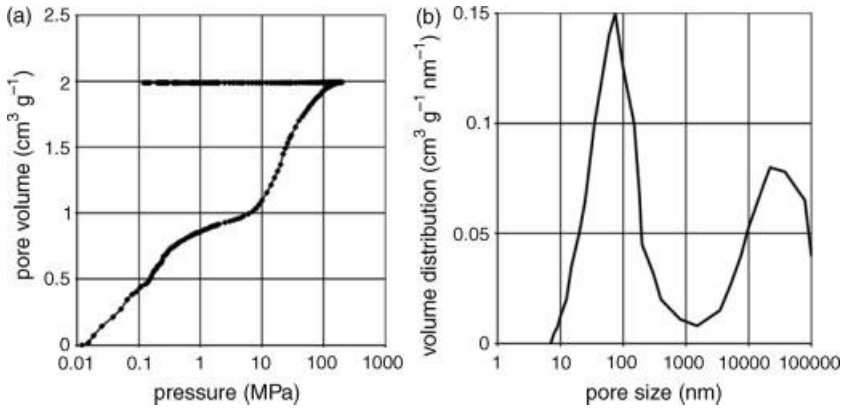

Fig. 5.9 (a) Mercury porosimetry data for dried copper hydroxide precipitate, pure intrusion case, (b) pore volume distribution by Eq. 5.4 (taken from Job *et al.* (2006a)).

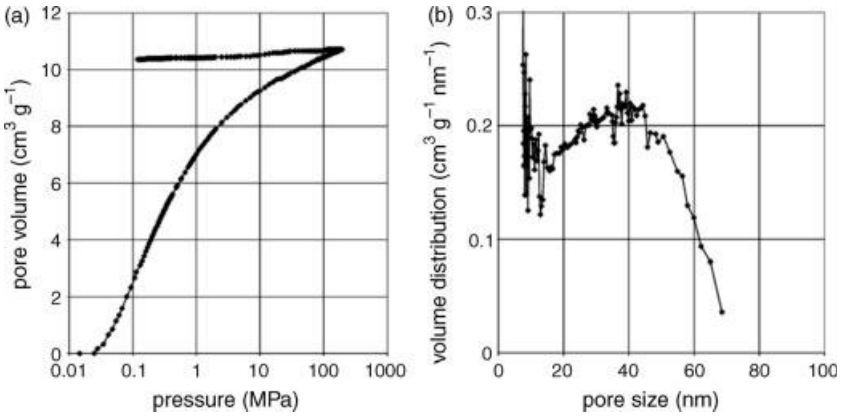

Fig. 5.10 (a) Mercury porosimetry data for monolithic silica aerogel, irreversible shrinkage case, (b) pore volume distribution by Eq. 5.5 (taken from Job *et al.* (2006a)).

may be observed after a first part of densification. Job *et al.* (2006a) discuss how these three different behaviors – pure intrusion, irreversible shrinkage, shrinkage followed by intrusion – can be distinguished and how mercury porosimetry data can be interpreted in each case (see also Pirard *et al.* (2005)).

Weighing of the sample before and after the porosimetry experiment can quantify the mercury which has intruded pores and is subsequently entrapped within the sample. In the case of pure intrusion, the full detected mercury volume remains within the sample, as revealed by the depressurization branch in Fig. 5.9a. If no mercury is found in the porous solid after porosimetry, the volume change of the sample may be measured (by mercury pycnometry as explained below) to confirm the assumed extent of irreversible shrinkage.

An example of irreversible shrinkage during mercury porosimetry is given in Fig. 5.10a. The shape of the curve reflects a progressive increase in mercury volume penetrating into the measurement cell, in contrast to the characteristic sudden pore volume jumps which occur during mercury intrusion at pressures corresponding to prevalent pore sizes. Such densification during mercury porosimetry has been reported for various dry gels, among them silica aerogels (Alié *et al.*, 2000; Scherer *et al.*, 1995b), RF xerogels (Job *et al.*, 2004, 2005; Léonard *et al.*, 2005a, 2008), aerogels and cryogels (Job *et al.*, 2005), and carbon xerogels (Job *et al.*, 2004). Evidently, the Washburn equation must not be used to determine pore size distribution in this case. Pirard *et al.* (1995) showed that the densification is due to a *hierarchical collapse* of pores: the largest pores collapse first at the lowest pressure values; then, as the mercury pressure increases, pores of decreasing size are successively and completely eliminated by crushing. Based on that mechanism, he proposed an appropriate relation to analyze mercury porosimetry data, which links pore size, down to which crushing occurs, to applied pressure

$$d_p = C \cdot P^{-0.25} \tag{5.5}$$

Here, C is a constant for material stiffness that needs to be determined experimentally. Figure 5.10b shows the pore size distribution obtained using this equation. It should be noted that densification curves may also be used to determine the bulk compression modulus of silica aerogels (Scherer *et al.*, 1995b).

Figure 5.11a shows mercury porosimetry data for a silica xerogel with mixed behavior: the material first shrinks (full circles) up to a critical pressure P_{cr} beyond which its small, uncollapsed pores are intruded (open circles). The critical pressure is identified by a sudden change of slope of the volume variation curve. If the sample is depressurized before reaching P_{cr} (crosses), then indeed no mercury uptake is detected in the sample. The pore volume distribution in Fig. 5.11b can be computed using either Eqs. 5.4 or 5.5 depending on the considered pressure domain. At $P = P_{cr}$, both equations are valid so that the mechanical constant C – necessary for the hierarchical collapse equation – can be obtained conveniently (Pirard *et al.*, 1998):

$$C = 4\sigma \cos\theta \cdot P_{cr}^{-0.75} \tag{5.6}$$

Such mixed behavior during mercury porosimetry has been observed for a range of dry gels, for example: silica xerogels and aerogels (Alié *et al.*, 2001), RF xerogels (Léonard *et al.*, 2008), and carbon xerogels, aerogels and cryogels (Job *et al.*, 2005).

For gels, the mechanisms involved during mercury porosimetry tests depend strongly on the microstructure, which is related to the synthesis (Léonard *et al.*, 2008) and drying conditions (Job *et al.*, 2005); therefore, one must carefully examine the measurement results to be sure of the mechanisms involved. If data corresponding to densification are analyzed using software based on the Washburn equation (usually provided with porosimeters) this yields an unphysical pore size distribution.

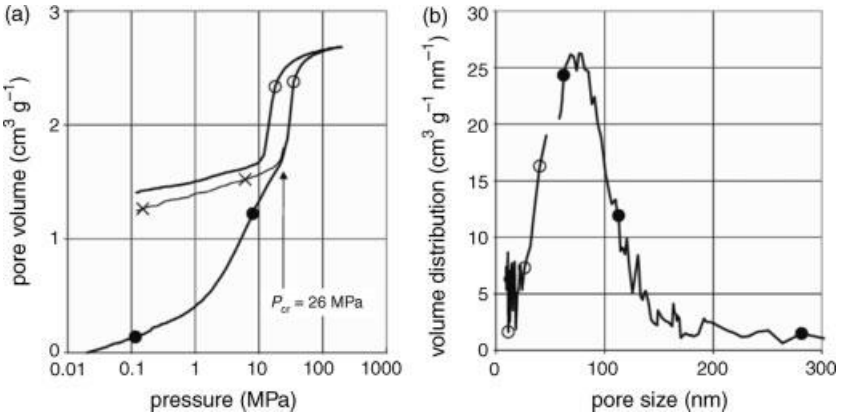

Fig. 5.11 (a) Mercury porosimetry data for silica xerogel, shrinkage followed by intrusion, (b) pore volume distribution by combining Eqs. 5.4 to 5.6 (taken from Job *et al.* (2006a)).

5.3.2.3 Other Methods

Another useful technique is *mercury pycnometry* which can be used to determine the geometrical volume of the dry gel (pores and solid), hence giving complementary data to helium pycnometry which measures only the pore volume. In this characterization method, a volume-calibrated chamber containing the sample is filled with mercury; the mercury volume (or weight) is measured to compute the sample volume. Unlike mercury porosimetry, no pressure is exerted so that mercury neither enters the pores nor crushes the sample.

Besides the determination of the porosity, pore size distribution and surface area, the (surface or mass) fractal dimension of dry gels may be of interest. To this purpose, small-angle X-ray scattering can be used; nitrogen sorption and mercury porosimetry also offer possibilities to extract this structural information (see, for example, Blacher *et al.* (2000)).

All previously described characterization methods yield only statistical or averaged information on gel structure. The natural wish to actually see the structure can be (partially) fulfilled by *scanning* or *transmission electron microscopy* (SEM or TEM). In SEM (Goldstein *et al.*, 2003), operating in high vacuum, a focused electron beam scans the sample surface and the local response (emitted secondary electrons) is recorded; therefore, spot size sets the resolution limit above 1 nm. To avoid charging of the sample during measurement, it needs to be made electrically conducting by sputter-coating with a thin gold layer, further decreasing the resolution. An alternative is offered by environmental SEM in which the sample is near or at atmospheric pressure allowing discharge through the gas phase. (In principle, ESEM also allows the investigation of wet samples, but to our knowledge has not yet been applied to wet gels.) In SEM, the surface is imaged in a three-dimensional appearance; however, the contrast in the image can be caused by a plenitude of effects so that careful interpretation is recommended. A clear advantage of SEM is that bulk samples can be characterized.

In contrast, TEM (Reimer and Kohl, 2008) is an optical method, in which electrons are interpreted as an electromagnetic wave of very short wavelength; as a result, higher resolutions (well below 1 nm) are possible and sputter-coating is not necessary. The sample is placed in high vacuum and imaged in transmission; consequently, it has to be very thin (typically 10–100 nm) to detect sufficient signal – and to actually see individual structural features. The obtained information is a two-dimensional projection of the sample, hence containing information from the whole sample depth.

Electron microscopy is mostly used qualitatively (some examples will be given in Section 5.5): for SEM, because of limited resolution and restriction to sample surface; and for TEM, because of the difficulty in separating information in the third dimension. Quantitative analysis of TEM data obtained from dry gels allows determination of the size distributions of primary particles, for example, in silica–alumina and silica aerogels, for which Sinko *et al.* (2008) have measured particle diameters in the range 3–14 nm.

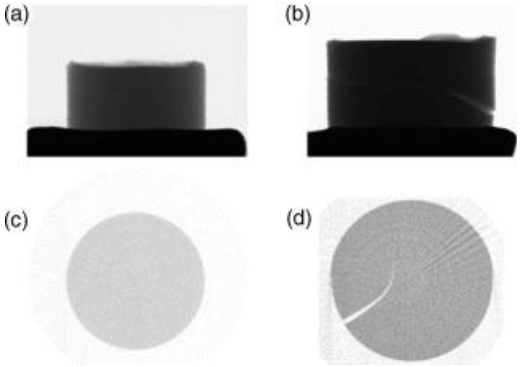

Fig. 5.12 X-ray transmission images (a,b) and reconstructed cross-sections (c,d) for RF gels showing shrinkage (a,c) and cracks (b,d).

5.3.3
Characterization of Gels During Drying

X-ray tomography is a non-destructive imaging technique giving access to the internal structure of the investigated object. The technique is based on the local variation of the X-ray attenuation coefficient of matter in the X-ray path. Two-dimensional cross-sectional images are reconstructed from transmission data collected by irradiating the object with an X-ray beam in many different directions (see Fig. 5.12), so that full volume data of the sample are accessible. (For a more detailed description of the measurement principle and subsequent image analysis, refer to Chapter 4 in Volume 2 of this series.) Nowadays, laboratory microtomographs allow the production of images with voxel size below 1 μm. Of course, this is not enough to see individual particles or pores in gels, but other important geometric and structural features are accessible: the dimensions, shape and volume of the gel sample, internal defects such as cracks, and local averages of gel density, porosity and moisture content. Therefore, the method offers a way of investigating shrinkage and the occurrence of cracks.

Since X-ray tomography keeps the sample intact, it is suitable not only for the characterization of the dried product, but also to follow the evolution of gel characteristics during the drying process. Up to now, this requires an interruption of the process to scan the sample being dried, but, in principle, the tomograph can be built around laboratory drying equipment. For such dynamic measurement, the time for a full scan of the sample is a crucial parameter; it depends on the sample size and the desired resolution and may vary from a few minutes, if 500^3 voxels are sufficient, to several hours, for 2000^3 voxels.

As most gels shrink during drying, it is essential to determine their surface area evolution to calculate the drying flux from mass loss measurements. With appropriate image analysis, very accurate shrinkage curves (as in Fig. 5.34) can be obtained from X-ray transmission images and reconstructed cross-sections (Fig. 5.12). The

same set of images can also be used to detect and quantify cracks appearing during drying. If crack-free materials are the quality goal, this experimental method can provide essential information for modeling and optimization of the drying process. Indeed, it is well-known (and will be explained in the following section) that too severe drying conditions may lead to sample cracking; and for a theoretical description, simulation of internal stresses must be combined with appropriate cracking criteria (see Section 5.6.1).

Finally, the images obtained from microtomography at different stages of drying can be processed to extract internal moisture distributions, which are very difficult to access by any other experimental technique. To this aim, calibration is necessary since only the wet gel density is available from tomography. Different possible drying behaviors are illustrated in Fig. 5.13 for RF gels, for which the attenuation of X-rays may be considered proportional to wet gel density (Escalona *et al.*, 2008). If the gel does not shrink, its density decreases as water is replaced by air; for gels exhibiting ideal shrinkage, that is, remaining fully saturated, the density increases as water "is replaced" by the dried RF resins whose intrinsic density is higher. Real behavior includes an initial period of ideal shrinkage followed by the emptying of pores with no further shrinkage. Therefore, the relationship between measured density and moisture content will generally not be unique for the whole drying process. Since all mentioned measurements are based on the same set of reconstructed images, they can be performed simultaneously.

In a more general context, X-ray microtomography can also help to determine the internal structure of the dried product. Unlike SEM, which requires sample preparation and yields only 2D information for a small part of the surface so that many repetitions are necessary for statistically relevant results, it is a non-destructive technique that gives full 3D information. For these reasons, X-ray microtomography can complement classical measurement techniques, if the dry material exhibits large pores which cannot be characterized by nitrogen adsorption (from 2 to 50 nm) or mercury porosimetry (from 7.5 nm to 150 μm).

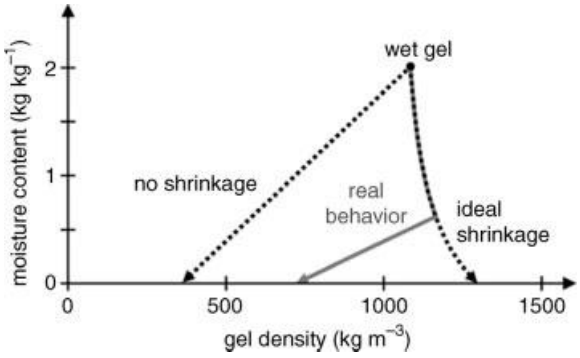

Fig. 5.13 Evolution of total gel density (as relevant for X-ray tomography) during drying for different material behavior (adapted from Escalona *et al.* (2008)).

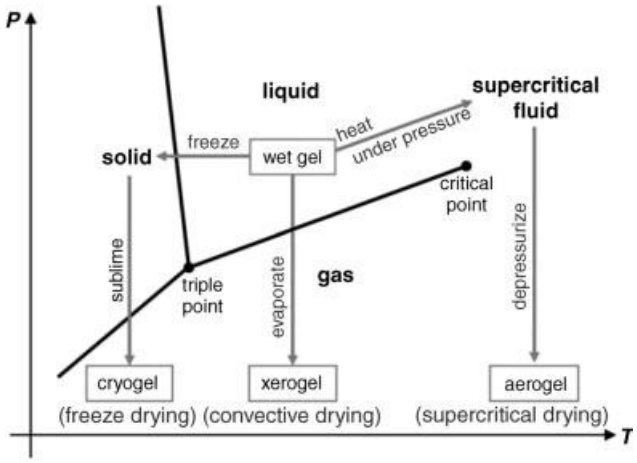

Fig. 5.14 Phase diagram to illustrate different drying methods for gels.

5.4
Drying Methods for Gels – Quality Loss

In this section, the major drying techniques for gels are presented. We stress again, that the term *xerogel*, despite its literal meaning ("dry gel"), will only be used for gels obtained by convective (or, more generally, evaporative) drying. Xerogels usually exhibit significant shrinkage, and it is difficult to avoid cracks, the reason lying in capillary effects, as will be discussed below. Therefore, other techniques such as freeze-drying and supercritical drying have been applied, where no liquid/gas phase boundary exists. As we will see, producing freeze-dried *cryogels* also bears a big risk for gel structure – if not in the drying step, then during freezing. The first successful technique to produce *aerogels* (in the sense that the full volume of pore liquid has been replaced by gas) was supercritical drying, this being the reason why here the term is only used for dry gels obtained by this route. Figure 5.14 summarizes the different drying techniques in the phase diagram for the pore-filling substance.

5.4.1
Convective Drying

5.4.1.1 Introduction

If a wet gel with low solid fraction and small pores is convectively dried without taking specific precautions, it will shrink significantly and irreversibly; a typical example is given in Fig. 5.15. Besides shrinkage, cracks may occur during drying, as shown for a rod of alumina gel in Fig. 5.16. The drying rate plays an important role in crack formation, so that different crack patterns are obtained or cracks can even be prevented by slow drying.

Fig. 5.15 Convective drying of a hydrogel (based on polyvinylpyrrolidone) (taken from Pakowski *et al.* (2006)).

In the following, we will sketch the theoretical framework for convective drying as developed by Scherer (1986, 1987a, b, c, 1988, 1989, 1990a, b, 1992a) and Brinker and Scherer (1990), which serves as a good basis to understand structural damage and to explore possibilities for preventing it.

5.4.1.2 **Shrinkage**

As liquid is removed from the gel surface by evaporation, the liquid/gas interface becomes curved. The resulting capillary pressure P_c is defined as the pressure difference between the gas and the liquid and is computed from the interface tension σ and the radius of curvature r_c (see Fig. 5.17a) as

$$P_c = P_g - P_w = \frac{2\,\sigma}{r_c} = \frac{2\,\sigma\cos\theta}{r_p} \tag{5.7}$$

The conversion into pore radius r_p and contact angle θ is only valid for a fully developed meniscus in cylindrical pores under the condition that the adsorbed liquid film can be neglected. This pressure can attain very high values, for example, approximately 30 MPa for water in perfectly wetted pores of radius 5 nm. Before analyzing the response of the gel to this pressure, the stress in the wet gel is defined; it

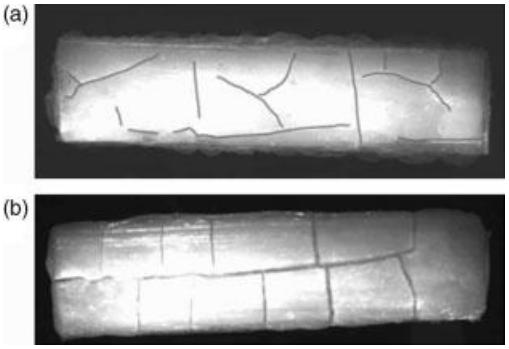

Fig. 5.16 Crack patterns on alumina gel for (a) slow and (b) fast convective drying (taken from Pourcel *et al.* (2007b)).

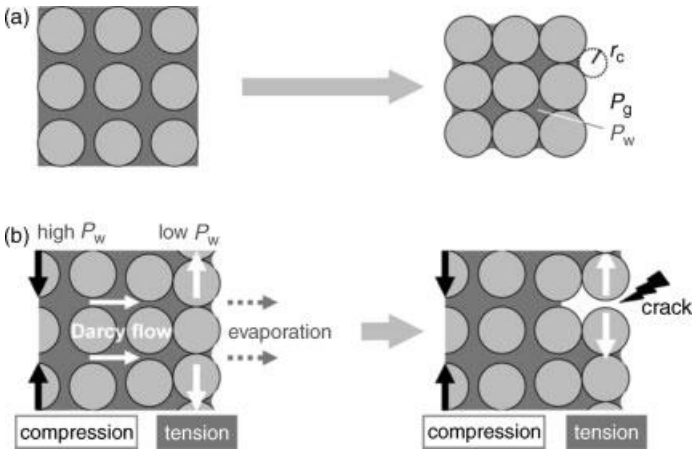

Fig. 5.17 Mechanisms during convective drying: (a) shrinkage of solid matrix as capillary pressure increases and (b) differential shrinkage when liquid flow is limited, leading to solid tension build-up and cracks when surface pores empty (only half of gel is shown).

has contributions from solid and liquid, as the respective forces F_s and F_w per total cross-sectional area A,

$$\sigma_x = \frac{F_{xs} + F_{xw}}{A} = \tilde{\sigma}_x - \psi P_w \tag{5.8}$$

Here, $\tilde{\sigma}_x$ is the solid network stress and ψ the porosity, and a negative liquid pressure is considered as compressive; equivalent equations hold for the y- and z-directions. For a small cube of gel or very low evaporation rates $\dot{m}_v$, liquid can easily flow to keep pressure gradients negligible, and uniform P_w can be assumed. Then, the liquid pressure is entirely balanced by the solid network stress $\tilde{\sigma}_x = \psi P_w$ (negative stress indicates compression), and the wet gel shrinks with no total stress, $\sigma_x = 0$. If the gel has a purely *elastic* solid network, then volumetric strain, that is, relative volume change, is given by

$$\varepsilon = \frac{\psi P_w}{K_0} \tag{5.9}$$

where K_0 is the bulk modulus of the gel. Gels of initial bulk density ϱ_0 can shrink reversibly until the density reaches a critical value ϱ_{cr}, roughly determined by

$$\Pi := \frac{\varrho_{cr} A_s m \sigma \cos\theta}{K_0} \approx 1 \tag{5.10}$$

where A_s is the specific surface area (given in $m^2 g^{-1}$ and roughly proportional to the inverse of the primary particle radius) and $2.5 < m < 4$ a material constant, both dependent on synthesis conditions (Smith *et al.*, 1995a). At the critical point (typically $\varrho_{cr} = 1.4\varrho_0$), the gel enters the *plastic* range: gel deformation is irreversible

and the shrinking gel becomes stiffer; the increase in bulk modulus can be approximated by

$$K_p = K_0(\varrho/\varrho_{cr})^m \tag{5.11}$$

Since shrinkage reduces the pore radius, the resulting compressive pressure also increases. With such a model, the density and pore size of the dry gel may be predicted (Smith *et al.*, 1995a): for $\Pi < 1$, the density increase during drying is less than 50% and reversible; otherwise, the dry gel density increases with increasing Π (irreversible shrinkage), for compliant gels roughly as $1.4\varrho_0\sqrt{\Pi}$. Shrinkage is hence more pronounced for higher surface tension, smaller contact angle, higher specific surface area (assumed as constant) and lower bulk modulus of the gel. In the above analysis, kinetics plays no role. It is therefore not surprising that shrinkage shows negligible dependence on drying rate (Smith *et al.*, 1995a).

5.4.1.3 **Differential Shrinkage and Stress**

Cracking, however, is strongly influenced by drying conditions: the fragments obtained when drying a wet gel cylinder become smaller as the oven temperature, and accordingly drying rate, is increased (Smith *et al.*, 1995a). To understand this, we must consider that liquid flow in the drying gel is limited by viscous effects. As illustrated in Fig. 5.17b, evaporation occurs at the gel surface so that shrinkage and decrease in liquid pressure start there. As a consequence, liquid is pumped from the core of the gel according to Darcy's law

$$\dot{m}_w = -\frac{K}{\mu_w/\varrho_w}\nabla P_w \tag{5.12}$$

where K is the permeability of the gel, μ_w the dynamic viscosity and ϱ_w the density of the pore liquid. Since gels have very low permeabilities – essentially, K is proportional to the square of the pore radius – even low drying rates can lead to high pressure gradients: for a typical permeability of $10^{-18}\,m^2$ and a drying rate of $1\,kg\,m^{-2}\,h^{-1}$, one obtains $3\,MPa\,cm^{-1}$. The liquid pressure profile is linked to the volumetric strain rate by

$$\dot{\varepsilon} = \frac{K}{\mu_w}\nabla^2 P_w \tag{5.13}$$

signifying that the solid network contracts locally when pore liquid flows out of that region.

In order to compute stress and strain in the drying gel, first, a constitutive equation for the wet gel must be derived. For an elastic solid network, the linear strain depends on the stress and liquid pressure as

$$\varepsilon_x = \frac{1}{E}\left[\sigma_x - \nu(\sigma_y + \sigma_z)\right] + \frac{P_w}{3K_p} \tag{5.14}$$

where E is the Young's modulus and ν the Poisson's ratio of the solid network. If this is applied to a plate (of thickness 2 L) that is dried from both sides, the local volumetric strain can be computed as

$$\varepsilon = ((1-C_0)\langle P_w\rangle + C_0 P_w)/K_p \tag{5.15}$$

where $\langle P_w\rangle$ is the average liquid pressure in the plate and C_0 is a function of Poisson's ratio and approximately 1/3 for highly compressive gels. There is a fundamental difference to Eq. 5.9, which describes free strain and is valid when liquid pressure and shrinkage are uniform in the gel. If pressure gradients develop, local shrinkage depends on both local and average liquid pressure, because regions of high and low pressure are connected and cannot contract freely at their natural rate.

Combining Eqs. 5.13 and 5.15 and using a boundary condition of constant evaporation flux at the plate surface $\dot{m}_w|_{z=L} = \dot{m}_v$, a time-dependent diffusion equation for the liquid pressure can be obtained and solved. For the stress in the plane of the plate, one finds

$$\sigma_x = \sigma_y \approx \langle P_w\rangle - P_w \tag{5.16}$$

This expresses the fact that stresses do not depend on the pressure *level* and only develop if there is a pressure *gradient*; further, it shows that during drying not only compression, but also tension will occur, the latter being a greater danger for the fragile gel structure. (Scherer nicely illustrates this behavior by a comparison with thermal stresses developing in a plate that is cooled from the surface.) Typical qualitative pressure and stress profiles in a drying elastic gel plate are plotted in Fig. 5.18.

One sees that the pressure profile becomes parabolic after a time that is characteristic for liquid flow; then, the profile shape stays unchanged, only the pressure level decreases. When the menisci at the gel surface are fully developed, the minimum pressure value is reached, given by Eq. 5.7, and the surface pores dry out, signifying the end of the first drying period. For the stress this means that a stationary profile is approached with a *maximum* tensile stress at the plate surface that can be given as

$$\sigma_x|_{z=L} \approx \frac{\mu_w \dot{m}_v L}{3\varrho_w K} \tag{5.17}$$

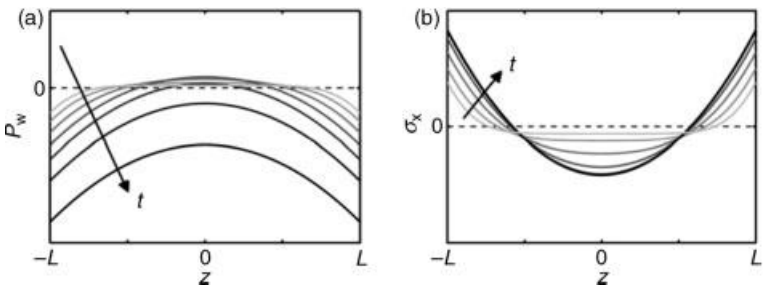

Fig. 5.18 Drying of an elastic gel plate (thickness 2L): qualitative profiles of (a) liquid pressure and (b) in-plane stress as evolving in time.

(For extremely high drying rates, when the liquid pressure only drops at the surface, the stress assumes the highest possible value, namely capillary pressure in Eq. 5.7.)

In the above model, shrinkage is not explicitly accounted for, but – taking a Lagrangian approach – the obtained profiles are still meaningful for a time-dependent plate of thickness L, if shrinkage is (nearly) uniform. Furthermore, constant material properties have been assumed which is certainly not allowed when the gel shrinks significantly. Despite these simplifications, the analysis is very helpful to identify the crucial parameters for preventing structural damage during drying: harmful stress increases with higher drying rate, larger sample thickness and lower permeability.

A similar derivation can be done for gels that have a *viscous* solid network. Then, the constitutive equation for the wet gel is given by the relation between strain rate and stress

$$\dot{\varepsilon}_x = \frac{1}{F}\left[\sigma_x - N(\sigma_y + \sigma_z)\right] + \frac{P_w}{3K_G} \tag{5.18}$$

where F is uniaxial solid viscosity, K_G bulk viscosity and N the corresponding Poisson's ratio. The local volumetric strain rate is a function of average and local liquid pressure

$$\dot{\varepsilon} = ((1-C_0)\langle P_w\rangle + C_0 P_w)/K_G \tag{5.19}$$

and can be linked to Eq. 5.13 to get a pressure profile that is constant in time. As above, the gel is assumed highly compressive, and local stress is computed from Eq. 5.16. Figure 5.19 shows how profiles of pressure and stress in the saturated gel depend on the two parameters

$$C_1 = L\sqrt{\frac{\mu_w}{3\,KK_G}} \text{ and } C_2 = \frac{3\,K_G\dot{m}_v}{\varrho_w L} \tag{5.20}$$

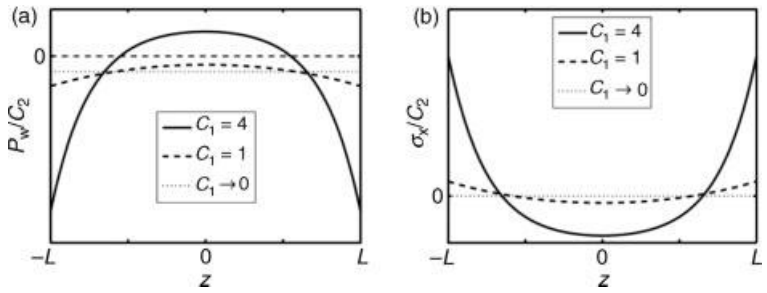

Fig. 5.19 Drying of a viscous gel plate (thickness 2L): qualitative static profiles of (a) liquid pressure and (b) in-plane stress.

(C_1 is a measure of the resistance that the pore liquid offers to contraction of the solid phase.) The maximum tensile stress, occurring at the plate surface, is given by

$$\sigma_x|_{z=L} \approx C_2\left(\frac{C_1 \cosh C_1}{\sinh C_1} - 1\right) \tag{5.21}$$

Again, the analysis is simplified by taking material properties constant and neglecting shrinkage. Furthermore, and unlike Scherer, we have neglected syneresis, that is, gel shrinkage due to restructuring of the solid network by continuing condensation reactions. Nevertheless, we find that, as for the elastic plate, higher drying rate, larger sample thickness and lower permeability increase the stress. In fact, Eq. 5.21 is approximated by Eq. 5.17 for small C_1; for high C_1, stress increases with increasing gel viscosity K_G. It must be stressed that, in reality, there is a time dependence, since the gel stiffens and becomes less permeable as it shrinks; therefore, during drying, liquid pressure gradients increase and stress reaches a *maximum* when the menisci are fully developed and the surface pores start to dry out – just as in the elastic case.

So far, we have only presented two limiting cases, the purely elastic and the purely viscous gel. Generally, one may say that the viscous model describes the compliant gel during the early stage of drying and that the elastic model is suited for later stages when the gel has become more rigid and the menisci are about to enter the gel. Of course, the mechanical behavior of real gels is more complex, and, for quantitative results, numerical solution with an explicit description of shrinkage is needed, for example, Scherer (1987b), and a combined model seems more appropriate, for example, for the start of drying (Scherer, 1988). Besides a good choice of the mechanical model, material parameters are a difficult issue. One method that proved to be elegant and accurate is a three-point bending test in which viscoelastic properties and permeability are estimated simultaneously (Scherer, 1992b).

The present overview was restricted to models that are only valid during the first drying period. However, this is sufficient for our discussion on structural damage since the highest stress level is attained at the critical point, when the solid network can no longer (or not fast enough) contract under capillary pressure and the liquid/gas interface starts to recede from the gel surface. Beyond this point, the liquid pressure at the liquid/gas interface remains constant and is given by Eq. 5.7 whereas both drying rate and distance for liquid flow decrease as the evaporation front recedes. Consequently, in the wet gel region, pressure differences can be leveled out and stress will disappear during the second drying period. (Due to the small pore size and the narrow size distribution, both not favorable for sustained capillary flow, all of the surface is expected to dry out rapidly so that the constant rate period is not extended significantly beyond the critical point.)

5.4.1.4 **Cracking**

The tensile stresses that have been derived for the first drying period can, in principle, on their own lead to failure of the gel. But mostly, cracks arise from the propagation of small mechanical defects under macroscopic tension. The material on either side of the crack can contract more freely so that the stress is partially relieved (see

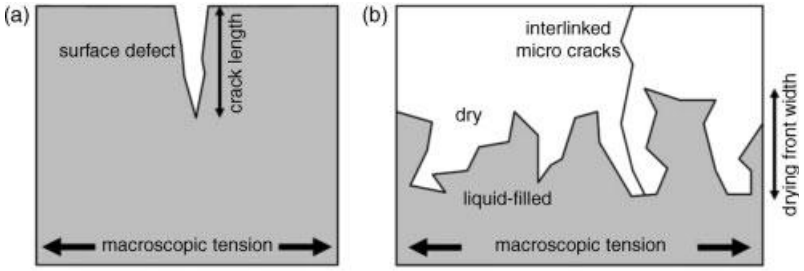

Fig. 5.20 Different explanations for crack initiation: (a) pre-existing surface defect or (b) micro cracks caused by local capillary forces.

Fig. 5.20a). The stress concentrated at the tip of the crack is proportional to the macroscopic tensile stress σ_x and the square-root of crack length c. If it exceeds the critical stress intensity I_{cr}

$$1.1\sigma_x\sqrt{\pi c} > I_{cr} \tag{5.22}$$

the crack will propagate catastrophically since crack-tip stress continuously increases. For constant macroscopic tension, a critical crack length can be defined. This theoretical description has been nicely confirmed on gels by bending experiments on notched beams and on beams with defined surface roughness (Alaoui *et al.*, 2000).

However, as we have seen above, the stress level rises gradually during the first drying period and experiences no dramatic change at the transition to the second drying period. Therefore, propagation of surface defects does not seem an appropriate explanation of why cracks usually occur at that very moment (Simpkins *et al.*, 1989).

According to Scherer, another mechanism is responsible: as liquid menisci enter the gel, capillary forces that held the pore walls together during the first drying period are switched off locally; by this, micro-cracks are initiated at the pore scale (see Fig. 5.17b). As the drying front advances, these micro-cracks can link together. The drying front has an irregular shape and its width decreases with increasing drying rate (Shaw, 1987); these effects result from the size distribution of pores and the viscous capillary flow that tries to keep small pores saturated. Pore network models, as presented in Chapter 2 of Volume 1 of this series, can help to study these phenomena (Vorhauer *et al.*, 2010).

The interlinked micro-cracks are under macroscopic tension over the width of the drying front, that is, the partially saturated region (see Fig. 5.20b). If this part of the crack exceeds the critical length, it can propagate catastrophically. With increased drying rate, the macroscopic stress increases linearly, and this cannot be compensated by the reduction of drying front width so that faster drying results in material failure whereas slow drying can prevent it. If the macroscopic stress is small, the micro-cracks will not propagate into macro-cracks, but rather heal when drying is complete.

Gel size has no influence on the drying front width, but larger gels develop higher stresses so that the proposed hybrid model of macroscopic stress and local failure can also explain why larger gels are more likely to crack.

Scherer further argues that local stresses alone cannot be the reason for macroscopic cracks, because gels that are too large or dried at too high rates generally break into only a few pieces. If the reason were the local pressure differences between pores (or pore regions) of different saturation status, then the gel sample should rather be pulverized – irrespective of drying rate and sample size.

So, besides macroscopic tension, the irregular interface of the fractal drying front is thought to play a crucial role in crack formation. There is experimental evidence for the existence of liquid and dry patches at the phase front, which are significantly larger than the pore size: during drying of porous glass, the partially saturated region of the drying front becomes opaque (Scherer, 1992a) because these patches scatter the light (unlike the much smaller pores themselves). It is still not clear whether the irregular shape of the phase front harms by generating defects or beneficially diffuses the stress. Since such an irregular front cannot be modeled by a continuum approach, only pore-scale models, as discussed in Section 5.6.2, are expected to bring more light to this interesting problem.

In the above expressions for gel stress, the liquid pressure level does not appear explicitly. Nevertheless, capillary pressure plays a crucial role because it decides to what extent the material will shrink, and thereby determines how much the gel stiffens and by how much its permeability is reduced. Consequently, lowering the capillary pressure – by increasing pore size, reducing surface tension or increasing contact angle – is beneficial for product quality because it reduces the maximum tensile stress.

So far, the qualitative recommendations to avoid cracks – besides reducing sample size and drying at a low rate – may be summarized as:

- Increase the gel strength (or the critical stress intensity I_{cr})
- Increase the pore size for higher permeability and lower capillary pressure
- Use low-surface tension pore liquid and increase the contact angle for reduced capillary pressure.

We conclude with a remark on phenomena at the end of the convective drying process. As the outer regions of the gel become completely dry, the compressive action of capillary pressure is eliminated and for (partially) elastic material behavior, springback, that is, re-expansion of the gel network may be observed. The interior regions are still under compression so that stress is reversed. This effect is nicely proven by experiment: a plate that is dried from one side is curved towards the open surface during the first drying period; during the second drying period the curvature is away from the open surface (Scherer, 1987c). Such stress reversal may also lead to cracks at the very end of drying when the wet region becomes small (Simpkins *et al.*, 1989).

5.4.2
Freeze-drying

After seeing the problems in convective drying because of capillary forces, one is inclined to test a drying technique that does not involve a liquid/vapor phase boundary. The most evident alternative is freeze-drying, which is widely used for

thermosensitive products, mainly foods and pharmaceuticals, and when the solid structure is to be preserved, for example, in biological samples. Therefore, it seems quite surprising that this alternative should also face severe problems – producing powder or very coarse pore structure (Scherer, 1992a). One straightforward explanation again involves capillarity, when residual pore liquid exists because of incomplete freezing or a too early temperature rise at the end of the drying process. This has indeed some significance if we recall that the melting temperature is much lower in small pores (see thermoporometry in Section 5.3.1.2).

However, Scherer (1993) points out that it is the freezing step itself that can destroy the fragile gel structure. One mechanism which may lead to damage by freezing is the *density change* during solidification of the pore liquid. For water, the specific volume increases by roughly 9%. Depending on the freezing conditions and pore size distribution, different scenarios can be imagined. For a significant temperature gradient, for example, if the wet gel is immersed into a cold liquid, an ice crust may form at or near the surface of the gel. When the inner regions freeze, and expand, this crust will fracture easily, rather than inhibiting crystallization. If the temperature is lowered uniformly, then, for distributed pore size, liquid starts to freeze in the larger pores, for which the required undercooling is less (see thermoporometry in Section 5.3.1.2), and a percolating ice network gradually builds up, which is broken when the liquid in the smaller pores freezes. Also, if we assume that the liquid solidifies simultaneously in all the pores, because of a uniform pore size, a pressure builds up that must be released. For a volume increase during solidification, the damaging effect seems very obvious, but also, if the solidified solvent has less volume than the liquid, as is normal, a significant tension builds up that is likely to destroy the already frozen pore regions.

Interestingly, it is another phenomenon that is likely to destroy the freezing gel, independent of the density change. If an ice layer forms at the surface of a gel, then we have the situation as in Fig. 5.5, that significant undercooling is required for the ice to penetrate the small pores. Alternatively, *liquid may be drained* from the pores and solidify on the crystal surface, as depicted in Fig. 5.21a. Since the growth of ice crystals is rather fast – Scherer estimates a front velocity $u = 0.1\ \mathrm{mm\,s^{-1}}$ for an undercooling of $\Delta T = 0.2\ \mathrm{K}$ – the liquid flow out of the wet gel may be orders of magnitude higher than during evaporative drying.

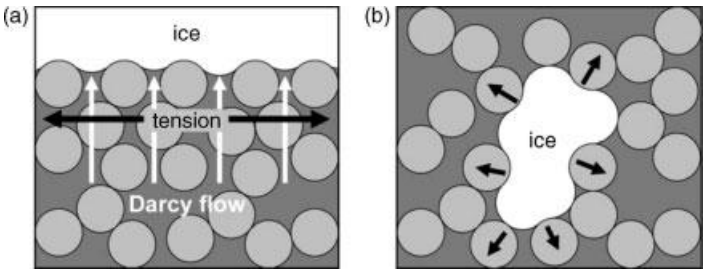

Fig. 5.21 Freezing of gels: (a) drainage of liquid to ice at gel surface with tension build-up; (b) ice crystal growing inside the gel and pushing primary particles apart.

The destructive effects, such as differential shrinkage and tensile stress at the gel surface, are of the same kind in both cases, so that for the freezing process, maximum tensile stress can be computed analogously to Eq. 5.17 as

$$\sigma_x \approx \frac{\mu_w u L}{3K} \tag{5.23}$$

But freezing, as compared to convective drying, takes minutes rather than hours or days, so that stresses higher than the modulus of rupture can develop, and failure even occurs without the mechanism of crack propagation. The resulting fragments themselves will be subjected to the same process of liquid drainage to a surface layer of ice. Breakage into finer fragments will continue until fragment size L is small enough for the gel to withstand the tensile stress σ_x in Eq. 5.23.

If crystals nucleate inside the gel, as can be promoted by incorporating a catalyst into the gel network, then large undercooling is required for the penetration of ice into the small neighboring pore openings. Again, liquid will rather flow towards the ice crystal, which itself pushes the primary particles apart as it grows (see Fig. 5.21b), the phenomenon being analogous to frost heave in soil. Such growth of internal ice crystals may result in large pores of the freeze-dried gel, or cause macroscopic cracks when the gel cannot withstand the developing stress.

Scherer also addresses gel *shrinkage* during freezing and finds that the gel is subjected to the maximum compressive pressure when flow towards a surface ice crystal is stopped by liquid/vapor menisci in other surface regions, and the ice crystal finally penetrates the pores. Then, the pressure in the liquid is

$$P_w = -\frac{2\sigma_{c,l}}{r_p} \tag{5.24}$$

where $\sigma_{c,l}$ is the interface tension between crystal and liquid (approx. 0.04 N m^{-1} for water) and r_p the pore radius. So, shrinkage is expected to be less pronounced than during convective drying, for which capillary pressure, Eq. 5.7, sets the condition for compressive pressure.

In order to reduce the damage to gels during freezing, we may conclude that the density change in the pore liquid during solidification should be small and that crystal growth from the gel surface should be avoided in favor of nucleation inside the gel. A more detailed analysis of the stress exerted on the solid network by internal ice crystals (Scherer, 1993) reveals that the pore liquid should also have low entropy of fusion. For limited shrinkage, the interface tension between crystal and pore liquid $\sigma_{c,l}$ should be low. And, most evidently, the gel strength plays a crucial role and should be as high as possible. Scherer also points out that very fast freezing could prevent damage because it would make the liquid vitrify rather than crystallize.

Once the gel is frozen, it is sublimation-dried under vacuum. Care must be taken that the ice does not melt and that drying is complete before the temperature is raised to ambient in order to avoid further damage to the gel. Concerning the drying step, freeze-drying has the disadvantage of long process times, since the drying rate is limited by the saturation vapor pressure of ice that is generally very low.

5.4.3 Supercritical Drying

5.4.3.1 Supercritical Drying of the Initial Solvent

Having seen that even costly freeze-drying is no evident solution, we turn to the drying technique that first produced highly porous dry gels, namely supercritical drying. The most obvious method is to take the wet gel as it is and transfer the pore liquid into its supercritical state. This is done by heating the gel in an autoclave in order to reach the supercritical state by increasing both temperature and pressure (see Fig. 5.14). For the following reason, it is crucial to place the wet gel in a bath of sufficient excess liquid (Phalippou *et al.*, 1990): during heating, the liquid expands and part of it evaporates until the whole autoclave is either filled by liquid or vapor, and only further heating makes the fluid supercritical. There must be more initial liquid per autoclave volume than the critical density, for example, $0.28\,\mathrm{g\,cm^{-3}}$ for methanol and ethanol, to keep the gel covered by liquid and avoid evaporative drying of the gel during the heating step – with capillary effects. (Alternatively, the autoclave may be pressurized by an inert gas before heating.) The critical values for some single-component solvents relevant in gel synthesis are given in Tab. 5.1. If the pore liquid consists of several components, the situation is more complicated because, then, the mixture must be supercritical (Phalippou *et al.*, 1990).

The *heating* rate $\mathrm{d}T/\mathrm{d}t > 0$ must not be too high to avoid non-uniform thermal expansion of the gel, especially the pore liquid, with the risk of damage. Scherer (1992c) has derived the stress in a heated gel cylinder (of radius R), which arises from the difference between the thermal expansion coefficients of liquid and solid, $\Delta\alpha > 0$, and low gel permeability that hinders the expanding liquid from flowing out of the gel. He finds a long-time solution for axial stress at the cylinder surface that is valid for compliant gels, both elastic and viscous,

$$\sigma_z|_{r=R} \approx \frac{3\mu_w R^2}{8K}\left(\psi\,\Delta\alpha\frac{\mathrm{d}T}{\mathrm{d}t}\right) \tag{5.25}$$

where the term in brackets is the thermal strain rate. If syneresis, and the corresponding shrinkage of the solid network, is accounted for, the stress is increased by an additional strain rate. The analysis further shows, that mechanical constraints of the gel should be avoided, otherwise significantly higher stresses may

Tab. 5.1 Critical constants for different solvents (Hüsing and Schubert, 2006).

	T_{cr} (°C)	P_{cr} (MPa)
methanol	240	7.9
ethanol	243	6.3
isopropanol, acetone	235	4.7
water	374	22.1
carbon dioxide	31	7.3

develop. From time-dependent calculations, with silica gel and methanol as the pore liquid, Scherer can explain experimental observations, in which gel cylinders of diameter 6 cm crack at a heating rate of $2\,\mathrm{K\,min^{-1}}$, but stay intact when heating at $0.3\,\mathrm{K\,min^{-1}}$.

After reaching the supercritical state, the pore fluid is removed by venting the autoclave. This *depressurization* is usually done under isothermal conditions to avoid the risk of condensation, and it must be slow enough to prevent significant stresses in the gel because the fluid cannot escape instantaneously but expands within the gel and causes the solid network to swell. Scherer (1994) has investigated the limiting conditions for the depressurization rate $\mathrm{d}P/\mathrm{d}t < 0$: assuming ideal gas behavior during the expansion, he obtains the following approximate expression for the maximal axial tensile stress at the surface of a gel cylinder (attained at the end of depressurization):

$$\sigma_z^{\max}|_{r=R} \approx R\sqrt{\frac{\psi\,\mu_w}{4\pi K}\left|\frac{\mathrm{d}P}{\mathrm{d}t}\right|} \tag{5.26}$$

The influence of sample size and depressurization rate has also been studied experimentally for different silica gels (Woignier *et al.*, 1994). For all gels, there was a maximum rate below which the samples stayed monolithic and above which they cracked. The obtained results were in reasonable agreement with a more advanced model than Eq. 5.26 (Scherer, 1994). For cylindrical samples with both diameter and height equal to 3 cm, the maximum depressurization rate is around $0.1\,\mathrm{MPa\,min^{-1}}$ (see also Sakka and Kozuka (2005)). Further analysis for ethanol shows that the process time can be significantly reduced by decreasing the depressurization rate during the process, since for an identical decrease in pressure, the (non-ideal) gas expands much more at lower pressures (Woignier *et al.*, 1994).

Near atmospheric pressure, the autoclave is flushed with an inert gas, for example, nitrogen, to prevent condensation in small pores (Sakka and Kozuka, 2005). Finally, the autoclave is cooled down – again slowly to avoid mechanical damage.

The above-described supercritical drying route is simple in theory but, in practice, has several disadvantages which come from the elevated critical parameters of the solvents used in gel synthesis (see Tab. 5.1). High temperatures and pressures, especially in large volumes of an industrial production, cause a considerable safety problem, and organic solvents bear the additional risk of inflammability. But further than this, the gels may undergo undesired structural changes at the elevated temperatures. Parts of the solid network may form crystals, or may be destroyed by the rather corrosive alcohol or water, and the elevated temperatures will enhance the above-described effects of ripening, that is, elimination of small pores by dissolution and re-precipitation, and syneresis, that is, formation of new bonds when distinct branches of the gel network approach each other by thermal fluctuations. During syneresis in silica gels, water is produced, so that the pore liquid changes composition and the initial critical conditions may not be enough to avoid capillary effects. It should be noted

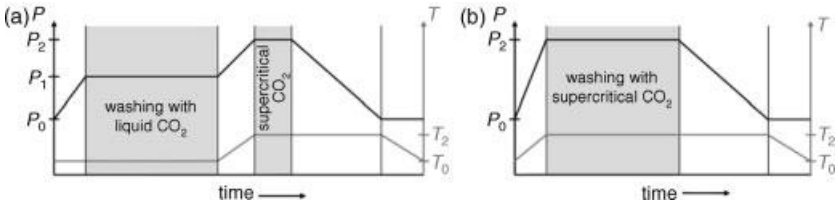

Fig. 5.22 Pressure and temperature protocols for different drying methods with supercritical CO_2 (ambient and supercritical conditions are denoted by indices 0 and 2, respectively).

that significant shrinkage (around 40% in volume) may occur during the described route of supercritical drying (Roig *et al.*, 1998).

5.4.3.2 **Low-Temperature Process with CO_2**

In order to circumvent the problems associated with the high critical temperatures of the pore liquid, a low-temperature supercritical drying route has been proposed (Tewari *et al.*, 1985): it involves carbon dioxide, which has a low critical temperature and is inert. Due to the smaller temperature variation, the supercritical drying step can be several times shorter; however, a washing step is needed to replace the pore liquid by liquid carbon dioxide (see Fig. 5.22a). This is done in the autoclave at or near room temperature (at 20 °C, CO_2 is liquid for $P_1 > 5.6$ MPa); again, the gel is initially covered by excess pore liquid, which is purged at elevated pressure before the actual washing step can start (liquid CO_2 floats on top because of its low density) (Masmoudi, 2006). If the original pore liquid is not miscible in carbon dioxide, as is the case for water, it must first be substituted by an intermediate, for example, alcohol or acetone. Typically, these washing steps require many hours because the transport mechanism is diffusion; and the characteristic time increases with the square of the gel dimensions. Washing with liquid CO_2 is done by rinsing the pressure vessel, and the concentration of the initial pore liquid is monitored by on-line gas chromatography; when it is lower than a critical value, for example, 10^{-3} of the initial concentration (Heinrich *et al.*, 1995), the liquid is transferred into its supercritical condition. Isothermal depressurization and cooling of the autoclave conclude the drying process (see Fig. 5.22a).

Significant improvement of this supercritical drying method can be achieved if the washing step itself is done with supercritical CO_2, as illustrated in Fig. 5.22b, because the diffusion process is significantly faster for this fluid (Bisson *et al.*, 2003). It is, however, not sufficient to be in the supercritical state of the single component CO_2; instead, the mixture of CO_2 and pore liquid must be supercritical. Taking a single-component pore liquid, for example, ethanol, then, for any temperature above the critical temperature of CO_2, there is a critical pressure (Schneider, 1978). In Fig. 5.23, these values are connected to a binary critical curve. Above this curve, the two phases are a completely miscible supercritical fluid; below the curve, liquid ethanol coexists with gaseous CO_2. The consequences for the washing step are clear: if the system is biphasic, capillary effects are expected to destroy the gel. Van Bommel and

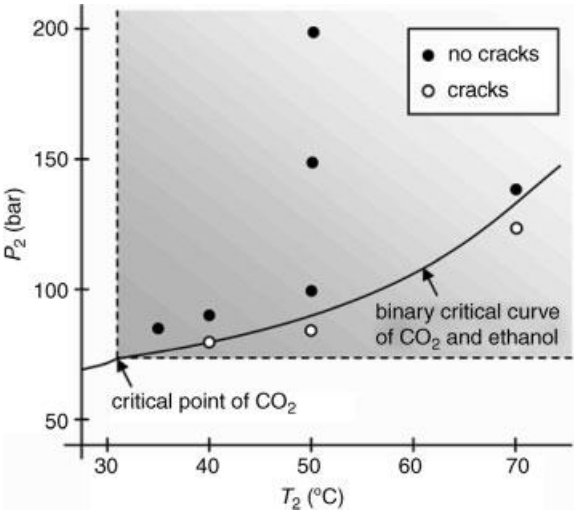

Fig. 5.23 Occurrence of cracks in gels dried with supercritical CO_2 depending on washing parameters as defined in Fig. 5.22b (taken from van Bommel and de Haan (1994)). (The shaded region marks the supercritical state of the single component CO_2).

de Haan (1994) have confirmed this expectation by the experimental results shown in Fig. 5.23. Monolithic aerogel rods (ø 1.5 cm) could be obtained after supercritical washing with CO_2 for 3 h at as moderate conditions as 35 °C and 8.5 MPa and depressurization in less than 1 h.

The same authors proved experimentally that recycle of the washing fluid is possible by first separating the ethanol (at 20 °C), then liquefying CO_2 (at 5 °C), both at reduced pressure (5.0 MPa), and finally heating it back to the supercritical state. They designed a semi-continuous industrial production plant for aerogel plates of 3 cm thickness, in which five autoclaves operate in turn and water could be used for cooling and heating. Due to longer diffusion times and lower depressurization rates (about 0.1 MPa min^{-1}) for the thick plates, a cycle time of 16 h was estimated.

It may be concluded that the supercritical route is most successful in preserving the gel during the drying step. Due to the absence of interfacial forces, both shrinkage and cracks can be successfully avoided. The standard technique uses carbon dioxide for its moderate critical values, and the necessary washing step is mostly done under supercritical conditions. In the frame of two recent European research projects (HILIT and HILIT+, 1998–2005), large monolithic silica aerogels for windows ($55 \times 55 \times 1.5\,cm^3$, see Fig. 5.24) could be successfully produced by this route (Masmoudi, 2006).

Recent experimental work aims to optimize synthesis and aging conditions for producing aerogels with increased mechanical strength and good transmission properties in a reasonable processing time (Strøm *et al.*, 2007); and to estimate effective diffusion coefficients for optimizing the washing with supercritical CO_2 (Masmoudi *et al.*, 2006). Theoretical work has tried to predict this coefficient from

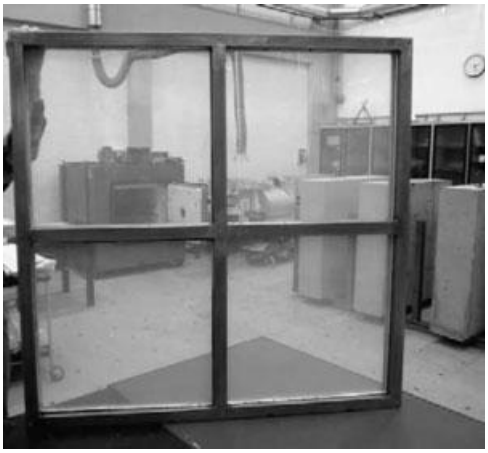

Fig. 5.24 Highly insulating and light transmitting (HILIT) aerogel glazing; aerogel sheet is placed between two glass panes and evacuated (taken from Jensen *et al.* (2004)).

molecular and Knudsen diffusivities accounting for the pore size distribution of the gel (Orlovic *et al.*, 2005).

In the next section, we will present experimental efforts to look for alternatives to the high-pressure process of supercritical drying. The goal is the production of highly porous dry gels by subcritical and ambient pressure routes or by freeze-drying.

5.5
Advanced Drying Techniques – Preserving Quality

Having seen that supercritical drying can produce large monolithic highly porous dry gels of high quality, we will now show how less expensive and safer alternatives can compete with it. In principle, all other techniques are more harmful to the gel structure, and new approaches had to be developed to limit the damage during drying.

The assignment of literature work to subsections on freeze-drying (Section 5.5.2), vacuum drying (Section 5.5.3) and convective drying (Section 5.5.4) accounts for the historical context and is not strict, because different drying techniques have often been compared in one and the same work.

5.5.1
Subcritical Drying

Only recently, the possibility of using subcritical drying techniques to produce xerogels has been explored; most of them will be treated in Sections 5.5.3 and 5.5.4 on vacuum and convective drying, respectively. Here, only one method close to supercritical drying as followed by Kirkbir *et al.* (1998a, b) will be presented. Wet silica gels were first washed (e.g., with ethanol) and then heated in a pressure

chamber. During heating to about 250 °C, the pressure increase first followed the vapor-pressure curve of the solvent until all solvent was evaporated (e.g., at 213 °C and 3.5 MPa); further pressure increase was due to vapor expansion up to a maximal pressure (e.g., 4.4 MPa) well below the pressures required in supercritical drying (e.g., >6.4 MPa). Similarly, different maximum pressures were adjusted and several solvents investigated. In this drying method, capillary forces do develop, but are reduced due to solvent exchange and elevated temperatures. Additionally, the solvent exchange may induce structural changes and thereby influence gel behavior.

From silica gels with moderate porosities (80–90%), large crack-free monoliths (e.g., cylinders with ø 5.6 cm and length 25 cm) could be prepared over wide ranges of maximal pressures. For ethanol as the pore liquid, no cracks were observed; additionally, shrinkage was negligible above a subcritical threshold whereas, below that pressure, the gel shrank significantly (linear shrinkage of 20% and more). For isobutanol, shrinkage was only observed at atmospheric pressure, but gels cracked below a threshold pressure.

These threshold pressures are related to the temperature at which the gel dries out and, hence, to the maximal surface tension that the gel experiences; they depend on synthesis conditions which control the structural and mechanical properties of the gel, such as pore size and strength, respectively. Although process pressures can be significantly reduced (by 50%) by this approach, the previously described problems associated with the elevated temperatures remain.

5.5.2 Freeze-Drying

5.5.2.1 General Remarks

Freeze-drying is an alternative to avoid liquid/vapor interfaces, as water is removed by sublimation after the freezing step. As indicated in Section 5.4.2, damage by cracks can be reduced by a pore liquid with low density change and low entropy of fusion; furthermore, a high freezing temperature is desirable for easy and complete freezing, and the saturation vapor pressure should be elevated for short drying times. One prominent substance fulfilling these requirements is *tert*-butanol $(CH_3)_3COH$ (see Tab. 5.2); from its low entropy of fusion, it is expected to have a low crystal–liquid interface tension so that gel shrinkage should also be limited (Scherer, 1993).

Tab. 5.2 Material properties relevant for freeze-drying.

	Freezing temperature (°C)	Density change during freezing (%)	Entropy of fusion ($J\,cm^{-3}\,K^{-1}$)	Saturation vapor pressure at 0 °C (Pa)
water	0.0	−8.5	1.2	61
tert-butanol	25.8	−0.04	0.24	821

It seems to be difficult to produce high-porosity monoliths from inorganic gels by freeze-drying. In an early work, Degn Egeberg and Engell (1989) could produce large *silica* cryogels of elevated porosity (>70%) that cracked into several large translucent *pieces*. Without solvent exchange, or if not enough washing steps were used, small cryogel *flakes* were obtained; the authors attribute this to incomplete freezing of residual pore liquid (especially ethanol with a freezing point of −117 °C), which subsequently boils during vacuum freeze-drying. Pajonk *et al.* (1990) report silica cryogels that have been produced as *powders* with relatively low density ($\geq 0.2\,\mathrm{g\,m^{-3}}$), but with less pore volume and lower surface area than the corresponding aerogels. Structural properties closer to those of aerogels could be obtained by aging to strengthen the gel (as described below) or by synthesis under basic conditions for larger pore size.

In contrast, the method is successfully used for *RF gels* (Mathieu *et al.*, 1997) probably because these organic gels have a strength and elasticity that can better withstand the stresses during freeze-drying (Kocklenberg *et al.*, 1998).

Before presenting literature results on RF cryogels, we will provide some background knowledge on RF gels that has been acquired from supercritical drying and subsequent pyrolysis of these organic gels. Bock *et al.* (1997) studied RF gels with a target density of $0.35\,\mathrm{g\,cm^{-3}}$ (with *skeletal density* $\varrho_s \approx 1.5\,\mathrm{g\,cm^{-3}}$, corresponding to porosity $\psi \approx 77\%$) and systematically varied the molar R/C ratio. By nitrogen adsorption, SAXS and TEM measurements, they could show that for an increase in this synthesis parameter from 100 to 800 and above, the particle and pore radius are increased from below 5 nm to above 50 nm. At the same time, the BET surface area of RF aerogels decreases from above $600\,\mathrm{m^2\,g^{-1}}$ to below $100\,\mathrm{m^2\,g^{-1}}$ (for R/C = 1500); after pyrolysis at 1050 °C, this variation is reduced to the range 600–400 $\mathrm{m^2\,g^{-1}}$. The specific volumes of mesopores ($2\,\mathrm{nm} < d_p < 50\,\mathrm{nm}$), which correspond to voids between the primary particles of the gel, and micropores ($d_p < 2\,\mathrm{nm}$), which are voids inside these particles, are suitable criteria to measure the quality of the dry gels. Both are of specific interest for high-surface-area applications, whereas macropores only contribute to porosity, that is, accessibility of the small pores and low overall density. During pyrolysis, mass loss and volumetric shrinkage (both about 50%) are observed so that the solid density is increased, but the porosity remains almost constant; further, the pore size distribution is shifted to values about one third smaller, and micropores are created.

Tamon *et al.* (1998) were interested in RF dry gels as precursors for mesoporous carbon with porosities > 80% and surface areas $> 800\,\mathrm{m^2\,g^{-1}}$ for applications in adsorption, chromatography, catalysis, and as electrodes. Their supercritical drying experiments are complementary to those of Bock *et al.* (1997): by varying R/C from 12.5 to 100 and using different dilution ratios, they show that the mesopore volume and peak radius of monomodal pore size distribution of RF aerogels can be engineered; they describe the same behavior during pyrolysis (mesopore volume reduction, decrease in peak radius, unchanged shape of pore size distribution and moderate increase in BET surface area). An increase in pyrolysis temperature (from 500 to 1000 °C) results in more shrinkage, but leaves the peak radius unchanged.

5.5.2.2 RF and Carbon Cryogels

The first RF cryogels were prepared by Mathieu *et al.* (1997) and Kocklenberg *et al.* (1998); they varied the R/C ratio between 50 and 250, used different dilution ratios and aging times, and characterized the pore structure of the resulting cryogels by nitrogen sorption, mercury porosimetry and SAXS measurements. They reported monolithic structures with good cohesion, high BET surface areas ($\geq 450\ m^2\ g^{-1}$), a mesopore volume of about $0.5\ cm^3\ g^{-1}$ and a micropore volume of about $0.2\ cm^3\ g^{-1}$.

At the same time, Tamon and coworkers started exploring alternatives to the expensive and dangerous supercritical route for producing carbon precursors, with a focus on freeze-drying (Tamon and Ishizaka, 1999; Tamon *et al.*, 1999). The gels were synthesized from resorcinol, formaldehyde (37% in methanol), sodium carbonate and distilled water (W) with two different R/C ratios (25 and 200) and two different dilution ratios R/W (0.125 and $0.25\ g\ cm^{-3}$). The solution was poured into glass tubes (ø 4 mm, 4 cm long) and gelled and cured for 1 day at 25 °C, 1 day at 50 °C and 3 days at 90 °C. Then, different drying routes were used to produce RF dry gels:

- **Supercritical drying**: the hydrogel is first washed with acetone (>1 week), then dynamically washed with liquid CO_2 (2 h) and with supercritical CO_2 (4 h).
- **Freeze-drying**: the hydrogel is immersed in 10 times its volume of *tert*-butanol (>1 d, repeat three times), then frozen (at −30 °C for 1 h) and freeze-dried (at −30 °C for 1 d, then at −10 °C for 1 d, then at 0 °C for 1 d).
- **Vacuum drying**: at room temperature.
- **Hot air drying**: at 50 °C.

All dry gels are aged (at 250 °C for 8 h) and characterized by nitrogen sorption. The results, reported in Fig. 5.25 and Tab. 5.3, indicate that freeze-drying produces more shrinkage and less mesopore volume than supercritical drying, but is still much better than the evaporative drying routes. Furthermore, this quality loss can be compensated by subsequent pyrolysis (heating rate $250\ K\ h^{-1}$; first to 250 °C and hold for 2 h; then to 1000 °C and hold for 4 h). Both aerogel and cryogel undergo significant volumetric shrinkage (>70%) that is reflected in a loss of macropore volume, but their porosity stays high (>80%) because of mass loss during carbonization.

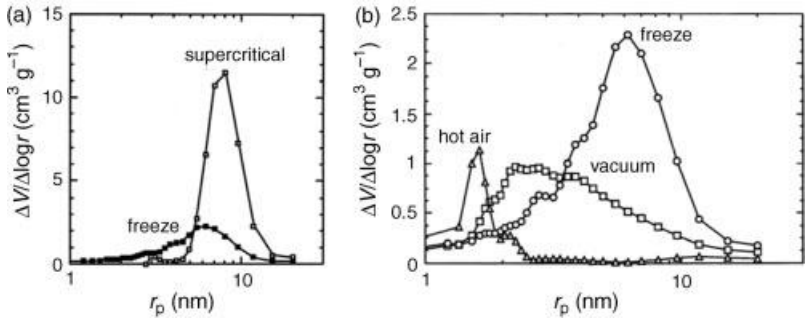

Fig. 5.25 Size distribution of mesopores in dry RF gels (R/C = 200, R/W = $0.25\ g\ cm^{-3}$) for different drying methods (from Tamon *et al.* (1999)).

Tab. 5.3 Structural properties of dry RF gels (R/C = 200, R/W = 0.25 g cm^{-3}) for different drying methods (from Tamon *et al.* (1999)).

	Volumetric shrinkage (%)	Dry gel porosity (%)	Mesopore volume (cm^3 g^{-1})	Macropore volume (cm^3 g^{-1})
supercritical drying	12	85	2.71	0.91
freeze-drying	25	79	1.02	1.42
vacuum drying	33	(no data)	0.62	(no data)
hot air drying	82	35	0.18	0.15

The mesopore volume of the cryogels is increased so that mesopore volumes around 1.5 cm^3 g^{-1} and BET surface areas in the range 900–1200 m^2 g^{-1} can be achieved for *both* supercritical and freeze-drying.

After these encouraging results, the influence of freezing and freeze-drying conditions on gel quality was investigated further (Tamon *et al.*, 2000; Yamamoto *et al.*, 2001a, 2005). For identical synthesis conditions as above, the pore liquid, washing protocol and temperature protocol during freezing and freeze-drying were varied.

If the gel was rinsed in *distilled water* (>1 d), it did not stay monolithic but was crushed into pieces, as expected from the theoretical considerations in Section 5.4.2. For water as the pore liquid, shrinkage is much more pronounced, the mesopores show considerable volume loss and reduction in size (see Fig. 5.26a); and the BET surface area is only 400 m^2 g^{-1}.

For solvent exchange with *tert-butanol*, the RF cryogels have a BET surface area around 550 m^2 g^{-1}, a mesopore volume around 1.1 cm^3 g^{-1} and a peak pore radius of about 6 nm. High reproducibility of these data has been proven (Yamamoto *et al.*, 2001a). It is important, that the initial pore liquid, which contains methanol and formaldehyde (with freezing temperatures below −90 °C), is sufficiently replaced, otherwise capillary forces may develop due to unfrozen residual liquid. The influence of the *number of rinses* (each 1 d) is shown in Fig. 5.26b: for only one rinse, the observed volumetric shrinkage is 55%, whereas two rinses or more can reduce this to 30%.

At a low *freezing temperature*, −196 °C (using liquid nitrogen) instead of −30 °C, undercooling is more pronounced and liquid can more easily freeze in the pores instead of flowing out of them; consequently, the pore size (and volume) is better preserved (see Fig. 5.26a).

Efforts to decrease the freeze-drying time showed that 5 d are needed at a constant temperature of −30 °C. If the process is stopped after 3 d or less, the pore liquid is incompletely removed and, after thawing, causes capillary forces and gel shrinkage to peak: consequently, the cryogels have a smaller peak pore radius (<4 nm) and reduced mesopore volume and surface area. However, by raising the *freeze-drying temperature* to −10 °C, the process can be finished in 1 d without any structural damage upon thawing.

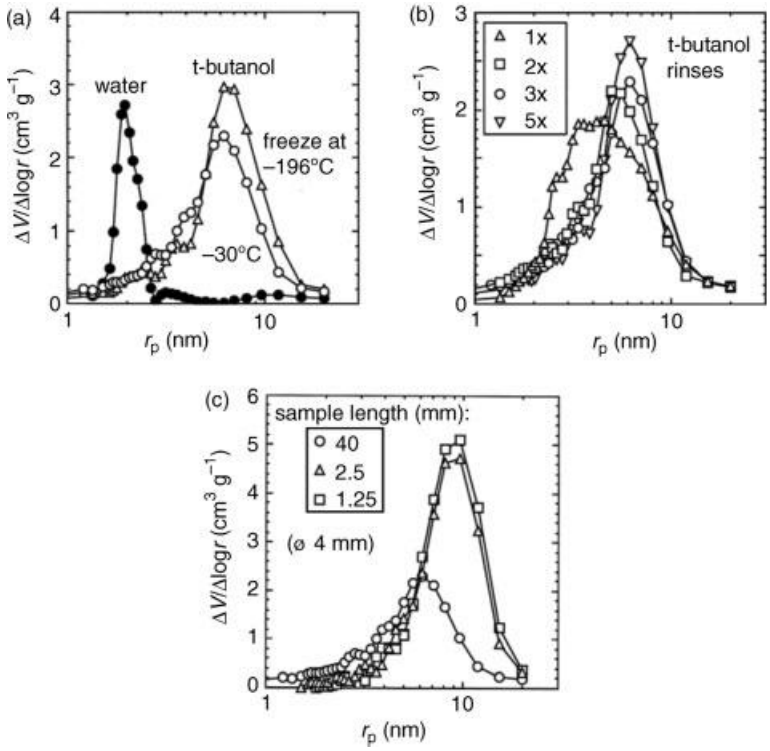

Fig. 5.26 Influence of preparation conditions on size distribution of mesopores in freeze-dried RF gels: (a) solvent (three rinses) and freezing temperature, (b) number of *tert*-butanol rinses and (c) sample size; empty circles correspond to data in Fig. 5.25b (from Tamon *et al.* (2000)).

Further, the role of sample size has been studied by cutting the wet gel cylinder into 16 or 32 slices to get cylinders of 2.5 or 1.25 mm height (ø 4 mm) before freezing (Tamon *et al.*, 2000). For smaller *sample size*, the mesopore volume can be increased to around 2 $cm^3\,g^{-1}$, and the peak pore radius to almost 10 nm (see Fig. 5.26c). (This effect is not easily explained by Scherer's work where sample size is primarily associated with stresses and potential cracks, and not with shrinkage.)

If the above described RF cryogels are pyrolyzed, BET surface areas around 900 $m^2\,g^{-1}$ and mesopore volumes around 1.5 $cm^3\,g^{-1}$ are achieved, not too far below the values of the corresponding carbon aerogels (1200 $m^2\,g^{-1}$, and 2.4 $cm^3\,g^{-1}$).

Besides drying conditions, some effort has been put into *optimizing gel synthesis* (Yamamoto *et al.*, 2001a). To this purpose a range of R/C ratios (50, 75, 100, 200) and R/W concentrations (0.125, 0.25, 0.375, 0.5 g cm^{-3}) has been studied, revealing C/W (mol m^{-3}) as a key parameter. For an increase in C/W from 5.7 to 91 mol m^{-3}, the peak radius of the carbon gels is decreased (from 7 to 1.4 nm), the mesopore volume is reduced (from 1.3 to 0.1 $cm^3\,g^{-1}$) and the BET surface area decreases (from 750 to 400 $cm^2\,g^{-1}$). At C/W > 70 mol m^{-3}, there are virtually no mesopores (i.e., pores

larger than 2 nm). The differences in the obtained gel structures are explained by the different particle growth: for high C/W (high pH), the particles of the gel are densely distributed and can only grow a little, whereas for low values of C/W, fewer particles are created and they can grow to larger sizes.

The limitation to low C/W can be overcome, if gelation is assisted by *ultrasonic irradiation*, producing so-called "sonogels" (Tonanon *et al.*, 2005). Then, also for C/W = 80 mol m^{-3}, carbon gels (ø 3 mm, 4 cm long) can be obtained with high BET surface area ($\geq$700 $m^2 g^{-1}$), significant mesopore volume ($\geq$0.6 $cm^3 g^{-1}$) and a peak pore radius of 2 nm, which is not possible by the unassisted synthesis route. Additionally, gelation times are reduced by the ultrasonic irradiation from more than 1 d to a few hours.

In the effort to replace freeze-drying by cheaper and faster *hot air drying*, the respective evolutions of pore size distribution were tracked for a gel-rod, by use of thermoporometry on the wet gel and nitrogen sorption on the cryogel and xerogel (see Fig. 5.7): whereas freeze-drying largely preserves the pore size, quality loss is observed during hot air drying due to significant shrinkage of the mesopores (Yamamoto *et al.*, 2005). Nevertheless, for particulate carbon gels, hot air drying seems to be an alternative. Wet gel *microspheres* of 30–70 μm have been synthesized by dispersing the starter solution (R/C = 400, R/W = 0.25 g cm^{-3}) into cyclohexane just before gelation, creating an inverse emulsion (Yamamoto *et al.*, 2005). Then, hot air drying (at 50 °C for 1 d) of these microspheres – in comparison to the above described process of freeze-drying – produces carbon gels with less, but still competitive, mesopore volume (0.52 $cm^3 g^{-1}$, instead of 0.85 $cm^3 g^{-1}$), the same micropore volume (0.22 $cm^3 g^{-1}$) and the same elevated BET surface area (almost 700 $m^2 g^{-1}$). This route may offer an alternative for the production of mesoporous carbon microspheres for use in, for example, adsorption techniques.

In order to save costs, not only in drying but also on the expensive raw materials, resorcinol has been replaced by the natural component wattle tannin (Tamon *et al.*, 2006a). For optimized synthesis conditions, pyrolyzed tannin-formaldehyde cryogels attained BET surface areas up to >600 $m^2 g^{-1}$ and mesopore volumes of up to 0.8 $cm^3 g^{-1}$, and are hence competitive. By additionally replacing formaldehyde with furfural, first results are promising, but more research to optimize the synthesis conditions is needed (Kraiwattanawong *et al.*, 2007).

5.5.2.3 Ice Templating (for Silica Gels)

The effects during gel freezing that are caused by liquid flow out of the pores, which are usually seen as a disadvantage, may also be used for an elegant templating technique to create engineered macromorphologies. Nishihara *et al.* (2005) studied silica cryogels obtained from controlled unidirectional freezing of pore water by immersion into a cold bath (immersion rates 6–20 cm h^{-1}; bath temperature −196 or −60 °C). After some distance, pseudo-steady-state growth of an array of polygonal ice rods in the fresh gel is observed, which serve as templates for ordered macropores in a microhoneycomb. Following low-temperature aging (−30 °C), these ice templates are removed simply by thawing (50 °C). Then, the gel may ripen for several days in a hydrothermal treatment under basic

conditions, before water (in the smaller pores) is substituted by *tert*-butanol (three one-day washings). By freeze-drying (at $-10\,^{\circ}C$) mesoporous walls are obtained; and heat treatment concludes the production process, by which large monolithic silica gels have been obtained (ø 10 mm).

The macropore size can be tuned in the range 4–40 μm since the diameter of the ice crystals depends on the immersion velocity u and the temperature difference $(T_0 - T_\infty)$ as

$$d_{ice} \propto \frac{1}{u(T_0 - T_\infty)} \tag{5.27}$$

The wall thickness can be adjusted from 0.2 to 2 μm; it is proportional to the product of the ice crystal diameter d_{ice} and the silica concentration in the starter solution. The overall porosity of the micro-honeycomb is about 94%; that of the walls around 40% (corresponding to a random packing of monosized spheres). Meso- and micro-porosity can be adjusted independently: through hydrothermal treatment the initial high BET surface area (up to $900\,m^2\,g^{-1}$) decreases and the small pores (radii < 1 nm) grow (up to 45 nm) so that mesopore volume is created. Microhoneycombs are suitable for many applications, since the macrochannels ensure a low pressure drop, and diffusion parameters in the porous walls can be engineered.

Depending on the firmness of the hydrogel, which can be tuned by synthesis parameters, several morphologies (see Fig. 5.27) are obtained (Mukai *et al.*, 2008): microhoneycombs for softer gels, and polygonal fibers for harder gels; and if the hydrosol is frozen before gelation, lamella or flat fibers result for higher or lower mobility of silica particles, respectively.

A modern use of titania–silica microhoneycombs may be in self-cleaning applications (Tamon *et al.*, 2006b): by the sol–gel process, the titania particles are more finely dispersed in the matrix than by conventional methods, and much higher BET surface areas can be reached; consequently, pulverized gels proved to have outstanding photocatalytic activity in the decomposition of large organic molecules.

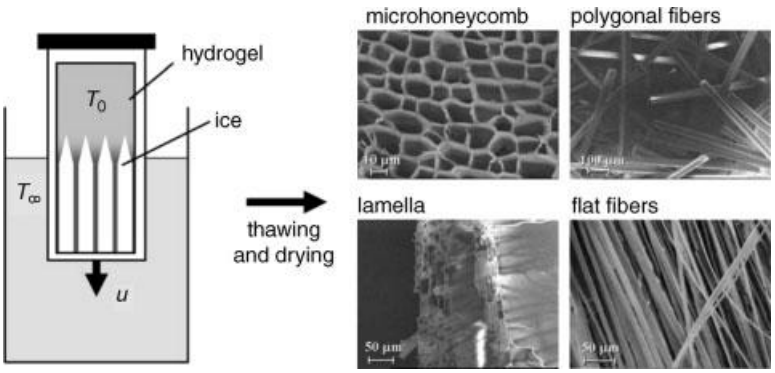

Fig. 5.27 Principle of ice templating and possible structures (adapted from Tamon *et al.* (2006b).

5.5.3
Vacuum Drying

The use of vacuum drying to obtain RF xerogels and the derived carbon materials has been explored by Job *et al.* (2004, 2005); they showed that the pore structure can be partially preserved without pretreatment. The motivation was that traditional gel-drying methods – supercritical and freeze-drying – are expensive and time-consuming and may, nevertheless, induce structural changes and quality loss; and that vacuum drying is a soft drying method.

In a first study (Job *et al.*, 2004), RF gels were prepared for several pH values (tuned by addition of sodium carbonate) and a fixed initial solid density of $0.35\,g\,cm^{-3}$ (adjusted by addition of de-ionized water) and aged at 85 °C for 3 d. The appearance of the wet gels varied from opaque and light brown at low pH (high R/C ratio) to translucent dark red at high pH (low R/C). These hydrogels were dried in a vacuum oven at 60 °C by gradually reducing the pressure from atmospheric to 1000 Pa over 5 d, and then were kept at 150 °C for 3 d. The obtained xerogels were pyrolyzed in a nitrogen atmosphere by progressively increasing the temperature to 800 °C (at $1.7\,K\,min^{-1}$ to 150 °C, held for 15 min, at $5\,K\,min^{-1}$ first to 400 °C where they were held for 1 h, then to 800 °C and held for 2 h) and then slowly cooled. Above this pyrolysis temperature, no further mass loss was observed and infrared spectra remain unchanged (Job *et al.*, 2004). The carbonized materials are black, matt (for low pH) or bright (for high pH).

In order to characterize the structure of RF and carbon xerogels, a combination of nitrogen adsorption (for micro- and meso-pores) and mercury porosimetry (for pore diameters from 7.5 to 150 nm) was used to obtain the BET surface area and pore volume (microporous and total); helium and mercury pycnometry were applied to determine the skeletal and bulk density.

During drying, the gels showed significant shrinkage but stayed monolithic. An increase in pH (from 5.45 to 7.35) results in smaller pore size – hence shifting the materials from mesoporous to microporous – and lower porosity (from 68% to only 22%). After pyrolysis, carbon gels are obtained with densities from 0.53 to $1.35\,g\,cm^{-3}$ (as compared to *skeletal density* $\varrho_s \approx 2.2\,g\,cm^{-3}$). Their BET surface areas are around $600\,m^2\,g^{-1}$ for pH < 6.5, whereas for higher pH (low R/C) no pores can be detected, but the apparent density suggests a (closed) porosity of 40%. The carbon materials possess good mechanical strength.

In a second study (Job *et al.*, 2005), vacuum drying was directly compared to supercritical drying (after washing with ethanol and liquid CO_2) and vacuum freeze-drying (with no solvent exchange and freezing with liquid nitrogen). For this comparison, different R/C ratios and two different initial solid densities (0.15 and $0.35\,g\,cm^{-3}$) were chosen. As R/C increased from 50 to 1000, the major structural change was an increase in the size of the primary particles, from about 5–10 to 25–30 nm. Generally speaking, capillary forces are more pronounced as the size of the particles – and hence the pores – is reduced, that is, for low R/C; and the mechanical stability of the RF gels increased with their density.

All *aerogels* stayed monolithic, but some showed volumetric shrinkage, which was attributed to residual water and ethanol after the washing steps and can reach up to 40% for high R/C and high dilution ratio. By variation of the synthesis conditions, a wide range of apparent densities (as low as 0.19 g cm^{-3}) and pore sizes can be covered.

Cryogels could only be obtained as small pieces; according to the authors, this might be due to the thermal shock and solvent expansion during freezing (Job *et al.*, 2005). Two distinct behaviors could be observed: if the solid density of the wet gels was low, ice crystals may grow inside the gel, reducing the size of the meso- and macro-pores and creating megalopores larger than 10 μm. As discussed previously (see Fig. 5.21), this phenomenon is not related to the density change during freezing and not specific for water. (Note that classical macropores have sizes 50 nm $< d_p <$ 1 μm.) For wet gels with high solid density, the solid structure was either preserved, or the gel shrank considerably (by 56% in volume) if the pore size was smaller than 40 nm. This was probably caused by melting of the confined solvent since sample temperature was not controlled but increased during the process. Both aerogels and cryogels are very fragile if their porosity is high (>80%), and mechanically resistant if they are denser.

Vacuum-dried *xerogels* underwent more shrinkage than gels dried by the other methods; volumetric shrinkage was more pronounced for smaller particle size and lower initial solid density and reached up to 87%. The final density depended only on R/C, which determined the particle size, and increased from 0.52 to 1.1 g cm^{-3}, as this ratio decreased from 1000 to 50. In fact, the gels are compressed until the capillary force (set by the size of particles or pores) is counterbalanced by the mechanical strength of the network. The xerogels were monolithic for large pore size (at high R/C), whereas for small pore size (at low R/C) they could show cracks or, for low initial density, broke into pieces; they were not friable or fragile, and could be handled without damage. Due to shrinkage, samples with high porosity and small pores (<50 nm) could not be produced by vacuum drying.

5.5.4
Convective Drying

5.5.4.1 Preliminary Remarks

This section summarizes research work with air drying at ambient or elevated temperature and ambient pressure. Although the temperature, moisture and velocity of the air flow are often not well defined, all these efforts will be denoted by convective drying. Such methods are cheaper and safer than all previously discussed, and they are suitable for a continuous production process. The overview first puts focus on silica gels, then on RF gels, accounting for the historical development.

If one wants to produce aerogel-like silica without the use of supercritical drying, one should recall the influences of material parameters and drying conditions on damage by irreversible shrinkage and cracks (see Section 5.4.1). For a given material, we have seen that cracks can, in principle, be omitted by choosing a low enough drying rate, and shrinkage can be influenced by the properties of the pore liquid and its interaction with the solid. The choice of a *low-surface tension pore liquid* is favorable and can, in certain cases, prevent shrinkage. However, it should be noted that, for

practical solvents, the surface tension range is limited to about 0.015–0.072 N m^{-1}. To some extent, a higher temperature during drying can also reduce the surface tension and shrinkage (Smith *et al.*, 1995b); in order to set the temperature of the wet gel to a value different to wet bulb conditions the drying rate is limited by control of mass transfer in the oven. Concerning the *contact angle* with the solid, one must consider that most pore liquids completely wet the gel network; for respective experimental proof on silica gels see Smith *et al.* (1995b). Surface modification can, however, have another beneficial effect as we will see.

5.5.4.2 **Preventing Shrinkage and Cracks by Aging (Silica Gels)**

The other route to preventing shrinkage and cracks is by increasing pore size – at the expense of surface area – or by increasing *gel stiffness and strength*. One possibility to strengthen the gel is by aging in the mother liquor. Then, distinct branches of the network are cross-linked, the solid surface is smoothed and necks between primary particles grow by dissolution and re-precipitation of silica. Indeed, the mechanical properties of the gel are improved. Since the strengthening effect is not enough, Einarsrud (1998) performed washing of the wet silica gel (from TEOS via a base-catalyzed route) with a TEOS/ethanol solution (70 vol%) and aging at elevated temperatures (70 °C). From the *monomer solution*, silica can be more easily added at desired places of the gel network: first filling the necks, then the smallest pores, and finally increasing the thickness of the gel filaments. As a result, the solid density increases and its specific surface decreases. The aged gels (cylinders of ø 8.6 mm) were washed with ethanol, characterized by a beam bending experiment (Scherer, 1992b) and

- washed with liquid CO_2 and supercritically dried;
- washed with n-hexane for its low surface tension (0.018 N m^{-1}) and dried at ambient pressure by raising the temperature from 70 to 180 °C within 4 d.

The dry gels were characterized by helium pycnometry and nitrogen sorption. Knowing that convective drying can yield monolithic gels if the process is slow enough, the focus is here on shrinkage, and the density of the xerogels is the quality criterion. Figure 5.28 shows how this property depends on aging time and drying method. In fact, the solid density of the wet gel is the parameter that determines how the gel behaves during drying. Without aging, the wet gels have low density and undergo substantial shrinkage. Aged wet gels have a higher initial density, but show only little shrinkage so that their final density can be much lower. For aging times >1 d, there is only a little shrinkage and the best xerogels are obtained. There is also some shrinkage during supercritical drying that can be reduced by aging. For aged silica gels of density around 0.21 g cm^{-3}, convective drying can produce gels of the same quality as supercritical drying – without shrinkage. With a *skeletal density* of $\varrho_s \approx 2.15$ g cm^{-3} (Hæreid *et al.*, 1995), this corresponds to a porosity of $\psi \approx 90\%$. By the effects of aging, the shear modulus ($\sim$ bulk modulus) of wet gels increases by one order of magnitude (to values > 10 MPa), and the surface area of the corresponding xerogels decreases from 1000 to 700 m^2 g^{-1}.

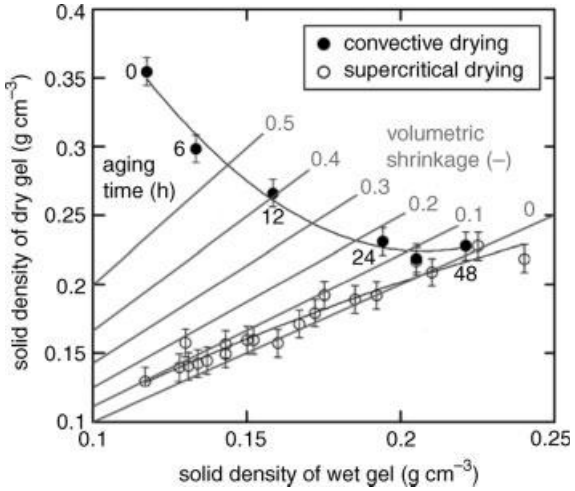

Fig. 5.28 Drying of silica gels aged in monomer solution; aging times are indicated for xerogels; gray lines indicate levels of volumetric shrinkage (adapted from Einarsrud (1998)).

The shrinkage of aged gels can also be understood by a model (Scherer *et al.*, 1996) that predicts the solid density of the gel after convective drying, using wet gel data (permeability and bulk modulus) and accounting for the increase in bulk modulus during drying.

It should be mentioned that there is no obvious alternative to the aging step: on the one hand, a simple increase in silica concentration in the starter solution only increases the gel density, without the corresponding increase in stiffness; on the other hand, quite stiff gels can be obtained under acidic synthesis conditions, but they have a smaller pore radius so that capillary forces still cause damage (Einarsrud, 1998).

A similar approach has been followed by Leventis *et al.* (2005) who studied *polymer crosslinking* of silica gels. The hydrogel (from TMOS via a base-catalyzed route) is first aged in mother liquor, then washed with ethanol, acetone and finally an acetone solution of hexamethylene diisocyanate O=C=N–$(CH_2)_6$–N=C=O; during subsequent curing, a conformal polymer coating forms on the gel network (see Fig. 5.29). If such a gel is dried in a 40 °C oven at ambient pressure after substituting the pore liquid for pentane, no shrinkage occurs because of the dimensional stabilization by crosslinking. Moreover, the xerogel shows no difference in appearance and structural parameters to supercritically dried gels. The xerogels (ø 10 mm, length 40 mm) have a relatively low BET surface area of 160 $m^2 g^{-1}$ and a relatively high density of 0.56 g cm^{-3}; indeed, crosslinked gels with lower densities were not stable during drying. However, their mechanical strength is increased by two orders of magnitude, and they are less hydrophilic in comparison to the underlying plain silica gel (Leventis *et al.*, 2005).

Besides providing a method to produce future lightweight materials, the study is interesting because it addresses the role of surface tension in drying shrinkage

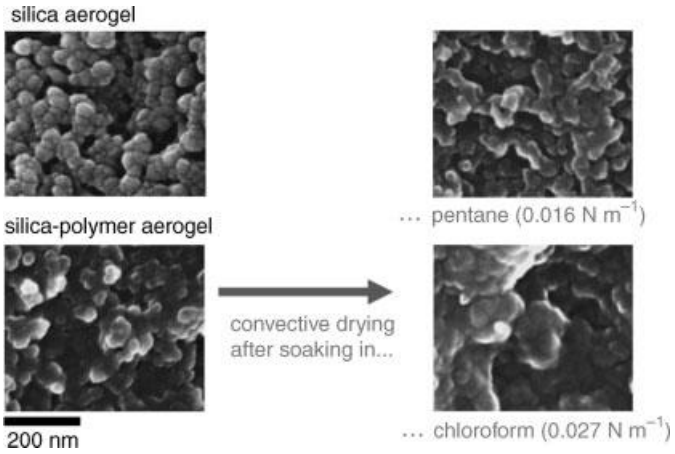

Fig. 5.29 Modification of silica aerogel by polymer-crosslinking and effect of capillary forces during convective drying (rearranged SEM images from Leventis *et al.* (2005)).

or rather collapse of the pore structure. To this purpose, crosslinked aerogels have been soaked in liquids with different surface tensions and dried convectively. As shown in Fig. 5.29, drying with pentane preserves the structure, whereas the pores collapse for liquids with higher surface tension, such as chloroform. The average pore radius (measured by nitrogen sorption) decreases from 9 nm to below 2 nm as the surface tension of the pore liquid increases from 0.016 to 0.027 N m^{-1}.

Strengthening of the gel network for successful convective drying has also been investigated for other classes of gels. Gan *et al.* (2005) produced highly porous *alumina* monoliths. An aluminum nitrate/ethanol solution was gelled with propylene oxide as gelation agent and formamide as the drying control chemical additive (DCCA). After aging in mother liquor, the gels were washed and aged in ethanol, TEOS/ethanol and again ethanol, to strengthen them by *silica crosslinking*, before drying at ambient pressure with a slow (10 K h^{-1}) temperature rise to 70 °C. Different molar ratios of gelation agent and DCCA have been selected to produce low-density silica-reinforced alumina gels. An increasing amount of formamide leads to smaller pores (pore size distributions by nitrogen sorption) and to more shrinkage; the role of DCCA during the sol–gel process is not clear, but the xerogel density passes through a minimum as its concentration is increased (see Fig. 5.30). For the optimal composition of the starter solution, a density of 0.26 g cm^{-3} (i.e., porosity >90%) was reached with particle sizes from 10–30 nm (see Fig. 5.30) and BET surface area around 450 m^2 g^{-1}. Other DCCA substances did not yield as low densities, and without any DCCA, the xerogel density was 0.4 g cm^{-3}.

5.5.4.3 Making Shrinkage Reversible by Surface Modification (Silica Gels)

Instead of preventing shrinkage, one may also try to make it reversible. To this aim, Smith *et al.* (1995b) modified the surface of the silica matrix before drying. The underlying idea is as follows: in unmodified silica gels, when pore walls get into close

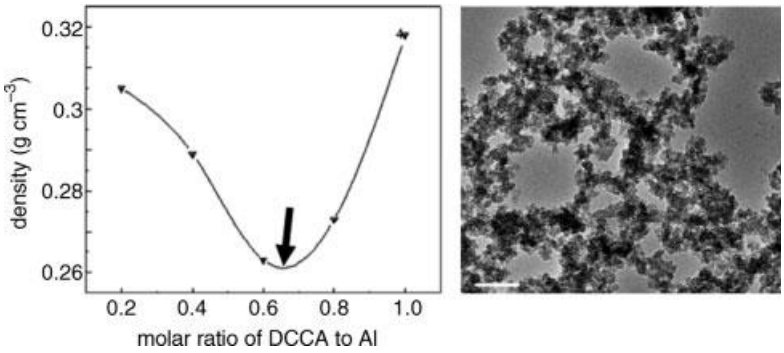

Fig. 5.30 Optimal ratio of DCCA for producing low-density alumina gel and TEM image (adapted from Gan *et al.* (2005)).

proximity during drying shrinkage, condensation reactions occur between neighboring hydroxy groups and make the shrinkage permanent. In order to prevent this crosslinking, the surface is methylated in a reaction with trimethylchlorosilane (TMCS):

$$\equiv \text{Si-OH} + \text{ClSi}(\text{CH}_3)_3 \rightarrow \equiv \text{Si-O-Si}(\text{CH}_3)_3 + \text{HCl} \tag{5.28}$$

(Such a substitution is also called silylation.) Then, bond formation in the compressed state is prevented and *springback* is possible when the capillary forces disappear at the end of the drying. In Fig. 5.31, the drying behavior of modified and unmodified gels is shown: both shrink to around 27% of their original volume before springback is observed to merely 30% for the unmodified gel and 97% for the modified one. Drying was performed at 35 °C for 2 d, after exchanging the pore liquid for n-heptane. A related study (Smith *et al.*, 1995a) showed that the density of the dry gels did not significantly vary when drying times of a cylinder with ø 10 mm were

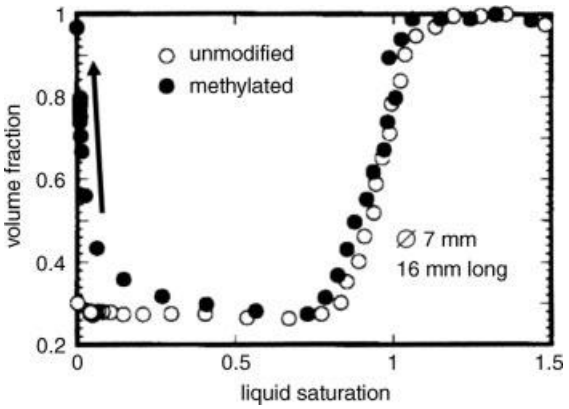

Fig. 5.31 Volume of silica gel during convective drying; springback occurs at the very end and its magnitude depends on the surface chemistry (from Smith *et al.* 1995b).

reduced from two days to several minutes. However, the dried gels broke into fragments of decreasing size (from 8 mm to < 3 mm) when the drying rate was increased, thereby proving that the stresses and damage by cracks depend on the drying rate.

More recent work investigates the role of surface modification with TMCS for small silica gel spheres (ø 3 mm) for springback and vapor diffusion during the second drying period (Bisson *et al.*, 2004). Drying took 2 h at 25 °C under controlled nitrogen flow. The modification step needs to be long enough (2 d) for complete volume recovery. Then, the dry gel density is almost as low as that obtained by supercritical drying (0.15 g cm^{-3} instead of 0.13 g cm^{-3}); the slight increase is due to mass uptake by the chemical reaction. The shrinkage before springback is also reduced if the surface is (more completely) modified; the authors argue that lower capillary forces must be the reason, but that the explanation cannot be given in terms of surface tension and contact angle. Instead, they showed by experiment that the wetting energy for the pore liquid (isopropanol) is significantly reduced by surface modification, and they argue that this sets a limit for how much (capillary) force can be transmitted from the pore liquid to the solid. The authors also highlight the low effective diffusivity of vapor that is three orders of magnitude lower than expected from the Knudsen diffusivity. Transport seems to be controlled by adsorption–desorption effects. Finally, surface modification also makes the dry gel less hydrophilic (Bisson *et al.*, 2004).

With the purpose of producing *hydrophobic* silica xerogel monoliths of high porosity, other *silylation agents* have been systematically explored by Rao *et al.* (2007). During drying of the modified gels with hexane (temperature protocol: 50 °C for 6 h, 120 °C for 12 h, 200 °C for 6 h), their volume change was recorded. The extent of shrinkage during drying is similar for all investigated agents, but volume recovery during springback is better if the silylation agent contains a higher number of alkyl groups; and hexamethyldisilazane $(H_3C)_6Si_2NH$ is even more suitable than TMCS, yielding a density of 0.06 g cm^{-3} (instead of 0.105 g cm^{-3}) and a porosity of 96.9% (instead of 94.6%), and having better transmission of light (65% instead of only 30%). The excellent hydrophobicity of the modified gels has been confirmed by contact angle measurement and long-term adsorption test in a water-saturated atmosphere, and their thermal stability up to 325 °C has also been proven.

In recent efforts towards a *cheaper production* process for highly porous silica gels, costly *raw materials* such as TEOS have been replaced by cheap water glass; then, sodium is substituted in an ion exchange (Schwertfeger *et al.*, 1998; Hwang *et al.*, 2007).

Furthermore, time-consuming and costly *solvent exchanges* used for surface modification with TMCS can be limited. In one approach (Schwertfeger *et al.*, 1998), silica hydrogel is put in hexamethyldisiloxane (HMDSO) and TMCS is added; then TMCS reacts with the pore water to give HMDSO and HCl. HMDSO is not miscible in water and forms a layer on the pore walls expelling the aqueous HCl. So, besides silylation with TMCS, the solvent is exchanged automatically, and the by-products are separated outside the gel. Durably hydrophobic xerogels with porosities $> 85\%$ have been produced in this way (Schwertfeger *et al.*, 1998).

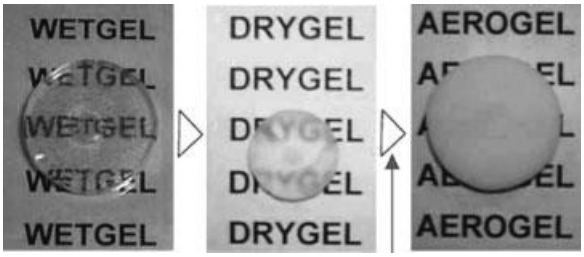

Fig. 5.32 Springback during convective drying of surface modified silica gel (from Hwang *et al.* (2007)). Here, "drygel" indicates the point when pores start to dry out; "aerogel" is the highly-porous xerogel.

In another approach (Hwang *et al.*, 2007), one solvent exchange with isopropanol/TMCS/n-hexane solutions was performed on the hydrogel with similar reactions and a phase separation as above: the surface is modified and pore water is replaced by low surface tension hexane. In this way, large monoliths (discs of ø 22 mm, 7 mm thick) have been obtained by controlled evaporation under hexane atmosphere at room temperature for 3 d. If the silica content in the starter solution (i.e., before gelation) was too low, the gel collapsed during drying and resulted in a powder; if it was too high, many cracks were observed. In the safe range (4 to 8 wt%), the performance depended on the amount of TMCS in the exchange solution: too little led to irreversible shrinkage, too much produced fracture during springback. Only the right amount (with molar ratio TMCS/pore water of 0.3 to 0.4) resulted in good springback (94% volume recovery) and crack-free xerogels with porosities around 93% (see Fig. 5.32) and surface areas around 675 $m^2 g^{-1}$.

Instead of surface modification, one may also directly synthesize *organic–-inorganic hybrid gels* to obtain springback behavior during drying, and elastic deformability of the dry gel: for example, Kanamori *et al.* (2008) produced gels with high porosity (> 80%) from methyltrimethoxysilane in a two-step process with urea as base-releasing agent and a surfactant to prevent phase separation. For certain synthesis parameters, supercritical drying can be substituted for convective drying without change of pore structure (confirmed by SEM images). During drying, the hybrid gel networks display reversible volumetric shrinkage of more than 60%; additionally, uniaxial compression of the dry gel up to a linear strain of 80% is reversible. The authors explain this extraordinary behavior by low crosslinking density keeping the gel flexible, low density of silanol groups on the network surface that could make shrinkage irreversible and repulsive forces between methyl groups.

5.5.4.4 RF Gels – From First Results to a Systematic Investigation

Encouraged by the results obtained with vacuum drying (see Section 5.4.3), Léonard and coworkers (2005a, b) explored the possibility of convective drying for RF hydrogels. Using wet gels (ø 22 mm, 13 mm high) prepared with identical synthesis conditions as before, convective drying was directly compared to vacuum drying. The gels were dried for 4–5 h with air of ambient humidity, heated to 70 °C and flowing at

2 m s^{-1}; all xerogels stayed monolithic despite the immense reduction in drying time (by a factor of 40). An increase in pH from 6 to 7 leads to an increase in microporosity and in BET surface area from 117 to 355 $m^2 g^{-1}$ and an increase in solid density in the RF xerogels. Vacuum drying yields higher surface area (approximately 500 $m^2 g^{-1}$ for the whole pH range), but always produces more shrinkage than convective drying, suggesting that the lower evaporation rates might be the reason (see also Mayor and Sereno (2004)).

For pH 6, convective drying produced xerogels with the highest porosity (77%) and no shrinkage (initial and final solid density were both 0.35 g cm^{-3}). This is explained by two effects: at lower pH, the pore size is large and the gel elastic, in contrast to the viscoelastic behavior and small pore size at higher pH which both favor shrinkage under capillary compression.

After pyrolysis, these xerogels are slightly more porous (up to 82% for pH 6), but have slightly increased density due to carbonization (the lowest value being 0.39 g cm^{-3} for pH 6) – an effect that is also reported for vacuum-dried gels. Additionally, the convectively dried gels show an increase in BET surface area and microporosity for all investigated pH (up to 628 $m^2 g^{-1}$ and 0.27 $cm^3 g^{-1}$, respectively, for pH 6). In contrast, open porosity and BET surface area could *not* be detected for pyrolyzed vacuum-dried gels at pH 6.5 and 7, probably because less condensation reactions (in lack of H^+) lead to a gel structure that is weak enough to collapse during the chemical restructuring of pyrolysis.

After these promising first results, a *systematic investigation* of convective drying was started, with a variation in drying air temperature and velocity to study their influence on the drying behavior of RF gels with different R/C ratio (Job *et al.*, 2006b). During drying, the sample is continuously weighed to deduce the drying rate. Additionally, the sample is characterized by X-ray microtomography (with a spatial resolution of 41 μm) at regular intervals to track changes in sample volume and surface, and also the evolution of cracks; care is taken that the intervals for characterization are short enough to not disturb the drying process.

Several RF hydrogels (ø 28 mm, 10 mm high), with different R/C ratios, but all having the same initial solid density of 0.35 g cm^{-3}, were gelled and aged at 70 °C for 24 h. Then, they were convectively dried in a laboratory drying tunnel with ambient air ($Y \approx 0.007$); different settings of temperature and velocity were chosen. Drying rate curves (evaporation flux versus moisture content) were reported and the correlation between drying conditions and drying kinetics was found to obey classical theory. The dry gels were characterized by nitrogen sorption and mercury porosimetry to obtain BET surface areas, approximate pore sizes, micropore volumes (pore radii <1 nm) and total pore volumes. Pore size distributions have not been derived from mercury porosimetry curves since all the pores seem to be compressed simultaneously (instead of a hierarchical collapse) (Job *et al.*, 2006a); however, the cumulative volume of pores larger than 7.5 nm (i.e., those compressed or invaded at maximal pressure) can be obtained.

In Tab. 5.4, the most interesting results of the study are summarized, for a fixed air velocity. Higher air temperature reduces the drying time but may destroy the sample, if the drying rate is too high. All gels with R/C = 1000 stayed *monolithic*, but developed

Tab. 5.4 Convective drying of RF gels (ø 28 mm, 10 mm high): influence of R/C and drying temperature (air with ambient moisture and velocity 2 m s^{-1}) on the drying time and structural properties. (Gels with R/C = 1000 developed cracks, but stayed monolithic.).

R/C	T_{dry} (°C)	t_{dry} (h)	Final state	$\Delta V/V_0$ (%)	BET area ($m^2 g^{-1}$)	Micropore volume ($cm^3 g^{-1}$)	Pore size (nm)	Ψ (%)
1000	70	4.2	monolith (cracks)	13	153	0.08	>50	75
	115	2.2	monolith (cracks)	12				
	160	1.1	monolith (cracks)	13				
500	70	5.6	monolith	47	320	0.15	35–45	55
	92.5	4.2	monolith	50				
	115	1.8	fragments	—				
300	30	20.1	monolith	60	308	0.14	10–15	37
	50	17.8	fragments	—				
	70	6.9	fragments	—				
	115	2.8	fragments	—				

cracks during drying, which first opened and then closed due to stress reversal at the end of drying, as shown in Fig. 5.33. For R/C = 500, the gels showed no cracks for low enough drying rates, but otherwise broke into *pieces*; if R/C is further reduced to 300, drying conditions had to be softened to avoid such catastrophic cracks (as expected from the theory of Scherer). For identical drying conditions, the drying time decreases with increasing R/C, probably due to increasing pore size that facilitates vapor diffusion.

From height and cross-section measurements, *shrinkage* is found to be *isotropic*. (For gels synthesized with a wider range of R/C that were dried slowly, the shrinkage curves are shown in Fig. 5.34.) During the first drying period, the shrinkage is *ideal*, that is, the volume reduction is only due to evaporation and all the pores are filled. In

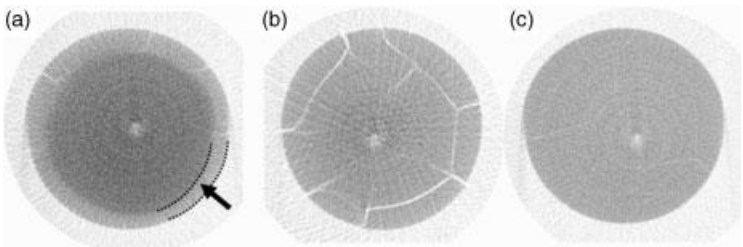

Fig. 5.33 X-ray microtomograph cross-sections of RF gel (R/C = 1000, ø 28 mm, 10 mm high, $X_0 = 2.03$) during convective drying at 115 °C for (a) $X = 0.47$, (b) $X = 0.2$ and (c) $X = 0.002$ (from Job *et al.* (2006a)).

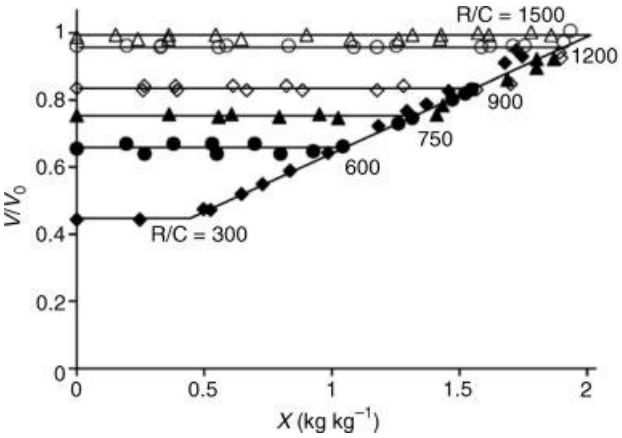

Fig. 5.34 Shrinkage of RF gels (Ø 22 mm, 13 mm high) during slow convective drying with ambient air (solid lines are guides to the eyes; adapted from Léonard *et al.* (2008)).

the second drying period, the gel volume remains constant and the pores dry out. With increasing R/C, that is, increasing pore size and stronger gel structure, the shrinkage period becomes shorter, or even negligible. Accordingly, the highest xerogel porosity was obtained for R/C = 1000, for which shrinkage is low and the drying front recedes quickly from the gel surface (as can be estimated from the different gray levels in Fig. 5.33a).

The extent of shrinkage is found to be independent of the drying conditions, for the investigated range of air temperatures and velocities. Similarly, the structural properties – BET surface area, micropore volume and average pore size – show no dependence on the drying conditions, but are determined by synthesis parameters. As in vacuum drying, RF xerogels with high porosity and small pores (<50 nm) could not be produced. Pyrolysis was not performed in this study, but is expected to drastically increase the BET surface area and, for high R/C, yield highly porous carbon gels.

It must be noted that the *shape and size* of the gel sample will also affect its tendency to crack. As seen above, constraints on the drying conditions are especially important

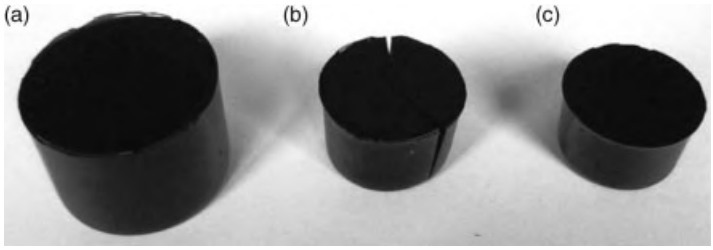

Fig. 5.35 RF gel with R/C = 300 (a) in its initial state (ø 46 mm, 28 mm high), (b) after partial drying at 50 °C and φ = 50% (cracking after 16 min) and (c) after complete drying at 40 °C and φ = 60% (ø 33 mm, 20 mm high).

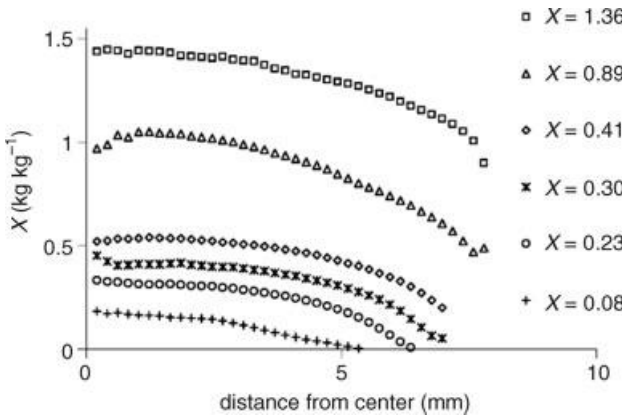

Fig. 5.36 Moisture profiles for different average moisture contents in a drying RF gel cylinder with R/C = 500 (adapted from Escalona *et al.*, 2008).

for low R/C ratios. If cracking is to be avoided for gels with R/C = 300, large samples (ø 46 mm, 28 mm high) need to be dried under soft conditions ($T = 40\,^{\circ}C$, $\varphi = 60\%$), whereas smaller samples (ø 23 mm, 12 mm high) can be dried under more severe conditions ($T = 70\,^{\circ}C$, $\varphi = 15\%$) (Léonard *et al.*, 2007). The shrinkage and cracking behavior of the larger sample is shown in Fig. 5.35.

Internal moisture transport during convective drying of the gel may be investigated with the help of experimental *moisture profiles* obtained from X-ray microtomography (Escalona *et al.*, 2008). As explained in Section 5.3.3, the different gray levels essentially reflect the average local densities, and their translation into moisture profiles requires calibration. Depending on the shrinkage behavior, the relation between the measured density and pore saturation may not be unique. Figure 5.36 shows the moisture profiles in a drying gel with initial moisture content $2\,kg\,kg^{-1}$. The gel does not shrink too much, so that a unique relation can be established for moisture contents up to $1.5\,kg\,kg^{-1}$. Such profiles can then be compared to simulation results (Escalona *et al.*, 2008) and may help to set up cracking criteria.

5.5.4.5 Aging of RF Gels

Complementary work (Job *et al.*, 2006c) aimed at optimizing *synthesis conditions*, especially in terms of aging time (up to 3 d) and temperature (50 to 90 °C). Aging is found to be crucial for completion of the condensation reactions and the corresponding strengthening of the gels: without aging, the samples broke into pieces during drying. Aging can be accelerated by increasing the temperature; and it seems to be completed after 2 d at 70 °C and after 1 d at 90 °C since longer times do not significantly change the pore structure. At 50 °C, the aging process seems to require more than 3 d, consequently, xerogels have low BET surface area and low pore volume. But aging temperature also has a direct influence on pore structure: a high value (90 °C) gives high surface area and pore volume, but may lead to undesired bubble formation in the gel. Consequently, aging for 2 d at 70 °C may be recommended.

In the same work, gels with R/C as high as 2000 (pore size around 500 nm) were also dried (at 70 °C); for them, a long period of constant absolute drying rate (in $kg\,s^{-1}$) is observed, in contrast to gels with R/C = 1000 (pore size around 50–80 nm). For both gels, shrinkage is negligible so that a first drying period can only be caused by capillary flow of pore liquid to the gel surface, and this is limited by friction in the smaller pores of the gel with R/C = 1000.

Independent work of Reichenauer *et al.* investigated the influence of R/C ratio (1000 to 3000), solvent exchange (acetone, isopropanol) and aging parameters on *linear shrinkage* of RF gels (Wiener *et al.*, 2004; Reichenauer *et al.*, 2007). For drying of RF hydrogels (R/C = 1500), significant linear shrinkage of around 15% is reported; it can be reduced to around 6% by solvent exchange (with acetone) and longer aging with progressive temperature increase (Wiener *et al.*, 2004). Nevertheless, these values are rather high in comparison to those discussed above, possible reasons being a slightly higher dilution ratio and different aging protocols (including a high temperature of 90 °C). Measurement of the length change during slow drying of solvent-exchanged gels showed that shrinkage may be partially reversible; such springback is almost suppressed for a solvent exchange with deionized water and quite pronounced for acetone and isopropanol (Reichenauer *et al.*, 2007).

The effect of aging was studied by Wu and Fu (2008) on RF gels synthesized with a microemulsion templating technique. Cetrimonium bromide is used as a surfactant (rather than catalyst) in the aqueous RF solution; after gelation and aging in mother liquor, the gels were slowly dried, first at room temperature (2 d), then under an infrared lamp (1 d) and finally in an oven at 100 °C (3 h). Subsequently, the RF xerogels were carbonized at 900 °C. By aging, the gel is strengthened so that drying shrinkage can be significantly reduced. The largest effect is observed during the first 12 h of aging: the compressive modulus increases from 39 to 176 MPa, and RF xerogel density decreases from 1.3 to 0.49 $g\,cm^{-3}$ for a resorcinol/surfactant (R/S) molar ratio of 200. By variation of R/S from 50 to 200 (with 5 d of aging), the pore size can be increased from 14 to around 40 nm without significant effect on the gel strength, with the consequence that drying shrinkage can be drastically reduced: xerogel density is decreased from 0.72 to 0.45 $g\,cm^{-3}$. The lowest density achieved for both RF and carbon xerogels in this work was 0.43 $g\,cm^{-3}$.

5.5.4.6 **Concluding Remarks**

To summarize the investigations on RF gels, one may say that the process parameters of convective drying may be optimized after the synthesis conditions have been set. The drying time can be reduced by increasing the air temperature and/or velocity and by decreasing the air humidity; however, the respective ranges are limited if monolithic xerogels are the goal, especially when the pores are small. The pore structure of carbon gels obtained by pyrolysis depends strongly on that of the RF dry gels. Although supercritical drying leads to the widest pore texture range (with difficulties to fix pore volume and pore diameter independently in the case of small pores, see Job *et al.* (2005)), vacuum or convective drying are sufficient in many cases, especially if dense, mechanically resistant carbons are needed, or if the only selection

criterion is the pore size. Any pore size can be obtained by evaporative drying, but it is strongly correlated to the pore volume: for the time being, it remains impossible to produce carbon xerogels with both small pores and high pore volumes. If such properties are desired, supercritical drying is still the method to choose.

5.5.5 Microwave Drying

Finally, preliminary studies on the use of microwave drying to produce RF and carbon xerogels will be reported. Gels with low molar ratio have been investigated by Tamon and coworkers (Yamamoto *et al.*, 2001b; Tamon *et al.*, 2003). Of special interest is the direct comparison of microwave drying with freeze-drying (freezing at $-30\,^{\circ}C$ for 6 h, drying at $-10\,^{\circ}C$ for 24 h) and convective drying (in a $50\,^{\circ}C$ oven for 48 h) for RF gels (ø 4 mm, 40 mm long) synthesized with $R/C = 200$ and $R/W = 0.375\,g\,cm^{-3}$ (Yamamoto *et al.*, 2001b); before drying, the solvent in all the gels was exchanged for *tert*-butanol. The most evident effect is the drastic drying time reduction for microwave drying – from more than 20 h for the alternative drying methods to only 10 min. However, the structural properties, as documented in Tab. 5.5, are also affected: in general, one may say that microwave drying yields gels of significantly better quality than hot air drying, but not as good as freeze-drying. In comparison to normal xerogels, the major improvement is that – during pyrolysis – mesopore volume is preserved and BET surface area is increased. Variation of R/W resulted in no significant changes in the carbon gel properties.

More extensive work (Tamon *et al.*, 2003) on RF gels with $R/C = 400$ showed that microwave drying can produce carbon gels with a quality comparable to carbon cryogels. For $C/W < 20\,mol\,m^{-3}$, large mesopore volumes and BET surface areas can be obtained. Microwave drying has also been combined with ultrasonic irradiation during sol–gel transition (Tonanon *et al.*, 2006); for $R/C = 200$ and several $C/W = 20$–$80\,mol\,m^{-3}$, the porous properties of the resulting microwave carbon gels were significantly improved.

Tab. 5.5 Influence of drying method on the structural properties of RF and carbon gels with $R/C = 200$, and $R/W = 0.375\,g\,cm^{-3}$ (from Yamamoto *et al.* (2001b)).

Drying method	After drying				After pyrolysis		
	Volumetric shrinkage (%)	Peak pore radius (nm)	Mesopore volume ($cm^3\,g^{-1}$)	BET surface area ($m^2\,g^{-1}$)	Peak pore radius (nm)	Mesopore volume ($cm^3\,g^{-1}$)	BET surface area ($m^2\,g^{-1}$)
freeze	54	5.5	1.45	554	5.5	0.94	662
hot air	78	1.8	0.31	255	1.6	0.06	121
microwave	75	2.4	0.56	422	1.8	0.48	549

Most recently, a wider range of R/C ratios (300–1000) was investigated for aqueous RF gels without solvent exchange (Zubizarreta *et al.*, 2008). Before microwave drying in a unimode cavity oven (1000 W for 30 min), the gels (ø 20 mm, 30 mm high) were aged at 85 °C for 3 d. Most of the gels stayed monolithic, and the structural properties of RF and carbon xerogels were similar to those previously reported for convective drying; in particular, the mesoporosity does not collapse during the drying step. This means that a rapid drying technique is available for the preparation of low-density carbon gels with high BET surface areas and different mesopore sizes.

5.6
Advanced Modeling of Convective Drying – Understanding Quality

The development of drying models is essential in order to optimize the drying process by speeding up the drying rate to reduce energy consumption and, at the same time, accounting for the quality of the dried material. Quality deterioration, mainly by cracking, depends on the stress route followed by the material during drying. Therefore, the models compare the predicted drying stresses to suitable cracking criteria. The reader will easily notice that the recent modeling approaches are inspired by the previously presented work of Scherer.

5.6.1
Macroscopic Models

5.6.1.1 General Remarks

Continuous models are easy to implement and, therefore, have been widely used to describe the drying of deformable porous media (e.g., see Chapters 3 and 4, Volume 1 of this series). In these models, gel properties are expressed in terms of average parameters (or parameter functions) such as the diffusion coefficient, thermal diffusivity and Young's modulus, and partial differential equations for mass, heat and momentum balances are solved by discretization ("top-down" approach).

As opposed to Scherer, recent models are non-isothermal and not restricted to essentially one-dimensional problems (such as an infinite plate, cylinder or sphere). Some of them consider the drying gel as a biphasic medium, that is, a solid matrix that remains saturated, so that the second drying period cannot be described. Others can also simulate shrinkage and stress after the liquid/gas phase boundary has receded into the gel, as already explored by Scherer (1987b) for a flat plate by assuming a constant evaporation rate until the gel is completely dry.

5.6.1.2 Diffusion Model

Léonard and Pourcel developed thermo-hygro-mechanical models for the drying of resorcinol-formaldehyde hydrogels and alumina gels, respectively (Léonard *et al.*, 2006; Escalona *et al.*, 2008; Pourcel *et al.*, 2007a). Their equations are based

on the work of Jomaa and Puiggali (1991). Each type of gel is assumed to be a shrinking medium, in which the liquid and solid phases are followed during the drying. Saturation of the sample, that is, ideal shrinkage, is assumed throughout the drying process. The equations are written in Eulerian coordinates and a matrix velocity $\mathbf{v}_s$ is introduced to take account of the mechanical coupling.

Léonard *et al.* (2006) modeled liquid transport in the (fully saturated) gel by a diffusion approach for the volume-averaged liquid density, $\bar{\varrho}_w = \psi\varrho_w$,

$$\frac{\partial\bar{\varrho}_w}{\partial t} = \nabla\cdot(D_{eff}\nabla\bar{\varrho}_w - \bar{\varrho}_w v_s) \tag{5.29}$$

where D_{eff} is the (constant) effective diffusion coefficient describing liquid flow; heat transfer is described by pure conduction

$$\varrho c_P\frac{\partial T}{\partial t} = \nabla\cdot(\lambda_{eff}\nabla T) \tag{5.30}$$

where ϱc_P and λ_{eff} are the effective volumetric heat capacity and the thermal conductivity, respectively. The drying gel is a cylinder (see Fig. 5.37) with flux boundary conditions on all surfaces: evaporation flux is computed from the mass transfer coefficient and the difference in air humidity in the bulk and at the gel surface (the latter is obtained from a sorption isotherm that relates moisture content $X = \bar{\varrho}_w/\bar{\varrho}_s$ to relative humidity); heat flux is the sum of enthalpy loss due to evaporation and heat transfer through the gas-side boundary layer.

The solid phase is considered to be in elastic mechanical equilibrium, which is reasonable if the characteristic time of relaxation is smaller than the characteristic time for moisture diffusion. Then, the divergence of the stress tensor must be zero; in cylindrical polar coordinates, this translates into the following equations for normal stresses, σ_r, σ_θ and σ_z, and shear stress, τ_{rz}:

$$\begin{aligned}\frac{\partial\sigma_r}{\partial r} + \frac{\sigma_r-\sigma_\theta}{r} + \frac{\partial\tau_{rz}}{\partial z} &= 0\\ \frac{\partial\sigma_z}{\partial z} + \frac{\partial\tau_{rz}}{\partial r} + \frac{\tau_{rz}}{r} &= 0\end{aligned} \tag{5.31}$$

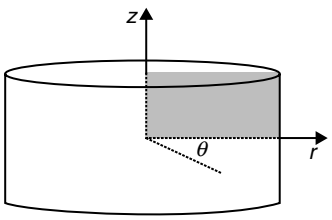

Fig. 5.37 Axisymmetric geometry for a drying gel cylinder.

The stresses depend linearly on the *difference* between total strains and shrinkage strains (because shrinkage itself does not contribute to stress),

$$\begin{bmatrix} \sigma_r \\ \sigma_\theta \\ \sigma_z \end{bmatrix} = \frac{E}{(1+\nu)(1-2\nu)} \begin{bmatrix} 1-\nu & \nu & \nu \\ \nu & 1-\nu & \nu \\ \nu & \nu & 1-\nu \end{bmatrix} \begin{bmatrix} \varepsilon_r^T - \varepsilon_r^S \\ \varepsilon_\theta^T - \varepsilon_\theta^S \\ \varepsilon_z^T - \varepsilon_z^S \end{bmatrix} \qquad (5.32)$$

$$\tau_{rz} = \frac{E}{1+\nu} \varepsilon_{rz}^T$$

where E is Young's modulus and ν Poisson's ratio. The total normal and shear strains depend on the radial and axial displacement, u_r and u_z, as

$$\varepsilon_r^T = \frac{\partial u_r}{\partial r}, \quad \varepsilon_\theta^T = \frac{u_r}{r}, \quad \varepsilon_z^T = \frac{\partial u_z}{\partial z}$$

$$\varepsilon_{rz}^T = \frac{\partial u_r}{\partial z} + \frac{\partial u_z}{\partial r} \qquad (5.33)$$

whereas shrinkage strain, for isotropic materials, is computed from the total sample volume as

$$\varepsilon_r^S = \varepsilon_\theta^S = \varepsilon_z^S = \sqrt[3]{\frac{V}{V_0}} - 1 \qquad (5.34)$$

(For ideal shrinkage, the sample volume only changes by loss of liquid.) The boundary condition ensures that no normal stress acts on the surfaces.

This model was applied to simulate the experimental situation of convective drying of *RF gels* described in Section 5.5.4.4 (Léonard *et al.*, 2006). To this purpose, Young's modulus was measured as a function of moisture content, using slowly dried gels with no moisture gradient. For compliant gels (R/C $\leq$ 500), for which the assumption of ideal shrinkage is valid over a wide range of moisture content (see Fig. 5.34), the simulated drying curves (Léonard *et al.*, 2006) and moisture profiles (Escalona *et al.*, 2008) were in good agreement with the experimental ones. As additional information, stresses in the drying gel became available. In accordance with the experimental results (see Tab. 5.4), more severe drying conditions (Léonard *et al.*, 2006) or larger sample size (Léonard *et al.*, 2007) increase the stresses in the gel that – above a certain level – lead to cracking. As an example, Fig. 5.38 shows maximal von Mises stresses that are relevant for damage to the material, as a function of drying temperature.

A slightly advanced model was applied to the drying of *alumina gels* which are precursors for ceramic catalyst supports (Pourcel *et al.*, 2007a, b). It is essential to avoid micro-cracks during the drying step because they could propagate during the subsequent calcination process and reduce the material strength that is required for the industrial application of the porous ceramic material. Pourcel *et al.* introduced the moisture dependence of the liquid diffusion coefficient and added convective contributions of liquid and solid to the heat transfer in Eq. 5.30. For parametrization of the hydro-thermo-mechanical model, sorption isotherm (with a hygroscopic

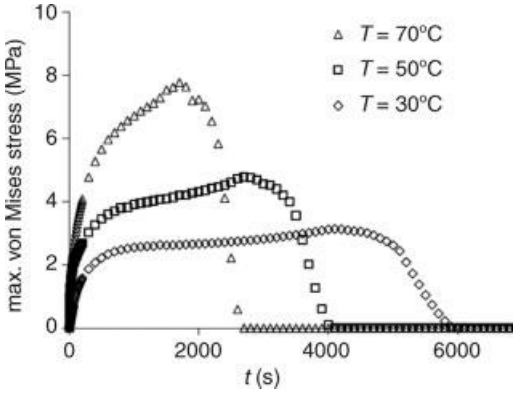

Fig. 5.38 Influence of air temperature in convective drying: maximal von Mises stress for a compliant RF gel.

region for $X < 0.65$), shrinkage behavior (ideal from the initial moisture content of 1.7 down to 0.3) and Young's modulus of the alumina gel were measured. As the essentially new model element, a crack initiation criterion is defined, to allow determination of the drying conditions leading to a crack-free material. For this purpose, tensile failure strength was measured as a function of moisture content by a Brazilian test. In this indirect test, a gel cylinder is put under radial compression so that tensile stress is induced in its center until it crushes. The tensile strength is found to increase exponentially with decreasing moisture content (see Fig. 5.42), just as Young's modulus, both being a consequence of increasing stiffness during (drying) shrinkage. The complete model is then able to predict the drying time when cracks, if any, are initiated by comparing simulated stress to failure stress.

To validate the model, an alumina gel rod ($20 \times 20 \times 80\,mm^3$) was dried convectively on an aluminum plate, sealing all surfaces except the top one (see Fig. 5.41a). Evolution of average moisture content, several local temperatures in the gel as well as moisture profiles (by gravimetric analysis of gel slices) were measured, all being in good agreement with the simulation results. Fig. 5.39 shows a comparison of experimental and simulated moisture profiles.

The occurrence of cracks has been experimentally investigated with the following major findings (documented in Fig. 5.40). For very slow drying rates, the gel dries without cracks. Above a *first critical* drying rate, cracks occur in the later drying stages (at times $> 10^5$ s), when the gel stops shrinking and its surface is no longer saturated with pore liquid; then macroscopic stress in combination with local differences in capillary forces results in cracks (as described in Section 5.4.1). In this case, the crack pattern is irregular. If the drying rate exceeds a *second critical* value, cracks already occur at the very beginning (at times <1000 s). Then, the cracks are due to severe moisture gradients and pronounced differential shrinkage. Such cracks show a rather regular pattern. For a gel rod with smaller dimensions ($10 \times 10 \times 80\,mm^3$), both critical values of drying rate are increased, because less stress develops in smaller samples.

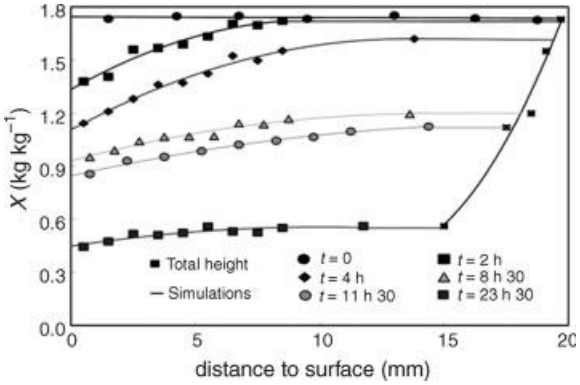

Fig. 5.39 Moisture profiles during drying (30 °C, φ = 60%, air at 2 m s^{-1}) of a shrinking alumina gel rod (20 × 20 × 80 mm^3) (taken from Pourcel *et al.* (2007b)).

From stress simulations (in Cartesian coordinates), normal and shear stresses in the gel rod are obtained (an example is shown in Fig. 5.41). Maximum stress develops at the drying surface as tensile stress (indicated by the arrow). These numerical results, together with the criterion for cracks, can reproduce the overall cracking behavior with the two critical times. Figure 5.42 shows that, sooner or later, depending on the drying rate, the surface tensile stress exceeds the tensile strength of the gel. The observed stress maximum is a result of the stress increase due to densification and the successive stress decrease due to the reduction in drying rate in the hygroscopic region. In this way, short crack initiation times are predicted quite

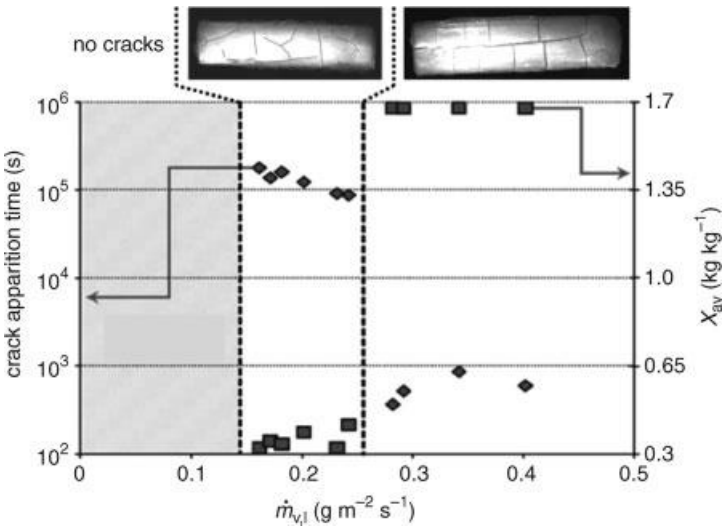

Fig. 5.40 Drying time and average moisture content at the moment of crack apparition in alumina gel (20 × 20 × 80 mm^3), as a function of evaporation rate in the first drying period (adapted from Pourcel *et al.* (2007a, 2007b)).

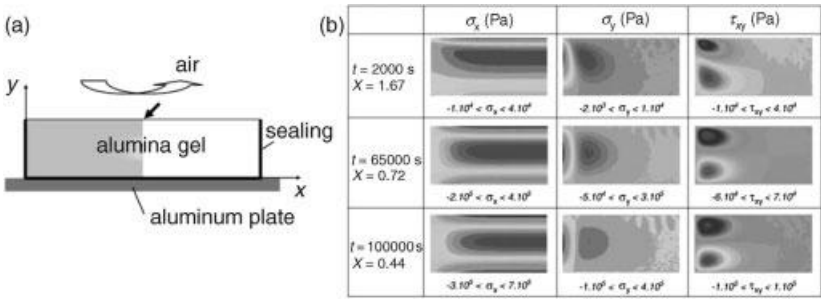

Fig. 5.41 (a) Experimental set-up and (b) simulated stress fields (for shaded sample area) in drying alumina gel rod ($20 \times 20 \times 80\,mm^3$) (30 °C, $\varphi = 70\%$, air at $2\,m\,s^{-1}$) (taken from Pourcel *et al.* (2007b)).

well, but the time of appearance of cracks at the transition to the second drying period is underestimated (cracking is predicted for too high surface moisture content).

The authors see the reason in the model assumption of elastic mechanical equilibrium. In reality, the alumina gel behaves as a viscoelastic material and stress is related to strain as

$$\sigma_x = \int_0^t R(X, t-\tau)\frac{\partial \varepsilon_x}{\partial t}\bigg|_\tau d\tau \tag{5.35}$$

The relaxation function $R(X,t)$ can be described by a generalized Maxwell model, as illustrated in Fig. 5.43 with three elasticity moduli R_i of different relaxation times τ_i

$$R(X,t) = R_0(X) + \sum_{i=1}^{3} R_i(X)\exp\left(-\frac{t}{\tau_i}\right) \tag{5.36}$$

In the simulations, the elastic behavior has been described by a Young's modulus $E = R(X,0)$, thereby assuming that relaxation can be neglected. In fact, the longest,

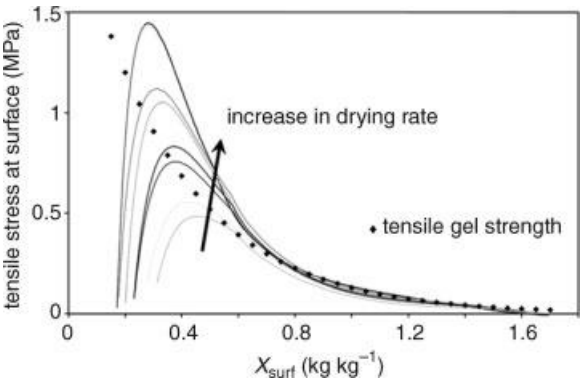

Fig. 5.42 Comparison between simulated tensile stress and gel strength at the gel surface during drying for different drying conditions (from Pourcel *et al.* (2007b)).

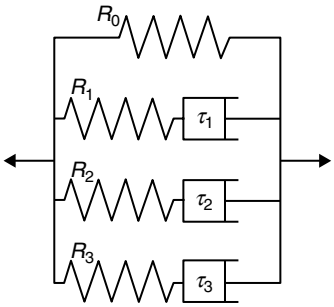

Fig. 5.43 Generalized Maxwell model for viscoelastic gels.

and therefore most important, relaxation time ($\tau_3 = 1000$ s) is small in comparison to the drying times of a large gel sample. This provides a macroscopic explanation for the discrepancy between simulated and experimental values for long cracking times, since viscoelastic stresses are sensitively delayed and higher at the end of drying than elastic ones (Bogdanis, 2001).

It should, however, be kept in mind that the model crack criterion contains no contribution from the drying-out of the gel surface – be it in terms of an averaged receding liquid/gas boundary or, at the microscale, as information about the emptying of individual pores. In fact, the simulation predicts cracks because, during stiffening of the gel, stresses increase more than the strength (see Fig. 5.42).

The extended (viscoelastic) model will be used on RF gels so that recent experimental efforts (Léonard *et al.*, 2007) aim to estimate the numerous necessary parameters. For R/C ratios from 300 to 1500, the elastic modules and relaxation times of Eq. 5.36 are determined as a function of moisture content in a compressive axial test. Additionally, the compression modulus is extracted from mercury porosimetry (Scherer *et al.*, 1995b) so that Poisson's ratio can also be estimated. For low R/C, gels are found to be stiffer and have more pronounced viscoelastic behavior. During drying, a given gel gets stiffer and the viscous contributions become less important. In this work, the difficulty in obtaining a clear separation of solid and liquid contributions to the mechanical properties of the gel also becomes obvious: hydrodynamic effects play an important role for the relaxation times which are attributed to the gel.

5.6.1.3 More Rigorous Modeling

The diffusion model is not very satisfactory from a physical point of view since liquid transport is known to be convective. Therefore, Jomaa *et al.* made an effort to develop a more fundamental description by volume averaging of the heat and mass balances in the deforming saturated gel (Cáceres *et al.*, 2007). For the evolution of the volume-average liquid density, or equivalently the local porosity $\psi = \bar{\varrho}_w/\varrho_w$, they obtained

$$\frac{\partial \bar{\varrho}_w}{\partial t} = \nabla \cdot \left(\frac{K}{\mu_w/\varrho_w} \nabla P_w - \bar{\varrho}_w \mathbf{v}_s \right) \tag{5.37}$$

which directly replaces Eq. 5.29 from the diffusion model. An additional balance equation is obtained for total mass by assuming ideal shrinkage

$$0 = \nabla \cdot \left(\frac{K}{\eta_w} \nabla P_w - \boldsymbol{v}_s \right) \tag{5.38}$$

(In the original versions of the two latter balance equations, the authors also account for the compressibility of the liquid, which is negligible from a physical point of view but helpful for numerical stabilization.) The energy balance contains contributions from heat conduction and liquid and solid convection. The usual flux boundary conditions are applied to the heat and mass transfer equations.

Again, mechanical equilibrium is assumed, that is, a divergence-free total stress tensor. The total stress tensor decomposes into solid network stress and liquid stress (with identity matrix **I**):

$$\sigma = \sigma_s - P_w \mathbf{I} \tag{5.39}$$

Network stress is then related to the *finite* strain tensor with an elastic material law, and normal stress is set to zero at the gel surface. This closes the mathematical problem for the four independent variables, ψ, P_w, $\mathbf{v}_s$ and T.

The previous drying experiment on a gel rod is used to assess the model. Moisture and temperature evolution are fairly well reproduced by the simulation; and maximal tensile stresses are obtained that are similar to those computed with the diffusion model. However, the numerical liquid pressure attains unrealistically low values, which is a result of the non-penetration assumption for gas. Here, the missing link of the macroscopic model to microstructural properties, that is, pore size, becomes obvious.

Altogether, this model formulation provides a complete and physically correct description of fluid transfer and seems to be suited for extension to the partially saturated gel of the second drying period. A major challenge remains the definition of an air-penetration criterion that initiates the second drying period.

5.6.2
Development of A Pore-Scale Model

In the macroscopic description of porous media, structural features are hidden in effective parameters, and phenomena that are characteristic of the micro-scale are obscured by rather crude, often semi-empirical, models. Of course, this general deficiency is also true for the macroscopic description of gel drying. However, the transition to the second drying period, and in particular the development of cracks at this moment, is a particular problem, where the necessity to account for pore-scale phenomena becomes even more evident. The purely macroscopic description needs criteria that not only depend on the microstructure itself, but also on how it behaves during drying.

When the liquid/gas phase boundary recedes into the gel, the spatial distribution of liquid and solid is crucial for the mechanical load on the gel by capillary forces and the ability of the gel network to support this load without damage. In order to

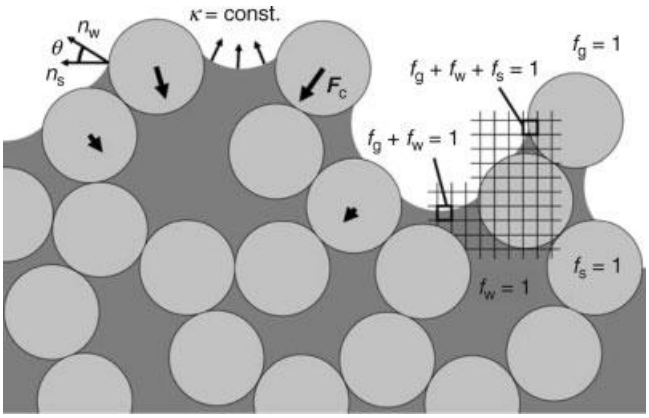

Fig. 5.44 Pore-scale representation of drying gel with conditions for capillary equilibrium, capillary forces on the gel network and the use of phase functions in discretization.

understand better what happens at this critical stage of drying, Kirsch *et al.* (2009) are currently developing a simulation tool that operates on the pore-level and will predict macroscopic behavior in a "bottom-up" approach.

In a first model version, the liquid distribution on the network of primary particles is assumed to be in capillary equilibrium. This allows interpretation of the fluid dynamics problem as a shape transformation problem. Connected liquid patches have uniform curvature κ of the liquid/gas phase boundary; additionally, at three-phase boundaries, the contact angle θ to the solid surface must be fulfilled (see Fig. 5.44).

The drying problem is solved in small time steps by removing some liquid at the local evaporation rates and subsequently relaxing the liquid with a volume-of-fluid approach as proposed by Stepanek *et al.* (1999). Space is discretized into voxels, and the distribution of solid, liquid and gas is described by the respective volume fractions in these voxels (f_s, f_w and f_g). From these phase functions, normal vectors can be computed, for example

$$\mathbf{n}_w = -\frac{\nabla f_w}{|\nabla f_w|} \tag{5.40}$$

Then, the above equilibrium conditions can be expressed as

$$\nabla\kappa = \nabla\left(\frac{1}{2}\nabla\cdot\mathbf{n}_w\right) = 0 \tag{5.41a}$$

$$\mathbf{n}_s\cdot\mathbf{n}_w = \cos\theta \tag{5.41b}$$

The discrete versions of these equations must be fulfilled in liquid–gas voxels (only first equation) and in three-phase voxels (both equations), as highlighted in Fig. 5.44. Volume conservation sets a constraint to the optimization problem. Figure 5.45 shows a result of pore liquid relaxation. Such simulated equilibrium liquid distributions will be validated by microtomography on model systems with larger particles.

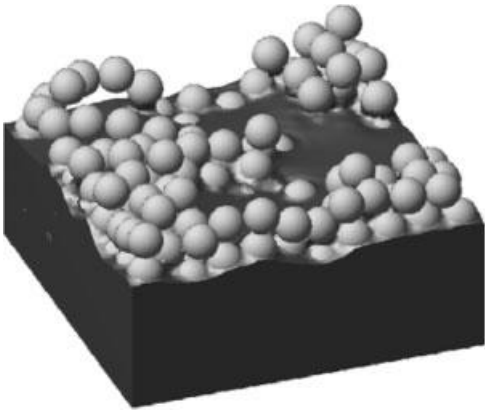

Fig. 5.45 Liquid distribution on an open-pore particle network after capillary relaxation from a plane phase boundary.

From the liquid phase distribution, the capillary forces $\mathbf{F}_c$ on the individual gel particles are accessible, with one contribution from the bulk liquid and a second from the three-phase contact line. By use of the discrete element method (DEM), capillary forces can be loaded on the primary particles, which are connected by bonds; as a result, micro-cracks – and also shrinkage – can be simulated (Kharaghani *et al.*, 2011). The cracking criterion is, hence, set by the strength of the necks interlinking the primary particles.

This pore-scale drying model is very close to physical reality, but will require geometrical information about the particle network that may be obtained from Monte-Carlo aggregation models (e.g., Rottereau *et al.* (2004)). The model additionally requires parametrization; due to the small dimensions, this will have to be done by calibration of the simulated macroscopic behavior by experiments on small gel samples.

The necessary link to the macroscopic stresses in the gel will be established by restricting the simulation to a surface region of the gel and by imposing an average pressure gradient that can be related to the drying rate by macroscopic permeability (again avoiding expensive fluid dynamics). The intention of this approach is not only to set limits to the drying rate, but to see which micro-scale arrangements of the primary particles and which liquid–solid systems are favorable for structure preservation during drying.

5.7 Summary

In the first part of this chapter, background knowledge has been provided regarding the unusual physical properties of gels, the synthesis of selected gels, and the specific behavior of gels during characterization and in the course of drying, with a focus on gel structure and its deterioration. In the second, main part of the chapter, recent research efforts in drying technology have been discussed for a choice of inorganic

and organic gels. Especially, several successful approaches to the production of dry gels with high porosity and high surface area by routes other than supercritical drying have been presented. Indeed, for a range of materials, freeze-drying and convective drying offer real alternatives to this expensive and dangerous process; and microwave drying may be an immerging technique. Attention has also been given to research aiming to avoid or reduce time-consuming and expensive washing steps prior to drying; and some efforts to use low-cost gel precursors have been included. Furthermore, X-ray microtomography has been presented as a modern technique to track structural changes during drying. Finally, we have reported on recent and emerging drying models, operating at the macro-level or at the pore scale. Their goal is to predict drying shrinkage and stresses and to set model-based criteria to avoid quality loss, mainly by cracks.

Future research is required if dry gels with extreme porosity (>90%) and pore size in the low-nanometer range, as required for insulation purposes, are to be produced by evaporative drying techniques. New multi-scale modeling is expected to shed more light on the mechanisms causing shrinkage and cracking. This will allow optimization of drying conditions, but might also give the chance to engineer gel structures that are suitable for convective drying.

Additional Notation Used in Chapter 5

A_s	specific surface area	$m^2\,kg^{-1}$
C_0	constant ($\approx 1/3$)	—
C_1	constant defined by Eq. 5.20	Pa
C_2	constant defined by Eq. 5.20	—
c	crack length	m
d_p	pore diameter	m
E	Young's modulus	Pa
F	force	N
F	uniaxial solid viscosity	Pa s
f	phase volume fraction	—
I_{cr}	critical stress intensity	$Pa\,m^{0.5}$
K	permeability	m^2
K_G	bulk solid viscosity	Pa s
K_p	bulk modulus	Pa
K_0	initial bulk modulus	Pa
m	exponent in Eq. 5.11	—
N	Poisson's ratio for viscous gel	—
$\mathbf{n}$	unit normal vector	—
R	aggregate radius	m
R	radius of gel cylinder	m
R_i	mechanical moduli in Fig. 5.43	Pa
r	primary particle radius	m
r_p	pore radius	m

Greek letters

α	thermal expansion coefficient	K^{-1}
$\dot{\varepsilon}$	strain rate	s^{-1}
θ	contact angle	rad
κ	mean curvature	m^{-1}
ν	Poisson's ratio	—
Π	quantity defined by Eq. 5.10	—
$\tilde{\sigma}$	solid network stress	Pa
τ	shear stress	Pa
τ	relaxation time	s
ψ	porosity (voidage)	—

Subscripts and superscripts

c	(ice) crystal
c	curvature
cr	critical
p	pore
S	shrinkage
T	total
x, y, z	in coordinate direction
0	initial

Abbreviations

BET	Brunauer, Emmett and Teller theory
C	catalyst
CT	computed tomography
DCCA	drying control chemical additive
DSC	differential scanning calorimetry
ESEM	environmental scanning electron microscopy
HMDSO	hexamethyldisiloxane
R	resorcinol
RF	resorcinol-formaldehyde
S	surfactant
SAXS	small angle X-ray scattering
SEM	scanning electron microscopy
TEM	transmission electron microscopy
TEOS	tetraethoxysilane
TMCS	trimethylchlorosilane
TMOS	tetramethoxysilane
W	water

References

Alaoui, A. H., Woignier, T., Pernot, F., Phalippou, J., Hihi, A., 2000. Stress intensity factor in silica alcogels and aerogels. *J. Non-Cryst. Solids* **265**: 29–35.

Alié, C., Benhaddou, A., Pirard, R., Lecloux, A. J., Pirard, J. P., 2000. Textural properties of low-density xerogels. *J. Non-Cryst. Solids* **270**: 77–90.

Alié, C., Pirard, R., Pirard, J.-P., 2001. Mercury porosimetry: applicability of the buckling-intrusion mechanism to low-density xerogels. *J. Non-Cryst. Solids* **292**: 138–149.

Al-Muhtaseb, S. A., Ritter, J. A., 2003. Preparation and properties of resorcinol-formaldehyde organic and carbon gels. *Adv. Mater.* **15**: 101–114.

Bellunato, T., Calvi, M., Matteuzzi, C., Musy, M., Perego, D. L., Storaci, B., 2007. Refractive index dispersion law of silica aerogel. *Eur. Phys. J. C* **52**: 759–764.

Berthon, S., Barbieri, O., Ehrburger-Dolle, F., Geissler, E., Achard, P., Bley, F., Hecht, A. M., Livet, F., Pajonk, G. M., Pinto, N., Rigacci, A., Rochas, C., 2001. DLS and SAXS investigations of organic gels and aerogels. *J. Non-Cryst. Solids* **285**: 154–161.

Bisson, A., Rigacci, A., Lecomte, D., Rodier, E., Achard, P., 2003. Drying of silica gels to obtain aerogels: phenomenology and basic techniques. *Drying Technol.* **21**: 593–628.

Bisson, A., Rodier, E., Rigacci, A., Lecomte, D., Achard, P., 2004. Study of evaporative drying of treated silica gels. *J. Non-Cryst. Solids* **350**: 230–237.

Blacher, S., Heinrichs, B., Sahouli, B., Pirard, R., Pirard, J.-P., 2000. Fractal characterization of wide pore range catalysts: application to Pd-Ag/SiO2 xerogels. *J. Colloid Interface Sci.* **226**: 123–130.

Bock, V., Emmerling, A., Saliger, R., Fricke, J., 1997. Structural investigation of resorcinol formaldehyde and carbon aerogels using SAXS and BET. *J. Porous Mater.* **4**: 287–294.

Bogdanis, E., 2001. *Modelling of heat and mass transport during drying of an elastic-viscoelastic medium and resolution by the finite element methods.* Diss. University Pau, France.

Boonamnuayvitaya, V., Tayamanon, C., Sae-ung, S., Tanthapanichakoon, W., 2006. Synthesis and characterization of porous media produced by a sol-gel method. *Chem. Eng. Sci.* **61**: 1686–1691.

Brinker, C. J., Scherer, G. W., 1990. *Sol-gel science.* Academic Press, Boston, USA.

Brun, M., Lallemand, A., Quinson, J.-F., Eyraud, C., 1977. A new method for the simultaneous determination of the size and the shape of pores: the thermoporometry. *Thermochim. Acta* **21**: 59–88.

Cáceres, G., Bruneau, D., Jomaa, W., 2007. Two-phase shrinking porous media drying: a modeling approach including liquid pressure gradient effects. *Drying Technol.* **25**: 1927–1934.

Daughton, D. R., MacDonald, J., Mulders, N., 2003. Acoustic properties of silica aerogels between 400 mK and 400 K. *J. Non-Cryst. Solids* **319**: 297–303.

Degn Egeberg, E., Engell, J., 1989. Freeze-drying of silica gels prepared from siliciumethoxid. *Rev. Phys. Appl.* **24**: C4–C23.

Dollimore, D., Heal, G. R., 1964. An improved method for the calculation of pore size distribution from adsorption data. *J. Appl. Chem.* **14**: 109–114.

Einarsrud, M.-A., 1998. Light gels by conventional drying. *J. Non-Cryst. Solids* **225**: 1–7.

Escalona, I., Jomaa, W., Olivera-Fuentes, C., Crine, M., Blacher, S., Léonard, A., 2008. Convective drying of gels: comparison between simulated and experimental moisture profiles obtained by X-ray microtomography. *Proceedings of 16th International Drying Symposium (IDS2008)*, Hyderabad, India, Vol. C, 1209–1215.

Farmer, J. C., Fix, D. V., Mack, G. V., Pekala, R. W., Poco, J. F., 1996. Capacitive deionization of NaCl and NaNO3 solutions with carbon aerogel electrodes. *J. Electrochem. Soc.* **143**: 159–169.

Farmer, J. C., Bahowick, S. M., Harrar, J. E., Fix, D. V., Martinelli, R. E., Vu, A. K., Caroll, K. L., 1997. Electrosorption of chromium ions on carbon aerogel electrodes as a means of remediating ground water. *Energ. Fuel* **11**: 337–347.

Fricke, J., 1986. Aerogele. *Phys. unserer Zeit* **17**(4): 101–106.

Gan, L., Xu, Z., Feng, Y., Chen, L., 2005. Synthesis of alumina aerogels by ambient drying method and control of their structures. *J. Porous Mater.* **12**: 317–321.

Geis, S., Müller, B., Fricke, J., 2000. Dielectric constants of SiO2 and RF aerogels measured by a response function method. *J. Porous Mater.* **7**: 423–433.

Goldstein, J. I., Newbury, D. E., Echlin, P., Joy, D. C., Lyman, C. E., Lifshin, E., Sawyer, L., Michael, J. R., 2003. *Scanning electron microscopy and X-ray microanalysis.* 3rd edn, Kluwer Academic/Plenum Publishers, New York, USA.

Hæreid, S., Dahle, M., Lima, S., Einarsrud, M.-A., 1995. Preparation and properties of monolithic silica aerogels from TEOS-based alcogels aged in silane solutions. *J. Non-Cryst. Solids* **186**: 96–103.

Heinrich, T., Klett, U., Fricke, J., 1995. Aerogels—Nanoporous materials, Part I: Sol-gel process and drying of gels. *J. Porous Mater.* **1**: 7–17.

Hrubesh, L. W., Poco, J. F., 1995. Thin aerogel films for optical, thermal, acoustic and electronic applications. *J. Non-Cryst. Solids* **188**: 46–53.

Hrubesh, L. W., 1998. Aerogel applications. *J. Non-Cryst. Solids* **225**: 335–342.

Hüsing, N., Schubert, U., 2006. Aerogels, in *Ullmann's encyclopedia of industrial chemistry.* Wiley-VCH, Weinheim, Germany.

Hwang, S.-W., Jung, H.-H., Hyun, S.-H., Ahn, Y.-S., 2007. Effective preparation of crack-free silica aerogels via ambient drying. *J. Sol-Gel Sci. Techn.* **41**: 139–146.

Jensen, K. I., Schultz, J. M., Kristiansen, F. H., 2004. Development of windows based on highly insulating aerogel glazings. *J. Non-Cryst. Solids* **350**: 351–357.

Job, N., Pirard, R., Marien, J., Pirard, J.-P., 2004. Porous carbon xerogels with texture tailored by pH control using sol-gel process. *Carbon* **44**: 619–628.

Job, N., Thery, A., Pirard, R., Marien, J., Kocon, L., Rouzard, J.-N., Beguin, F., Pirard, J.-P., 2005. Carbon aerogels, cryogels and xerogels: influence of the drying method on the textural properties of porous carbon materials. *Carbon* **43**: 2481–2494.

Job, N., Pirard, R., Pirard, J.-P., Alié, C., 2006a. Non intrusive mercury porosimetry: pyrolysis of resorcinol-formaldehyde xerogels. *Part. Part. Syst. Charact.* **23**: 72–81.

Job, N., Sabatier, F., Pirard, J.-P., Crine, M., Léonard, A., 2006b. Towards the production of carbon xerogel monoliths by optimizing convective drying conditions. *Carbon* **44**: 2534–2542.

Job, N., Panariello, F., Marien, J., Crine, M., Pirard, J.-P., Léonard, A., 2006c. Synthesis optimization of organic xerogels produced from convective air-drying of resorcinol-formaldehyde gels. *J. Non-Cryst. Solids* **352**: 24–34.

Jomaa, W., Puiggali, J.-R., 1991. Drying of shrinking materials: modellings with shrinkage velocity. *Drying Technol.* **9**: 1271–1293.

Jones, S. M., 2006. Aerogel: space exploration applications. *J. Sol-Gel Sci. Techn.* **40**: 351–357.

Kanamori, K., Aizawa, M., Nakanishi, K., Hanada, T., 2008. Elastic organic-inorganic hybrid aerogels and xerogels. *J. Sol-Gel Sci. Techn.* **48**: 172–181.

Kharzheev, Yu. N., 2008. Use of silica aerogels in Cherenkov counters. *Phys. Part. Nuclei.* **39**: 107–135.

Kharaghani, A., Metzger, T., Tsotsas, E., 2011. Discrete modeling approach to mechanical effects during isothermal drying. *AIChE J.* **51**: 872–885.

Kirkbir, F., Murata, H., Meyers, D., Chaudhuri, S. R., 1998a. Drying of aerogels in different solvents between atmospheric and supercritical pressures. *J. Non-Cryst. Solids* **225**: 14–18.

Kirkbir, F., Murata, H., Meyers, D., Chaudhuri, S. R., 1998b. Drying of large monolithic aerogels between atmospheric and supercritical pressures. *J. Sol-Gel Sci. Techn.* **13**: 311–316.

Kirsch, C., Metzger, T., Tsotsas, E., 2009. Towards a micro-scale simulation of convective gel drying. *Proceedings of XII Polish Drying Symposium,* Lodz, Poland, 223–234.

Kistler, S. S., 1931. Coherent expanded aerogels and jellies. *Nature* **127**: 741.

Kocklenberg, R., Mathieu, B., Blacher, S., Pirard, R., Pirard, J.-P., Sobry, R., Van den Bossche, G., 1998. Texture control of freeze-dried resorcinol-formaldehyde gels. *J. Non-Cryst. Solids* **225**: 8–13.

Kraiwattanawong, K., Mukai, S. R., Tamon, H., Lothongkum, A. W., 2007. Preparation of carbon cryogels from wattle tannin and furfural. *Microporous and Mesoporous Materials* **98**: 258–266.

Lecloux, A. J., 1981. Texture of catalysts, in *Catalysis: Science and technology*. Vol. **2** (eds J. R. Anderson, M. Boudart). Springer, Berlin, Germany, pp. 171–230.

Léonard, A., Job, N., Blacher, S., Pirard, J.-P., Crine, M., Jomaa, W., 2005a. Suitability of convective air drying for the production of resorcinol-formaldehyde and carbon xerogels. *Carbon* **43**: 1808–1811.

Léonard, A., Job, N., Jomaa, W., Pirard, J.-P., Crine, M., Puigalli, J.-R., 2005b. Textural comparison of resorcinol-formaldehyde xerogels obtained from vacuum drying and convective drying. *Proceedings of 7th World Congress of Chemical Engineering (WCCE7)*, Glasgow, Scotland, P4-009.

Léonard, A., Crine, M., Jomaa, W., 2006. Modelling of the convective drying of resorcinol-formaldehyde resins: influence of the drying conditions on the induced stress tensor. *Proceedings of 15th International Drying Symposium (IDS2006)*, Budapest, Vol. A, 273–278.

Léonard, A., Crine, M., Jomaa, W., 2007. Production of cylindrical carbon xerogel monoliths: effect of sample diameter on drying-induced cracks. *Extended Abstracts of 6th European Congress of Chemical Engineering (ECCE6)*, Copenhagen, Denmark, II (T2-7b).

Léonard, A., Blacher, S., Crine, M., Jomaa, W., 2008. Evolution of mechanical properties and final textural properties of resorcinol-formaldehyde xerogels during ambient air drying. *J. Non-Cryst. Solids* **354**: 831–838.

Leventis, N., Palczer, A., McCorkle, L., Zhang, G., Sotiriou-Leventis, C., 2005. Nanoengineered silica-polymer composite aerogels with no need for supercritical fluid drying. *J. Sol-Gel Sci. Techn.* **35**: 99–105.

Lin, C., Ritter, J. A., 1997. Effect of synthesis pH on the structure of carbon xerogels. *Carbon* **35**: 1271–1278.

Lippens, B. C., de Boer, J. H., 1965. Studies on pore systems in catalysis, Part 4: The t-method. *J. Catal.* **4**: 319–323.

Lu, X., Wang, P., Arduini-Schuster, M.-C., Kuhn, J., Büttner, D., Nilsson, O., Heinemann, U., Fricke, J., 1992. Thermal transport in organic and opacified silica monolithic aerogels. Proceedings of 3rd International Symposium on Aerogels, *J. Non-Cryst. Solids* **145**: 207–210.

Lubda, D., Lindner, W., Quaglia, M., du Fresne von Hohenesche, C., Unger, K. K., 2005. Comprehensive pore structure characterization of silica monoliths with controlled mesopore size and macropore size by nitrogen sorption, mercury porosimetry, transmission electron microscopy and inverse size exclusion chromatography. *J. Chromatography A* **1083**: 14–22.

Masmoudi, Y., 2006. *Etude du séchage au CO_2 supercritique pour l'élaboration de matériaux nanostructurés: application aux aerogels de silice monolithiques*. Diss, Ecole des Mines de Paris, France.

Masmoudi, Y., Rigacci, A., Ilbizian, P., Cauneau, F., Achard, P., 2006. Diffusion during the supercritical drying of silica gels. *Drying Technol.* **24**: 1121–1125.

Mathieu, B., Blacher, S., Pirard, R., Pirard, J.-P., Sahouli, B., Brouers, F., 1997. Freeze-dried resorcinol-formaldehyde gels. *J. Non-Cryst. Solids* **212**: 250–261.

Mayor, L., Sereno, A. M., 2004. Modelling shrinkage during convective drying of food materials: a review. *J. Food Eng.* **61**: 373–386.

Mukai, S. R., Nishihara, H., Tamon, H., 2008. Morphology maps of ice-templated silica gels derived from silica hydrogels and hydrosols. *Micropor. Mesopor. Mater.* **116**: 166–170.

Nishihara, H., Mukai, S. R., Yamashita, D., Tamon, H., 2005. Ordered macroporous silica by ice templating. *Chem. Mater.* **17**: 683–689.

Nunez, O., Nakanishi, K., Tanaka, N., 2008. Preparation of monolithic silica

columns for high-performance liquid chromatography. *J. Chromatogr. A* **1191**: 231–252.
Orlovic, A., Petrovic, S., Skala, D., 2005. Mathematical modeling and simulation of gel drying with supercritical carbon dioxide. *J. Serb. Chem. Soc.* **70**: 125–136.
Pajonk, G. M., Repellin-Lacroix, M., Abouarnadasse, S., Chaouki, J., 1990. From sol-gel to aerogels and cryogels. *J. Non-Cryst. Solids* **121**: 66–67.
Pakowski, Z., Glebowski, M., Adamski, R., 2006. Modeling of drying of highly shrinking materials using hydrogels as an example. *Drying Technol.* **24**: 1075–1081.
Pekala, R. W., 1989. Organic aerogels from the polycondensation of resorcinol with formaldehyde. *J. Mater. Sci.* **24**: 3221–3227.
Phalippou, J., Woignier, T., Prassas, M., 1990. Glasses from aerogels, Part I: The synthesis of monolithic silica aerogels. *J. Mater. Sci.* **25**: 3111–3117.
Pirard, R., Blacher, S., Brouers, F., Pirard, J.-P., 1995. Interpretation of mercury porosimetry applied to aerogels. *J. Mater. Res.* **10**: 2114–2119.
Pirard, R., Heinrichs, B., van Cantfort, O., Pirard, J.-P., 1998. Mercury porosimetry applied to low density xerogels: relation between structure and mechanical properties. *J. Sol-Gel Sci. Techn.* **13**: 335–339.
Pirard, R., Alié, C., Pirard, J.-P., 2005. Specific behavior of sol-gel materials in mercury porosimetry: collapse and intrusion, in *Handbook of sol-gel science and technology, Vol. 2: Characterization of sol-gel materials and products* (eds S. Sakka, R. M. Almeida). Kluwer Academic Publishers, Dordrecht, The Netherlands, pp. 211–233.
Pourcel, F., Jomaa, W., Puiggali, J.-R., Rouleau, L., 2007a. Criterion for crack initiation during drying: alumina porous ceramic strength improvement. *Powder Technol.* **172**: 120–127.
Pourcel, F., Jomaa, W., Puiggali, J.-R., Rouleau, L., 2007b. Crack appearance during drying of an alumina gel: thermo-hydro-mechanical properties. *Drying Technol.* **25**: 759–766.
Rao, A. P., Rao, A. V., Pajonk, G. M., 2007. Hydrophobic and physical properties of the ambient pressure dried silica aerogels with sodium silicate precursor using various surface modification agents. *Appl. Surf. Sci.* **253**: 6032–6040.
Reichenauer, G., Scherer, G. W., 2000. Nitrogen adsorption in compliant materials. *J. Non-Cryst. Solids* **277**: 162–172.
Reichenauer, G., Scherer, G. W., 2001a. Effects upon nitrogen sorption analysis in aerogels. *J. Colloid Interface Sci.* **236**: 385–386.
Reichenauer, G., Scherer, G. W., 2001b. Extracting the pore size distribution of compliant materials from nitrogen adsorption. *Colloid. Surf. A* **187–188**: 41–50.
Reichenauer, G., Pfrang, T., Hofmann, M., 2007. Drying of meso- and macroporous gels—length change and drying dynamics. *Colloid. Surf. A* **300**: 211–215.
Reimer, L., Kohl, H., 2008. *Transmission electron microscopy*. 5th edn, Springer, New York, USA.
Roe, R. J., 2000. *Methods of x-ray and neutron scattering in polymer science*. Oxford University Press, Oxford, UK.
Roig, A., Mata, I., Molins, E., Miravitlles, C., Torras, J., Llibre, J., 1998. Silica aerogels by supercritical extraction. *J. Eur. Ceram. Soc.* **18**: 1141–1143.
Rottereau, M., Gimel, J.-C., Nicolai, T., Durand, D., 2004. Monte Carlo simulation of particle aggregation and gelation, Part 1: Growth, structure and sized distribution of the clusters. *Eur. Phys. J. E* **15**: 133–140.
Sakka, S. (ed.) 2005. *Handbook of sol-gel science and technology, Vol. 3: Applications of sol-gel technology*. Kluwer Academic Publishers, Dordrecht, The Netherlands.
Sakka, S., Kozuka, H. (eds) 2005. *Handbook of sol-gel science and technology, Vol. 1: Sol-gel processing*. Kluwer Academic Publishers, Dordrecht, The Netherlands.
Schaefer, D. W., Martin, J. E., Wiltzius, P., Cannell, D. S., 1984. Fractal geometry of colloidal aggregates. *Phys. Rev. Lett.* **52**: 2371–2374.
Scherer, G. W., 1986. Drying gels, Part I: General theory. *J. Non-Cryst. Solids* **87**: 199–225.
Scherer, G. W., 1987a. Correction of "Drying gels, Part I: General theory". *J. Non-Cryst. Solids* **92**: 375–382.

Scherer, G. W., 1987b. Drying gels, Part 2: Film and flat plate. *J. Non-Crystalline Solids* **89**: 217–238.
Scherer, G. W., 1987c. Drying gels, Part 3: Warping plate. *J. Non-Cryst. Solids* **91**: 83–100.
Scherer, G. W., 1987d. Drying gels, Part 4: Rigid Gels. *J. Non-Cryst. Solids* **92**: 122–144.
Scherer, G. W., 1988. Drying gels, Part 5: . Viscoelastic plate. *J. Non-Cryst. Solids* **99**: 324–358.
Scherer, G. W., 1989. Drying gels, Part 8: Revision and review. *J. Non-Cryst. Solids* **109**: 171–182.
Scherer, G. W., 1990a. Stress and fracture during drying of gels. *J. Non-Cryst. Solids* **121**: 104–109.
Scherer, G. W., 1990b. Theory of drying. *J. Am. Ceram. Soc.* **73**: 3–14.
Scherer, G. W., 1992a. Recent progress in drying of gels. *J. Non-Cryst. Solids* **147–148**: 363–374.
Scherer, G. W., 1992b. Bending of gel beams: method of characterizing mechanical properties and permeability. *J. Non-Cryst. Solids* **142**: 18–35.
Scherer, G. W., 1992c. Stress development during supercritical drying. *J. Non-Cryst. Solids* **145**: 33–44.
Scherer, G. W., 1993. Freezing gels. *J. Non-Cryst. Solids* **155**: 1–25.
Scherer, G. W., 1994. Stress in aerogel during depressurization of autoclave, Part 1: Theory. *J. Sol-Gel Sci. Techn.* **3**: 127–139.
Scherer, G. W., Smith, D. M., Stein, D., 1995a. Deformation of aerogels during characterization. *J. Non-Cryst. Solids* **186**: 309–315.
Scherer, G. W., Smith, D. M., Qiu, X., Anderson, J. M., 1995b. Compression of aerogels. *J. Non-Cryst. Solids* **186**: 316–320.
Scherer, G. W., Haereid, S., Nilsen, E., Einarsrud, M.-A., 1996. Shrinkage of silica gels aged in TEOS. *J. Non-Cryst. Solids* **202**: 42–52.
Scherer, G. W., 1999. Structure and properties of gels. *Cement Concrete Res.* **29**: 1149–1157.
Scheuerpflug, P., Caps, R., Büttner, D., Fricke, J., 1985. Apparent thermal conductivity of evacuated SiO2-aerogel tiles under variation of radiative boundary conditions. *Int. J. Heat Mass Transfer* **28**: 2299–2306.
Schmidt, M., Schwertfeger, R., 1998. Applications of silica aerogel products. *J. Non-Cryst. Solids* **225**: 364–368.
Schneider, G. M., 1978. Physicochemical principles of extraction with supercritical gases. *Angew. Chem. Int. Ed. Engl.* **17**: 716–727.
Schwertfeger, R., Frank, D., Schmidt, M., 1998. Hydrophobic waterglass based aerogels without solvent exchange or supercritical drying. *J. Non-Cryst. Solids* **225**: 24–29.
Shaw, T. M., 1987. Drying as an immiscible displacement process with fluid counterflow. *Phys. Rev. Lett.* **59**: 1671–1675.
Shewale, P. M., Rao, A. V., Rao, A. P., 2008. Effect of different trimethyl silylating agents on the hydrophobic and physical properties of silica aerogels. *Appl. Surf. Sci.* **254**: 6902–6907.
Simpkins, P. G., Johnson, D. W., Fleming, D. A., 1989. Drying behavior of colloidal silica gels. *J. Am. Ceram. Soc.* **72**: 1816–1821.
Sinko, K., Torma, V., Kovacs, A., 2008. SAXS investigation of porous nanostructures. *J. Non-Cryst. Solids* **354**: 5466–5474.
Smith, D. M., Scherer, G. W., Anderson, J. M., 1995a. Shrinkage during drying of silica gel. *J. Non-Cryst. Solids* **188**: 191–206.
Smith, D. M., Stein, D., Anderson, J. M., Ackerman, W., 1995b. Preparation of low-density xerogels at ambient pressure. *J. Non-Cryst. Solids* **186**: 104–112.
Stepanek, F., Marek, M., Adler, P. M., 1999. Modeling capillary condensation hysteresis cycles in reconstructed porous media. *AIChE J.* **45**: 1901–1912.
Strøm, R. A., Masmoudi, Y., Rigacci, A., Petermann, G., Gullberg, L., Chevalier, B., Einarsrud, M.-A., 2007. Strengthening and aging of wet silica gels for up-scaling of aerogel preparation. *J. Sol-Gel Sci. Techn.* **41**: 291–298.
Tamon, H., Ishizaka, H., 1998. SAXS study on gelation process in preparation of resorcinol-formaldehyde aerogel. *J. Colloid Interface Sci.* **206**: 577–582.
Tamon, H., Ishizaka, H., Araki, T., Okazaki, M., 1998. Control of mesoporous structure of organic and carbon aerogels. *Carbon* **36**: 1257–1262.

Tamon, H., Ishizaka, H., 1999. Preparation of organic mesoporous gel by supercritical/freeze-drying. *Drying Technol.* **17**: 1653–1665.

Tamon, H., Ishizaka, H., Yamamoto, T., Suzuki, T., 1999. Preparation of mesoporous carbon by freeze-drying. *Carbon* **37**: 2049–2055.

Tamon, H., Ishizaka, H., Yamamoto, T., Suzuki, T., 2000. Influence of freeze-drying conditions on the mesoporosity of organic gels as carbon precursors. *Carbon* **38**: 1099–1105.

Tamon, H., Mukai, S. R., Nishihara, H., Yoshida, T., Yamamoto, T., Tonanon, N., Tanthapanichakoon, W., 2003. Microwave drying for synthesis of mesoporous carbon gels. *Proceedings of 3rd Asia-Pacific Drying Conference (ADC2003)*, Bankok, Thailand, 123–132.

Tamon, H., Kawahara, M., Kraiwattanawong, K., Nishihara, H., Mukai, S. R., 2006a. Preparation of carbon cryogel by sol-gel polycondensation of wattle tannin with formaldehyde. *Proceedings of 15th International Drying Symposium (IDS2006)*, Budapest, Hungary, Vol. C, 1859–1866.

Tamon, H., Nishihara, H., Mukai, S. R., 2006b. Synthesis of titania-silica microhoneycomb by unidirectional freezing and freeze-drying of hydrogel. *Proceedings of 15th International Drying Symposium (IDS2006)*, Budapest, Hungary, Vol. C, 1817–1824.

Tewari, P. H., Hunt, A. J., Lofftus, K. D., 1985. Ambient-temperature supercritical drying of transparent silica aerogels. *Mater. Lett.* **3**: 363–367.

Tillotson, T. M., Hrubesh, L. W., 1992. Transparent ultralow-density silica aerogels prepared by a two-step sol-gel process. *J. Non-Cryst. Solids* **145**: 44–50.

Tonanon, N., Siyasukh, A., Tanthapanichakoon, W., Nishihara, H., Mukai, S. R., Tamon, H., 2005. Improvement of mesoporosity of carbon cryogels by ultrasonic irradiation. *Carbon* **43**: 525–531.

Tonanon, N., Wareenin, Y., Siyasukh, A., Tanthapanichakoon, W., Nishihara, H., Mukai, S. R., Tamon, H., 2006. Preparation of resorcinol formaldehyde (RF) carbon gels: use of ultrasonic irradiation followed by microwave drying. *J. Non-Cryst. Solids* **352**: 5683–5686.

van Bommel, M. J., de Haan, A. B., 1994. Drying of silica gels with supercritical carbon dioxide. *J. Mater. Sci.* **29**: 943–948.

Vollet, D. R., Scalari, J. P., Donatti, D. A., Ruiz, A. I., 2008. A thermoporometry and small-angle x-ray scattering study of wet silica sonogels as the pore volume fraction is varied. *J. Phys. Condens. Matter* **20**: 025225.

Vorhauer, N., Metzger, T., Tsotsas, E., 2009. Empirical macroscopic model for drying of porous media based on pore networks and scaling theory. *Drying Technol.* **28**: 991–1000.

Wang, P., Körner, W., Emmerling, A., Beck, A., Kuhn, J., Fricke, J., 1992. Optical investigations of silica aerogels. *J. Non-Cryst. Solids* **145**: 141–145.

Wiener, M., Reichenauer, G., Scherb, T., Fricke, J., 2004. Accelerating the synthesis of carbon aerogel precursors. *J. Non-Cryst. Solids* **350**: 126–130.

Woignier, T., Scherer, G. W., Alaoui, A., 1994. Stress in aerogel during depressurization of autoclave, Part 2: Silica gels. *J. Sol-Gel Sci. Techn.* **3**: 141–150.

Woignier, T., Phalippou, J., Despetis, F., Etienne, P., Alaoui, A., Duffours, L., 2005. Mechanical properties of gels: from alcogel and aerogels to glasses. Ch. 2, in *Handbook of sol-gel science and technology, Vol. 2: Characterization and properties of sol-gel materials and products* (eds S. Sakka, R. M. Almeida). Kluwer Academic Publishers, Dordrecht, The Netherlands.

Wu, D., Fu, R., 2008. Requirements of organic gels for a successful ambient pressure drying preparation of carbon aerogels. *J. Porous Mater.* **15**: 29–34.

Yamamoto, T., Nishimura, T., Suzuki, T., Tamon, H., 2001a. Control of mesoporosity of carbon gels prepared by sol-gel polycondensation and freeze-drying. *J Non-Cryst. Solids* **288**: 46–55.

Yamamoto, T., Nishimura, T., Suzuki, T., Tamon, H., 2001b. Effect of drying method on mesoporosity of resorcinol-formaldehyde drygel and carbon gel. *Drying Technol.* **19**: 1319–1333.

Yamamoto, T., Endo, A., Ohmori, T., Nakaiwa, M., Mukai, S. R., Tamon, H., 2005. Effect of drying method on gas adsorption characteristics of carbon gel microspheres. *Drying Technol.* **23**: 2119–2129.

Zubizarreta, L., Arenillas, A., Menendez, J. A., Pis, J. J., Pirard, J.-P., Job, N., 2008. Microwave drying as an effective method to obtain porous carbon xerogels. *J. Non-Cryst. Solids* **354**: 4024–4026.